

Spring 1992

A transmission electron microscopy study of defect generation and microstructure development in ultrasonic wire bonding

Nikhil Mohan Murdeshwar
University of New Hampshire, Durham

Follow this and additional works at: <https://scholars.unh.edu/dissertation>

Recommended Citation

Murdeshwar, Nikhil Mohan, "A transmission electron microscopy study of defect generation and microstructure development in ultrasonic wire bonding" (1992). *Doctoral Dissertations*. 1684.
<https://scholars.unh.edu/dissertation/1684>

This Dissertation is brought to you for free and open access by the Student Scholarship at University of New Hampshire Scholars' Repository. It has been accepted for inclusion in Doctoral Dissertations by an authorized administrator of University of New Hampshire Scholars' Repository. For more information, please contact nicole.hentz@unh.edu.

INFORMATION TO USERS

This manuscript has been reproduced from the microfilm master. UMI films the text directly from the original or copy submitted. Thus, some thesis and dissertation copies are in typewriter face, while others may be from any type of computer printer.

The quality of this reproduction is dependent upon the quality of the copy submitted. Broken or indistinct print, colored or poor quality illustrations and photographs, print bleedthrough, substandard margins, and improper alignment can adversely affect reproduction.

In the unlikely event that the author did not send UMI a complete manuscript and there are missing pages, these will be noted. Also, if unauthorized copyright material had to be removed, a note will indicate the deletion.

Oversize materials (e.g., maps, drawings, charts) are reproduced by sectioning the original, beginning at the upper left-hand corner and continuing from left to right in equal sections with small overlaps. Each original is also photographed in one exposure and is included in reduced form at the back of the book.

Photographs included in the original manuscript have been reproduced xerographically in this copy. Higher quality 6" x 9" black and white photographic prints are available for any photographs or illustrations appearing in this copy for an additional charge. Contact UMI directly to order.

U·M·I

University Microfilms International
A Bell & Howell Information Company
300 North Zeeb Road, Ann Arbor, MI 48106-1346 USA
313/761-4700 800/521-0600

Order Number 9225259

**A transmission electron microscopy study of defect generation
and microstructure development in ultrasonic wire bonding**

Murdeshwar, Nikhil Mohan, Ph.D.

University of New Hampshire, 1992

Copyright ©1992 by Murdeshwar, Nikhil Mohan. All rights reserved.

U·M·I
300 N. Zeeb Rd.
Ann Arbor, MI 48106

A TRANSMISSION ELECTRON MICROSCOPY STUDY OF
DEFECT GENERATION AND MICROSTRUCTURE
DEVELOPMENT IN ULTRASONIC WIRE BONDING

BY

NIKHIL MURDESHWAR

B.Eng., University of Mysore, India, 1983.

M.S., University of Massachusetts, Amherst, 1989.

DISSERTATION

Submitted to the University of New Hampshire

in Partial Fulfillment of

the Requirements for the Degree of

Doctor of Philosophy

in

Engineering

May, 1992.

This dissertation has been examined and approved.



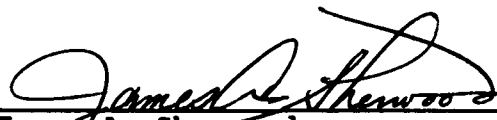
Dissertation Director, James E. Krzanowski
Associate Professor of Mechanical Engineering



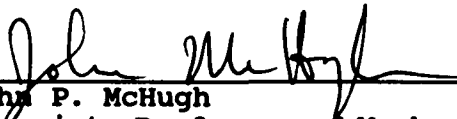
Todd S. Gross
Associate Professor of Mechanical Engineering



Barbaros Celikkol
Associate Professor of Mechanical Engineering



James A. Sherwood
Assistant Professor of Mechanical Engineering



John P. McHugh
Associate Professor of Mechanical Engineering

May 4, 1992
Date

ACKNOWLEDGEMENTS

My days at the University of New Hampshire will perhaps be remembered as the most critical three years of my life, for it was here I grew from being an engineering student to an ambitious material scientist. For this I am greatly indebted to various people: Prof. Krzanowski instilled in me the confidence to do a Ph.D. thereby preparing me for life's major challenges; Prof. Gross influenced me the most on life's 'big issues' among other things during our morning cups of coffee; Julie Clark kept me focussed on the priorities. To both Profs. Krzanowski and Gross I wish to thank for their advice on this work and patience in answering my numerous questions even the dumb ones, and to Julie I would like to express my gratitude for the sacrifices she made during the four years she's known me.

In addition to the aforementioned individuals, I acknowledge Prof. Sherwood's assistance on matters pertaining to and outside of work, and Profs. Celikkol and McHugh for their suggestions as members of my thesis committee. Nancy Cherim's friendship and assistance in microscopy and Dr. A.Garrett-Reed's help in scheduling a part of this research on the HB5 at MIT are also gratefully acknowledged.

My appreciation is also extended to the helpful staff at the Mechanical Engineering Department; Gary, Eileen, Dan and

Ron, at the instructional services; all my buddies especially Xishun Zhang; and my parents who have supported all of my adventurous endeavors.

Finally, the grant by IBM Corporation towards this research is gratefully acknowledged.

**Dedicated with the deepest love and appreciation
to my grandparents
Gajananan and Rajani Khot.**

TABLE OF CONTENTS

ACKNOWLEDGMENTS..... iii
DEDICATION..... iv
LIST OF TABLES..... viii
LIST OF FIGURES..... ix
ABSTRACT..... xvii

<u>CHAPTER</u>	<u>PAGE</u>
I. INTRODUCTION	1
II. LITERATURE SURVEY	4
2.1. The Effect of Ultrasound on Metal Properties.....	4
2.2. Bonding Mechanism.....	11
2.3. Fatigue Microstructures.....	15
2.3.1. Non-Ultrasonic Fatigue.....	16
2.3.2. Ultrasonic Fatigue.....	34
2.4. Interfacial Reactions and Reliability.....	45
2.5. Summary and Research Outline	51
III. EXPERIMENTAL METHODS	53
3.1. Materials.....	53
3.2. Mechanical Testing.....	54
3.3. Transmission Electron Microscopy	

Specimen Preparation Techniques.....	54
IV. MICROSTRUCTURE TRANSFORMATIONS DURING UWB.....	63
4.1. Wire Transformations.....	66
4.2. Substrate Microstructure Transformations...	75
4.2.1. Transformations in Aluminum.....	77
4.2.2. Transformations in Nickel.....	83
4.2.3. Transformations in Copper.....	93
4.2.4. Transformations in Stainless Steel..	102
V. THE EXTENT OF MICROSTRUCTURAL TRANSFORMATIONS	
DURING BONDING.....	107
5.1. σ_{ys} and its Influence on the UWB Process...	108
5.2. Ambient Temperature and its Influence on	
the UWB Process.....	119
5.3. A Model for Substrate Microstructural	
Transformation.....	122
VI. MICROSTRUCTURAL TRANSFORMATIONS AFTER BONDING....	130
6.1. Thermally Induced Transformations in Nickel	131
6.1.1. Transformations in Bulk Nickel.....	131
6.1.2. Transformations in Nickel Boron	
Substrates.....	134
6.2. Transformations in Thin Gold Substrates....	138
6.3. Transformations in Thick Gold Substrates...	147

6.4. Bond Strength Measurements..... 155

VII. THE EFFECT OF SURFACE CONDITION ON UWB..... 158

 7.1. Aluminum Substrates..... 159

 7.2. Stainless Steel Substrates..... 161

VIII. DISCUSSION..... 165

 8.1. Proposed Mechanisms of Bonding and
 Microstructural Development..... 165

 8.2. Thermal Transformations and Reliability.... 172

IX. CONCLUSIONS..... 177

X. SUGGESTIONS FOR FUTURE WORK..... 180

REFERENCES 182

LIST OF TABLES

<u>TABLE</u>		<u>PAGE</u>
1	Bonding substrate properties.	65
2	Total dislocation strain energies.	86
3	Literature data for cell formation during non-ultrasonic cyclic testing.	103
4	Experimental and theoretical σ_{ys} .	111
5	ω -model parameter for different metal substrates.	125
6	ω -model parameter for Cu alloy substrates.	126
7	ω as a result of change in the ambient temperature,	128
8	Analysis of Al/Ni-B interface (as-bonded specimen).	134
9	Microanalysis of points labelled in Fig. 81.	139
10	Microanalysis of points labelled in Fig. 84.	140
11	Microanalysis of points labelled in Fig. 86.	141
12	Microanalysis of points labelled in Fig. 88.	148
13	Microanalysis of points labelled in Fig. 90.	149
14	Bondability test results.	156
15	Summary of observed substrate transformations.	166

LIST OF FIGURES

<u>FIGS.</u>		<u>PAGES</u>
1	The influence of ultrasound on static of a zinc single crystal. (-) without ultrasound; (---) with ultrasound. (From Severdenko, Klubovich, Stepanenko, 1972).	9
2	Stress versus elongation for aluminum single crystals; (-) without ultrasound; (---) with ultrasound. (From Langenecker, 1966).	9
3	Acoustic hardening in zinc crystals (glide rate = $6 \times 10^{-5} \text{ s}^{-1}$). (From Langenecker, 1966).	10
4	Schematic illustration of the Aluminum ultrasonic wedge wire bonding process. (From Krzanowski, Murdeshwar, 1990).	16
5	Dislocation configurations in 310 stainless steel at $\epsilon_p = 5.0 \times 10^{-4}$. (a) dislocation pileups; (b) individual dislocations; (c) bundles of long dislocations. (From Jin, Zhon, Chen, 1990).	23
6	Dislocation configurations in 310 stainless steel at $\epsilon_p = 2.4 \times 10^{-3}$. (a) Loose arrangement (left) and ^p dislocation tangles (right); (b) dislocation veins; (c) embryos of PSB ladder structure; (d) well developed walls. (From Jin, Zhon, Chen, 1990).	24
7	Dislocation configurations in 310 stainless steel at $\epsilon_p = 8.8 \times 10^{-3}$. (a) Labyrinth structure; ^p (b) PSB ladder structure; (c) Two sets of inclined dislocation walls (d) Dislocation cells. (From Jin, Zhon, Chen, 1990).	25
8	The cyclic stress-strain and monotonic tensile test curves for a commercial low alloyed steel. (From Roven, Nes, 1991).	26
9a	Low cycle fatigue substructure of copper at $\epsilon_p = 0.0017; 0.0124$; (From Saxena, Antolovich, 1975).	26
9b	Low cycle fatigue substructure of copper at $\epsilon_p = 0.030$. (From Saxena, Antolovich, 1975).	27

10	Low cycle fatigue substructure of Cu-2.2Al at $\epsilon_p = 0.0029; 0.022$. (From Saxena, Antolovich, 1975).	28
11	Low cycle fatigue substructure of Cu-4.2Al at $\epsilon_p = 0.0027; 0.0113$. (From Saxena, Antolovich, 1975).	29
12	Low cycle fatigue substructure of Cu-6.3Al at $\epsilon_p = 0.0025; 0.042$. (From Saxena, Antolovich, 1975).	30
13	Planar arrays of dislocation in 304 stainless steel cycled at $\epsilon_p = 0.020$ at 25°C. (From Abdel-Raouf, Plumtree, Topper, 1974).	31
14	Cell formation in 304 stainless steel cycled at $\epsilon_p = 0.020$ at 25°C. (From Abdel-Raouf, Plumtree, Topper, 1974).	32
15	Schematic representation of the dislocation stress present at saturation in low amplitude fatigue of copper. Well defined loop patches have been named 'veins' in this representation. (From Figueroa, Bhat, De La Veaux, Murzenski, Laird, 1981).	32
16	Various dislocation structures formed in different oriented crystals. (From Jin, Winter, 1984).	33
17	Cyclic stress-strain curve for copper at room temperature at 6×10^5 cycles. (From Weiss, 1970).	39
18	Polycrystalline copper subjected to ultrasonic fatigue at 6×10^5 cycles and a strain amplitude of $< 2 \times 10^{-4}$. (From Weiss, 1970).	39
19	Polycrystalline copper subjected to ultrasonic fatigue at 6×10^5 cycles and a strain amplitude of $\approx 2-3 \times 10^{-4}$. (From Weiss, 1970).	40
20	Polycrystalline copper subjected to ultrasonic fatigue at 6×10^5 cycles and a strain amplitude of $\approx 2-3 \times 10^{-4}$. (From Weiss, 1970).	40
21	Polycrystalline copper subjected to ultrasonic fatigue at 6×10^5 cycles and a strain amplitude of $= 4-5 \times 10^{-4}$. (From Weiss, 1970).	41

22	Polycrystalline copper subjected to ultrasonic fatigue at 6×10^5 cycles and a strain amplitude of 5.5×10^{-4} . (From Weiss, 1970).	41
23	Ultrasonically irradiated aluminum showing sub-boundaries consisting of dislocation networks. (From Westmacott, Langenecker, 1965).	42
24	Ultrasonically irradiated aluminum showing high dislocation loop density in vicinity of sub-boundary; loops are 100-1000 Å in diameter; plane of foil is (312). (From Westmacott, Langenecker, 1965).	43
25	Composite bright field micrograph showing extensive deformation damage and dislocation cell and sub-boundary formation near a high angle grain boundary (GB) in the core of specimen C. Grain boundary $M_{23}C_6$ (C), equiaxed cells (E), and cell refinement (R) are also seen. (From Shea, Rao, 1982).	44
26	Phase diagram of Au-Al (From Majni, Nobili, Ottaviani, Costato, 1981.)	49
27	Phase diagram Ni-Al (From Janssen, Rieck, 1967).	50
28	Competing processes during bonding (From Joshi, 1971).	57
29	Bond pull-test apparatus.	57
30	Cross-section view specimen preparation technique.	61
31	Plan-view specimen preparation technique.	62
32	Microstructure of bonded wires to pure Al substrate with a high bonding time of 90 msec.	72
33	Microstructure of bonded wires to pure Al substrate with typical bonding parameters of 85 gf, 60 msec, and 0.6 W.	72
34	Microstructure of bonded wires to an as-received Al 2024 alloy with bonding parameters of 100 gf, 60 msec, and 0.7 W.	73
35	The grain structure near the tail section of a bonded wire. The black spots are contaminants from the silver epoxy.	73

36	Dislocation loops in the wire bonded with a high bonding time of 90 msec.	74
37	Low angle grain boundaries in the bonded wire in a specimen bonded with a high bonding time of 90 msec - weak beam (left) and bright-field (right) images.	74
38	Microstructure of the substrate near a wire bond showing a dislocation loop forming behind a jog in a dislocation.	76
39	An etched wire bond showing three different regions of plan view specimens.	76
40	Microstructure of the 6061 substrate near a bonded wire. The bond interface is shown across the top.	80
41	Microstructure of the 6061 substrate away from the wire bond area.	80
42	The condition of the 6061 substrate prior to bonding.	81
43	Image of the bond interface in the pure Al substrate bonded with high bonding time. The bond interface is indicated by arrows.	81
44	Image of the bond interface in a contaminated region (Krzanowski, 1989).	82
45	Image of the bond interface with dislocations emitted from a contaminated region (indicated by arrows).	82
46	Distinct dislocation cells observed in the BZ of an annealed Ni substrate.	88
47	A transition from dislocation cells to veins in the BZ of an annealed Ni substrate.	88
48	Dislocation veins in the BZ of an annealed Ni substrate.	89
49	Magnified image of the dislocation veins in the BZ.	89
50	Intense dislocation inhomogenous deformation at the PZ for an annealed Ni substrate.	90
51a	Selected area diffraction pattern of the PZ compared to Al.	90
51b	Typical annealed grain structure of the OZ.	91
52	Cross section view Ni substrate showing dislocation cells.	91

53	Dislocation cells in the BZ of a cold worked Ni substrate.	92
54	Recovered subgrains in the BZ of an annealed Cu substrate.	96
55	Round equiaxed grains in the BZ of an annealed Cu substrate.	96
56	Intense dislocation inhomogeneous deformation at the PZ of an annealed Cu substrate.	97
57	Low-angle thick walled completely recovered cells in the BZ of a cold worked Cu substrate.	97
58	Low-angle thick walled completely recovered cells in the BZ of a cold worked Cu substrate.	98
59	Microstructure of the BZ in an annealed Cu substrate at a bond time of 20 msec.	100
60	Microstructure of the BZ in an annealed Cu substrate at a bond time of 95 msec.	100
61	Microstructure of the BZ in an annealed Ni substrate showing dislocation cells.	101
62	Microstructure of the BZ in an annealed Ni substrate showing dislocation pileups.	101
63	Microstructure of the BZ in an annealed stainless steel substrate.	106
64	Microstructure of the BZ in an annealed stainless steel substrate.	106
65	Microstructural transformation of the BZ in a small grain Cu specimen.	115
66	Microstructural transformation of the BZ in a small grain ambralloy specimen.	115
67	Planar dislocation structure in the BZ of a large grain brass specimen.	116
68	Wavy dislocation structure in the BZ of a large grain brass specimen.	116
69	Planar and wavy dislocation structure in the BZ of a small grain brass specimen.	117
70	Boundary between the PZ and OZ in a large grain brass specimen bonded using small parameters.	117

71	Boundary between the PZ and BZ in a large grain brass specimen bonded using small parameters.	118
72	BZ in a large grain brass specimen bonded using large parameters.	118
73	Microstructural transformation of the BZ in a Ni substrate bonded at an ambient temperature of 150°C.	120
74	Microstructural transformation of the BZ in a Ni substrate bonded at an ambient temperature of 150°C.	120
75	Microbands in a Ni substrate bonded at 350°C.	121
76	OZ of a Ni substrate bonded at 350°C.	121
77	SEM image of Al wire bonded to bulk Ni aged at 500°C for 24 h. Average intermetallic thickness in these specimens was 75 microns.	133
78	Al/Ni intermetallic thickness obeys the parabolic growth law.	133
79	STEM image of the Al/Ni-B interface. Al is on the upper right and the Ni-B is at the lower left.	137
80	STEM image and elemental maps for Al/Ni-B specimen aged for 8 h at 125°C. The map shows O, Ni, and Al.	137
81	Bright-field image of the thin-Au specimen in the as bonded condition. The Al wire (top) and the Ni-P substrate (bottom) are separated by an intermetallic layer (dark region).	143
82	Bright-field image of the thin-Au specimen in the as bonded condition.	144
83	Elemental map for the image shown in Fig. 81. The upper left corner shows the image followed by Al, Ni, and Au maps.	144
84	STEM bright-field image of the thin-Au specimen aged for 48 h at 125°C. Note the unreacted layer of immersion Au on the Ni-P coating near a void.	145
85	Elemental map for the image shown in Fig. 84. The image is shown along with Al, Ni, and Au maps.	145

86	STEM image of a thin-Au specimen after 1500 thermal cycles. Al is at the lower left while Ni-P is at the upper right.	146
87	Elemental map for the image shown in Fig. 86. The image is shown along with Al, Au, and Ni maps.	146
88	Dark-field STEM image and elemental maps for thick-Au after 1500 thermal cycles.	152
89	TEM bright-field image of the intermetallic formed in the thick-Au specimen after 1500 thermal cycles.	152
90	Dark-field STEM image and elemental maps for thick-Au specimens after 3000 thermal cycles. Numbers indicate locations for microchemical analysis.	153
91	Dark-field STEM image and elemental maps for a thick-Au specimen aged 8 h at 125°C. The dark areas are voids which may be Kirkendall porosity.	154
92	TEM image of the intermetallic in a thick-Au specimen subjected to 1500 thermal cycles. Note the presence of voids.	154
93	Bond pull strength for wire bonded specimens in the as-received condition, and after 1500 or 3000 thermal cycles.	157
94	Percent of bond lifts for wire bond specimen test results in Fig. 93.	157
95	Bond pull strength versus surface roughness for wires bonded to pure Al substrates.	163
96	Bond pull strength versus surface roughness for wires bonded to 304 stainless steel substrates.	163
97	Cross section view specimen of Al wire bonded to Ni-B plated substrate.	164

ABSTRACT

**A TRANSMISSION ELECTRON MICROSCOPY STUDY OF
DEFECT GENERATION AND MICROSTRUCTURE
DEVELOPMENT IN ULTRASONIC WIRE BONDING**

by

Nikhil Murdeshwar

University of New Hampshire, May 1992.

Ultrasonic wire bonding is widely used in the electronic industry to connect semiconductor chips to packages. Even though the popularity of the technique has increased in recent times, questions remain about the bonding mechanism, and factors affecting bondability and reliability. In this thesis, answers were provided to many of these questions using TEM to examine bonded cross section and plan view specimens.

A detailed investigation of the Al wire and substrate showed dynamically annealed well recovered grains while microstructural observations of other substrates revealed wide varieties of response mechanisms. For example, Ni formed a dislocation cell structure, Cu formed a partially recovered structure, while Cu alloys and stainless steel formed planar dislocation arrays. These observed transformations were correlated with basic material properties and literature reported cyclic deformation studies to determine factors

contributing to substrate plastic deformation during bonding. It appeared that the plastic deformation of the substrate is not a requirement for good bonding, but since extensive plastic deformation can occur during bonding, it could have important implications in bond strength and reliability.

A model developed to estimate microstructural transformations was effective when applied to different metal substrates but somewhat less effective with Cu alloys.

The extent and type of intermetallic phases that formed at the wire-substrate interface after thermal aging, thermal cycling and in the as-bonded conditions were characterized for different Au and NiB plated substrates using EDS. Specimens were also examined for the extent of Kirkendall porosity and the conditions of the unreacted portions of the wire and substrate. It was found that the extent of interfacial reactions depended strongly on substrate metallurgy. For example, in the NiP/immersion Au specimen the original Au layer was still present after bonding, and transformed completely to Al-Au intermetallics after only 1.5 h at 90°C. The same treatment resulted in no intermetallic phase formation for Ni-B specimens with the interface remaining chemically and structurally sharp.

Finally, mechanisms of bonding and microstructural development were proposed.

CHAPTER I

INTRODUCTION

Ultrasonic bonding was accidentally discovered (Rosenberg, 1973, as referenced in Winchell, 1978) in Germany almost half a century ago. It has since been widely used in the automotive, aerospace, electrical and electronic industries as a cost-effective alternative to soldering, resistance welding and mechanical fastening. Advantages offered by the technique in structural applications are (Devine, 1984) the simplicity of tooling, the energy efficiency of the process and the small amount of heat generated during bonding. Since the method often replaces mechanical fasteners, weight and costs are reduced. The yield strength of ultrasonic bonds are often higher than those of resistance welds and brittle intermetallics are not formed because the base metal does not melt. In addition, molten metal is not expelled from the joint as in resistance welding and fluxes and fillers are not required. The technique also has a few limitations, such as a restriction as to the types of welds possible (only lap joints), capital equipment costs are higher than resistance welders, bonding is restricted to

softer metals since harder metals require more energy and bonding usually cannot be done on complex designs.

Only in recent years has the use of ultrasonic bonding in the electronic industry increased where it is mostly used for interconnecting semiconductor chips to packages by means of thin wires. To form an electrical connection, a metallurgical reaction such as melting, solidification, diffusion, dissolution or plastic deformation is required. This metallurgical reaction is critical for continuity of the electrical circuit and can affect the reliability of the entire electronic component. Therefore by understanding the metallurgical reaction which occurs during UWB, improvements can be made to enhance component reliability.

This thesis describes an extensive investigation of many facets of the ultrasonic wire bonding (UWB) process. First, the microstructure of bonding Al wire itself was examined. Next, the substrate microstructure was examined after bonding to a number of different metals including Al. The observations from these studies were correlated with basic material properties and reported cyclic deformation studies, and a simple model was developed to estimate certain microstructural changes. The bond interface metallurgical reaction which occurred subsequent to bonding was also studied after aging and thermal cycling tests. In addition to microstructure studies, the effects of substrate roughness, hardness and contamination were also investigated. Finally, a bonding

mechanism was proposed in light of observations from this study.

The major difference in this study from earlier investigations is the use of transmission electron microscopy (TEM) techniques for microstructure examination. The TEM offers higher resolution than previously used microstructural techniques and is necessary to image defects such as dislocations and grain boundaries, or to measure chemical composition on a microscopic scale.

The results of this study show that despite extensive deformation during bonding the Al wire had a surprisingly well-recovered grain structure. The substrate surface also surprisingly underwent extensive deformation resulting in a microstructure transformation. Depending on the substrate material, the transformed microstructure showed recovery, cell formation, veins or planar dislocation arrangements. Examination of the metallurgical reactions show the nature of precipitation reaction at the interface. It was also shown that for good bonding an ideal substrate would be soft, clean and slightly rough.

Before presenting the results of this study, several related areas such as the effect of ultrasound on metal properties, previously proposed wire bonding mechanisms, reported non-ultrasonic and ultrasonic fatigue microstructures, and interfacial reaction in the Au-Al and Ni-Al systems, will be reviewed in a literature survey.

CHAPTER II

LITERATURE SURVEY

2.1 The Effect of Ultrasound on Metal Properties - It has long been known that ultrasound causes softening in metals leading to the phenomenon of "acoustic weakening". This phenomenon was first demonstrated by Blaha and Langenecker (1955) on a single crystal of zinc. Their results reproduced here in Fig. 1 established that the use of ultrasound at stresses above the yield strength during a tensile test caused a decrease in the static stress (Curve 1). Upon turning off the ultrasound, the static stress returned to the original value. The effect reappeared when the ultrasound was again turned on. If, as in Curve 2, ultrasound was applied from the beginning of the tensile test, then a more gently sloped curve was obtained. In subsequent work Langenecker (1963) showed that the strength of other metals such as aluminum, beryllium, tungsten, low-carbon steel and stainless steel was also reduced when subjected to intense ultrasound. He made an interesting comparison between the effects of thermal and ultrasonic energy on the stress-strain curve of aluminum single crystals. The results,

reproduced here in Fig. 2, show the similarity of the curves with ultrasound at constant temperature, and at different temperatures without ultrasound. From this work it was evident that either heat or ultrasound could independently cause an equivalent deformation. It was also shown that the applied energy density required to cause an equivalent deformation by ultrasound was approximately 10^7 less than that by thermal energy. The difference in energy densities was explained by the fact that damping of sound waves takes place (Roderick, Truell, 1952) in crystal lattice defects such as grain boundaries, dislocations, etc., whereas thermal energy is distributed uniformly throughout the metal volume. Blaha and Langenecker (1955) explained the effect of sound waves on the static yield strength of zinc crystals based on the activation of dislocations by sound energy absorption. A different explanation for acoustic weakening was put forth by Nevill and Brotzen (1957) who attributed it to a mechanism of superposition on the static stress of the alternating stresses developed during ultrasound vibrations.

Chernenko et al. (1960, as referenced in Severdenko, Klubovich, Stepanenko, 1972) investigated the influence of ultrasound on the strength and ductility of copper at various temperatures. Specimens were first ultrasonically treated at a frequency of 19.5 kHz over a temperature range of 20°C to 700°C for times from 1 to 20 minutes, after which they were tensile tested. With an increase in temperature starting with

400°C, sharp drops in tensile strength and elongation were observed. Similar results were obtained with an increase in time of ultrasonic treatment at the same temperature. However, with long ultrasonic treatment time of 15-20 minutes at high temperatures of 600-700°C, copper transformed from the plastic to brittle condition, microcracks developed at the grain boundaries and microhardness dropped. It was hypothesized that with an increase in temperature, ultrasonic vibrations had a major influence on the change in the grain boundary structure, causing brittle failure of the metal at room temperature. The change in grain boundary was explained by the formation and accumulation of vacancies in microscopic pores and microcracks.

Another phenomenon associated with ultrasound and metal properties is "acoustic hardening" which comes into effect after the application of sufficiently high stress amplitude ultrasound. Fig. 3 (Langenecker, 1966) illustrates this phenomenon for Zn crystals. At point "a", ultrasound of 5 W/cm² is applied and acoustic weakening is observed which upon turning off returns to the original curve at "a'". Now, when the applied ultrasound is 15 W/cm² at "b", acoustic weakening is observed which shows up as hardening at "b'" upon turning off the ultrasound. Similarly, "c" and "c'" show the effect of turning on and off ultrasound of 25 W/cm². This behavior demonstrated another distinction between ultrasonic and thermal energy. Application of intense ultrasound leads to

hardening while heat treatment causes softening.

Possible mechanisms by which acoustic energy could be transmitted to the dislocation structure are resonance, relaxation and hysteresis. All these were explained (Severdenko, Klubovich, Stepanenko, 1972) to be insignificant except at critical conditions of frequency and therefore do not fully account for the effects of acoustic weakening and hardening. Based on Langenecker's (1962, 1963, 1966) work, Severdenko et al. attempted to explain the above described phenomena of acoustic weakening and acoustic hardening using dislocation theory. Ultrasonic waves on passing through a crystal are said to activate dislocations by localized heating as a result of acoustic energy absorption by dislocations and other crystal defects. When a crystal is in the loaded condition, the effect of relatively low-intensity ultrasound on it is said to mobilize some of the activated dislocations. Mobile dislocations in this case are thought to cause additional plastic deformation thereby decreasing the static stress. With prolonged ultrasound the mobile dislocations interact which reduces their mean mobility. However, for most dislocations at low-intensity ultrasound there is only an increase in the oscillation amplitude around the equilibrium position in which case the stress-strain curve will not differ from that of a tensile curve under normal conditions. If the crystal is in the unloaded condition, low-intensity ultrasound is thought to increase dislocation oscillation amplitude and

nucleate new dislocations over time.

In both cases, it is hypothesized that a certain critical intensity of ultrasonic oscillation is required for plastic deformation. On cessation of ultrasonic action a work hardened structure typically expected of plastic deformation is said to be found. This structure is in the form of a dislocation density increase, with the formation of a large number of obstacles due to intersection of moving dislocations with immobile ones, the formation of blocked loops of vacancies, etc. Any further plastic deformation in this metal sample would involve significantly more force.

Acoustic weakening can therefore be described to be a result of an interaction of acoustic energy with the microstructure that aids dislocation mobility. Since dislocation movement signals the onset of yielding, there is a lowering of the material yield strength. On cessation of ultrasound, mobile dislocations freeze with no activation energy to overcome obstructions in their path. The resulting work hardened structure is said to give rise to acoustic hardening.

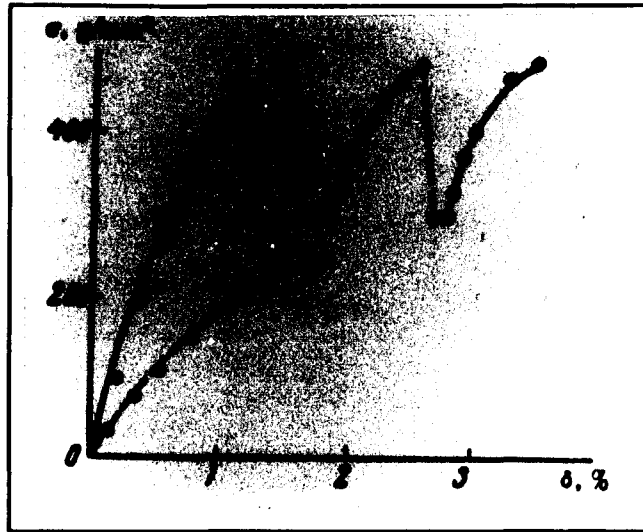


Figure 1 The influence of ultrasound on static tensile stress of a zinc single crystal. (-) without ultrasound; (---) with ultrasound. (From Severdenko, Klubovich, Stepanenko, 1972).

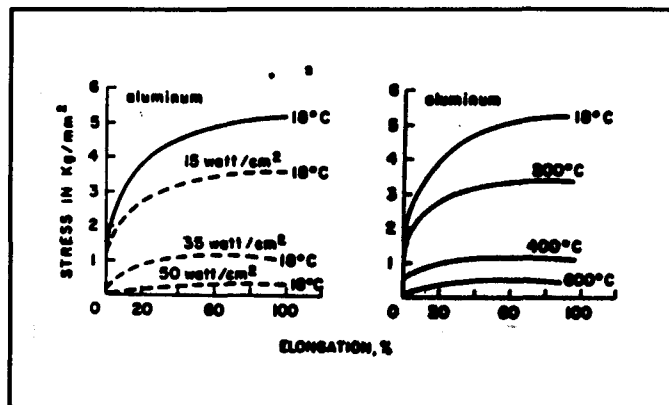


Figure 2 Stress versus elongation for aluminum single crystals; (-) without ultrasound; (---) with ultrasound. (From Langenecker, 1966).



Figure 3 Acoustic hardening in zinc crystals (glide rate = $6 \times 10^{-5} \text{ s}^{-1}$). (From Langenecker, 1966).

2.2 Bonding Mechanism - The ability of a metal to soften temporarily under the influence of ultrasound is used in the process of ultrasonic wire bonding schematically illustrated in Fig. 4. A wire of 25-100 μm diameter is drawn under a tool. On locating a suitable spot, the tool is lowered thereby clamping the wire to the substrate and applying a fixed force of about 100gf. The tool is simultaneously vibrated at ultrasonic frequencies for a short time period, usually less than 100 msec, during which the wire is flattened and a bond formed. The tool is then raised to find another suitable spot and the bonding process repeated. At this point the wire can either be cut or bonding continued to form stitch bonds and the wire cut at the termination of the process.

Over the years several explanations for the mechanism of wire bonding have been put forth that has led to much controversy further complicated by the short bonding time periods. The amount of heat generated during the process and its role in the bonding mechanism have comprised one such controversial issue. Kreye (1975) based on transmission electron microscopy (TEM) studies of cross-section view ultrasonic spot-welded Al to Cu specimens observed an ultrafine grain structure and concluded that melting had occurred at the interface and therefore heat was an integral part of the bonding mechanism. There have been other attempts to gauge the temperature increase as a result of bonding at the bond interface, with reported values ranging from 80°C

(Joshi, 1971) to 250°C (Krzanowski, Murdeshwar, 1990). The former was measured using a thermocouple and an oscilloscope at the bond interface while the latter was calculated from TEM observations using diffusion kinetics. Thermocouple measurements have been challenged as they measure an average temperature rather than a maximum, although adequate precautions (Joshi, 1971) were taken in that instance. However, by producing strong bonds in liquid nitrogen (-195°C), both Joshi (1971) and Harman et al. (Harman, Leedy, 1972) demonstrated the lack of need for high temperatures in the wire bonding process. In fact it has been pointed out (Harman, Albers, 1977) that heat is a by-product of the process rather than a requirement for it. Krzanowski et al.'s calculated temperature reiterates this claim and indirectly demonstrates Langenecker's analogy between the effect of temperature and ultrasound on a metal, as discussed in the previous section. To attain the higher temperatures hypothesized by some researchers (Plough, Davis, Lawler, 1969; Uthe, 1969) Joshi decreased the clamping force by 50% and could only achieve a maximum temperature of 120°C. The small increase in heat was attributed to interfacial sliding.

One theory proposed by Hulst and Lasance (1978) concentrated on interfacial sliding during bonding. It was proposed that 10-100 μm oblong welds were initially formed by means of a fretting mechanism. During fretting, oxides and other surface contaminants were said to be removed and further

growth of the weld took place by increasing the dimension and number of microwelds. For the fretting action to occur, it was thought that interfacial sliding was crucial. However, through laser interferometry and high speed recording techniques (Martin, Wilson, 1970, as referenced in Joshi, 1971) it was shown that interfacial sliding between the wire and the substrate did not take place. Harman et al. (Harman, Leedy, 1972) demonstrated this through a simple clamped-wire experiment consisting of clamping the wire by making two ultrasonic bonds approximately 5 millimeters apart (with no loops between bonds) and then making a bond at the center. It was found that although the center bond showed a little more deformation due to a lengthwise constraint of the other two bonds, it possessed the same strength.

Devine (1980) suggested that ultrasonic vibrations caused the breakup of oxides and surface films permitting bare metal contact. It was proposed that interatomic diffusion across the interface resulted in bonding without application of heat. Although several researchers (Harman, Leedy, 1972; Joshi, 1971; Winchell, Berg, 1978; Krzanowski, 1989; Krzanowski, Murdeshwar, 1990) acknowledge that bare metal contact is essential for bonding, it has been shown by Krzanowski (1989) through thin-film microanalysis using energy dispersive x-ray spectroscopy (EDXS) that significant diffusion does not occur in the short wire bonding time spans. This was also confirmed by him through diffusion distance calculations for the metal

systems examined.

Another investigation (Winchell, Berg, 1978) centered on the material flow response to a combined static and dynamic force system. In this study, Winchell and co-worker compared the bonding of aluminum wires to aluminum, glass, beryllium, and silicon substrates and observed the existence of a common bonding mechanism irrespective of the type of substrate used. The first of their two part mechanism proposed that the wire is softened by the wedge motion of the bonding tool and subsequent motion of a vertical machine load while the second part was characterized by a wave form which generated a strong cleansing action and an applied pressure at the bond interface. It was thought that this wave form initiated at the bond periphery and extended towards the center with time, hence the observation of a torus shaped region where bond formation occurred.

Krzanowski (1989) in a different approach from that of previous researchers, used high resolution TEM observations to investigate wire bonds. It should be noted that the earlier mentioned TEM study by Kreye was on ultrasonic spot welds and not on wire bonds. In his study, Krzanowski employed a unique cross-section TEM specimen preparation technique that enabled comparison to previously proposed wire bonding mechanisms. It was reported that during bonding the aluminum wire appeared to have undergone a transformation involving dynamic recovery or recrystallization and that the features normally associated

with plastic deformation were absent from the wire microstructure. Through direct examination it was shown that bond adhesion was due to interface formation similar to grain boundaries in polycrystalline metals. While analysis of the interface showed little evidence of either diffusion or melting, while debris, voids and entrapped particles were observed. It was therefore suggested that these were a result of dispersion of contaminants to low lying asperities which allowed for the formation of interfaces across which metal to metal contact occurred. Easterling et al. (Easterling, Tholen, 1972) demonstrated a similar principle in the case of metallic powders where clean metal surfaces were capable of bonding when in contact due to attractive forces that pulled them elastically together. Image matching techniques employed to analyze the observed elastic deformations showed that the formed junctions were due to metallic bonding. Among other things, it was also shown that small changes induced in contact geometry of the metal powders such as due to plastic deformation could substantially increase adhesion. This could very well be the critical step in ultrasonic wire bonding.

To further understanding of the bonding mechanism, relating the development of microstructures of both the wire and substrate in question before and after bonding needs to be done. It is known that applying cyclic stresses to a metal leads to development of fatigue-like microstructures, which are described in the subsequent sections.

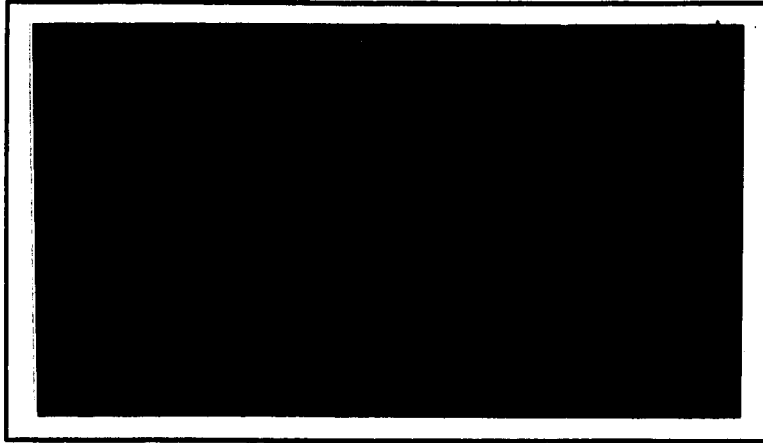


Figure 4 Schematic illustration of the Aluminum ultrasonic wedge wire bonding process. (From Krzanowski, Murdeshwar, 1990).

2.3 Fatigue Microstructures - Over the years laboratory testing of fatigue specimens have been conducted in bending, torsion, tension-tension, or tension-compression, using machines such as the Wohler or the Universal testing machine. The tests, usually 'low frequency' are in the range of a 100 Hz, although higher frequencies of up to a 1000 Hz can be obtained with more sophisticated means such as electro-resonance. However, with researchers becoming aware of material strength property changes due to ultrasonic irradiation such as that developed in high-thrust jet and rocket engines (Langenecker, 1963), 'high frequency' fatigue testing with the help of ultrasonically induced vibrations in the range upwards of 20 kHz, has taken on more meaning. In general, these tests are conducted (Maurer, 1970) with magnetostrictive or piezoelectric converters made of lead zirconate titanate. The amplitude of oscillation is transmitted to one end of the specimen over a $\lambda/2$ resonator and an acoustic velocity transformer. The length of the sample is kept at a half-wavelength of the ultrasonic wave so as to obtain resonance which builds up a sinusoidal or strain distribution along the axis of the specimen with a stress peak in the center.

The next two sub-sections discuss microstructures obtained through conventionally fatigued (or non-ultrasonic fatigue) and ultrasonic methods. Later, while discussing microstructural changes in the present study, reference to

these sections will be made whenever necessary.

2.3.1 Non-Ultrasonic Fatigue - It was recognized by Zhong and co-workers (Zhong, Jin, Zhou, Meng, Chen, 1990) that the cyclic stress-strain (CSS) curve for 310 stainless steel could be divided into three regions, each characterized by a change in slope of the saturation stress versus plastic strain curve. One method of obtaining the CSS curve is by drawing a line through the tips of the stabilized hysteresis loops obtained from specimens tested at different strain amplitudes. This curve then provides a convenient representation of the steady state cyclic stress - strain response of a material.

The dislocation substructure in each region of the CSS curve has been studied for different metals, such as 310 stainless steel (Jin, Zhong, Chen, 1990), ferritic steel (Roven, Nes, 1991), aluminum (Konig, Blum, 1980), copper (Feltner, Laird, 1967) and its alloys (Saxena, Antolovich, 1975). Reported observations of the substructure evolution with accumulating number of cycles along the CSS curve (Figueroa, Bhat, De La Veaux, Murzenski, Laird, 1981; Jin, 1989; Jin, Zhong, Chen, 1990; Doong, Socie, Robertson, 1990; Roven, Nes, 1991) includes dislocation loops, veins, unidirectional walls including the persistent slip band (PSB) ladder structures, labyrinth walls, cells and subgrains. One study on 310 stainless steel by Jin et al. (Jin, Zhong, Chen, 1990) demonstrated the above mentioned substructures in the

three regions of the CSS curve at plastic strain amplitudes ranging from 1×10^{-4} to 9×10^{-3} . Their micrographs reproduced here in Figs. 5-7 illustrate some of the observations at low, intermediate and high plastic strains. At low plastic strains, dislocations were said to be generated in many slip systems and found to be distributed quite uniformly. Typical dislocation structures such as pile-ups, individual dipoles and dislocation bundles can be seen at this plastic strain in Fig. 5. At intermediate plastic strains in Fig. 6, dislocation veins, tangles, or (110) walls were observed, while labyrinth walls, PSB ladders and misoriented cells were observed in Fig. 7, at high plastic strains. Using energy considerations Figueroa et al. (Figueroa, Bhat, De La Veaux, Murzenski, Laird, 1981) explained that the substructure evolution was a result of change to a more stable energy configuration. In another study (Roven, Nes, 1991), on the cyclic deformation of ferritic steels it was pointed out that the substructures observed in that investigation were similar to those observed in copper at the same plastic strain range. This indicated the necessity of a specific plastic strain range for a particular substructure independent of the metal crystal structure.

Several researchers (Konig, Blum, 1980; Saxena, Antolovich, 1975; Feltner, Laird, 1967) have made analogies between structures developed at low cyclic strains to stage I, and that of high cyclic strains to stages II and III of monotonic deformation while Roven et al. (Roven, Nes, 1991)

used the monotonic deformation curve and microstructural observations of cyclically deformed specimens to interpret the plateau in the CSS curve. It was explained by them using Fig. 8, that as the cyclic plastic strain range approached the elastic strain of the monotonic deformation curve, a majority of the grains accommodated considerable plastic displacements. The resulting compatibility stresses produced at grain boundaries enhanced multiple slip causing the transformation of the structure to cells and labyrinth walls. In fact the presence of this plateau in the CSS curve has been cause for much debate and further discussion on it would be outside the scope of the present work. It may suffice at this point to mention that Roven et al. observed a plateau only for large grained metals and it is generally agreed (Figuroa, Bhat, de la Veaux, Murzenski, Laird, 1981; Mughrabi, Herz, Stark, 1981; Jin, 1989) that this is associated with an increase in the number of PSBs.

It is understood that a prerequisite for the formation of these PSBs (Jin, 1989) and in general, for substructure evolution, is the ease of cross slip characterized by the largest possible annihilation distance of opposite screw dislocations. This depends on the stacking fault energy (SFE), temperature, strain amplitude and crystal orientation. Saxena et al. (Saxena, Antolovich, 1975) demonstrated the substructure evolved during low cycle fatigue (LCF) tests on four different Cu-Al alloys. It was observed by them in Figs.

9 and 10 that Cu (55.0 ergs/cm^2) and Cu-2.2Al (31.5 ergs/cm^2) always formed cells while dislocation bands and tangles were said to be observed for Cu-4.2Al (13.0 ergs/cm^2) in Fig. 11, at low plastic strain ranges. At high plastic strain ranges they reported the formation of elongated cells. This observation was reasoned by them to be due to cross slip becoming more frequent with increase in stress, resulting in cell formation. For Cu-6.3Al (5.5 ergs/cm^2) in Fig. 12, dislocation bands were observed at all strain ranges along with individual planar dislocations. Doong and co-workers (Doong, Socie, Robertson, 1990) demonstrated the above stated effect of SFE on the substructure using proportional and non-proportional loading on three materials, Al, Cu, and stainless steel each exhibiting a different slip mode.

The temperature effect on dislocation structure for OFHC Cu and 304 stainless steel was examined by Abdel-Raouf and co-workers (Abdel-Raouf, Plumtree, Topper, 1974). It was shown by them that the cyclic stress response is inversely related to the cell size for Cu cycled at different temperatures ranging from -75°C to 650°C . Fig. 13 and 14 present their observations for 304 stainless steel which underwent a change from planar to wavy slip character as the temperature changed from room temperature to 760°C . The cell size observed at elevated temperatures was found to increase with temperature.

Strain amplitude effects on cross slip and the resulting dislocation substructure were examined by Figueroa et al.

(Figueroa, Bhat, de la Veaux, Murzenski, Laird, 1981), whose observations on the cyclic strain response of Cu at low strains were schematically summarized and reproduced here in Fig. 15. They reported a change in the dislocation substructure from a loose distribution of dipoles at $\epsilon_p = 2 \times 10^{-5}$ to cells at $\epsilon_p = 2 \times 10^{-3}$ with an increase in strain.

Crystal orientation and its effect on the substructure were investigated by Jin and co-worker (Jin, Winter, 1984). A schematic interpretation used by them in Fig. 16 stated that in region A, a single slip system was active resulting in PSB ladders and matrix veins. The dislocation interaction between systems in region B produced Lomer-Cottrell locks resulting in a structure similar to region A. In region C they reported the formation of sessile jogs while in region D, a cell-like structure was said to be formed due to locally active multiple slip as a result of the co-planar dislocations.

In summary, metal cyclic fatigue causes a dislocation substructure evolution. This evolution is a result of cross slip resulting in a saturated structure affected by the strain amplitude, temperature or SFE. Initially defects in the form of dipoles and jogs lead to PSBs and softening along the plateau region of the CSS curve. The PSBs further transform to cells and subgrains as the CSS curve shows a drastic increase in slope indicating hardening.

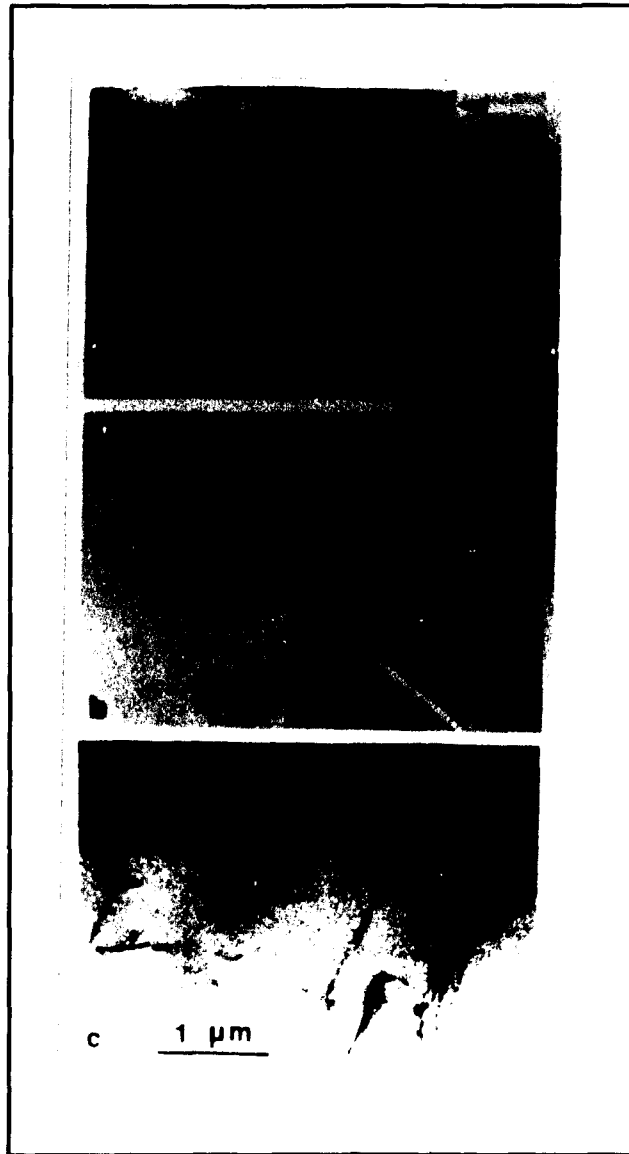


Figure 5 Dislocation configurations in 310 stainless steel at $\epsilon_p = 5.0 \times 10^{-4}$. (a) dislocation pileups; (b) individual dislocations; (c) bundles of long dislocations. (From Jin, Zhon, Chen, 1990).



Figure 6 Dislocation configurations in 310 stainless steel at $\epsilon_p = 2.4 \times 10^{-3}$. (a) Loose arrangement (left) and dislocation tangles (right); (b) dislocation veins; (c) embryos of PSB ladder; (d) well developed walls. (From Jin, Zhon, Chen, 1990).

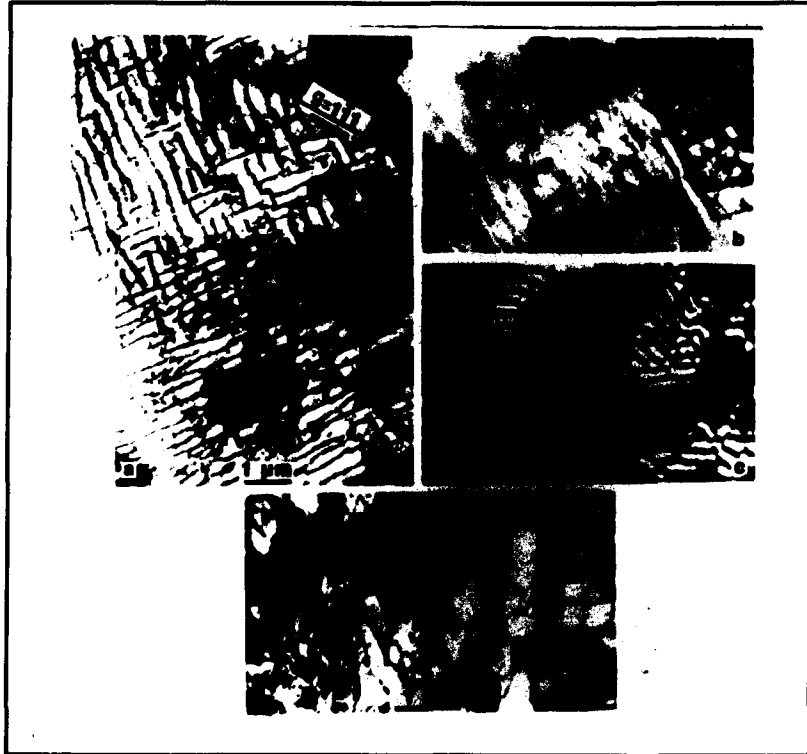


Figure 7 Dislocation configurations in 310 stainless steel at $\epsilon_p = 8.8 \times 10^{-3}$. (a) Labyrinth structure; (b) PSB ladder structure; (c) Two sets of inclined dislocation walls (d) Dislocation cells. (From Jin, Zhon, Chen, 1990).

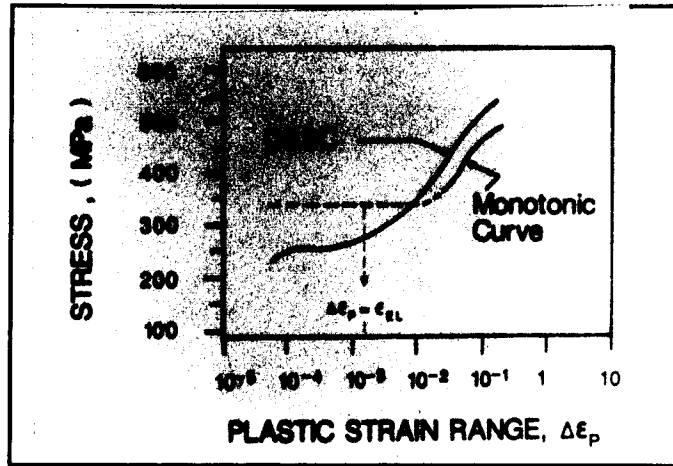


Figure 8 The cyclic stress-strain and monotonic tensile test curves for a commercial low alloyed steel. (From Roven, Nes, 1991).



Figure 9a Low cycle fatigue substructure of Cu at $\epsilon_p = 0.0017$; 0.0124 . (From Saxena, Antolovich, 1975).

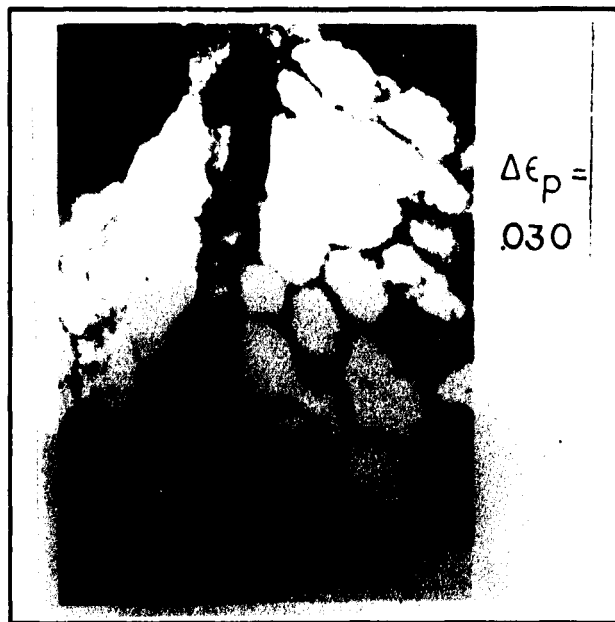


Figure 9b Low cycle fatigue substructure of copper at $\epsilon_p = 0.030$. (From Saxena, Antolovich, 1975).

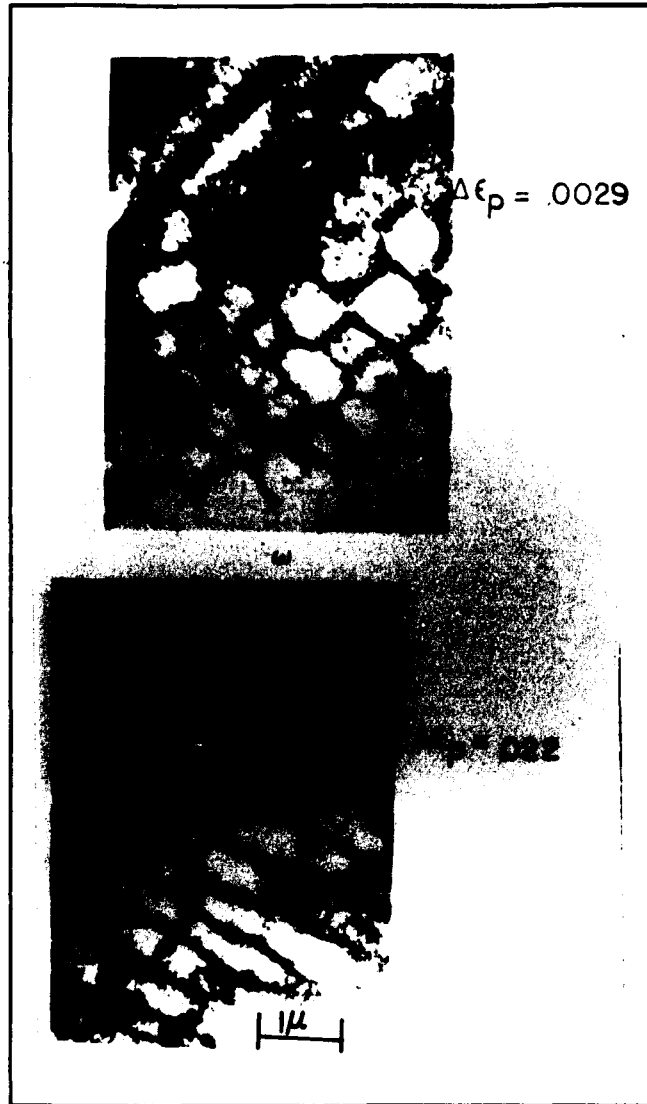


Figure 10 Low cycle fatigue substructure of Cu-2.2Al at $\epsilon_p = 0.0029$; 0.022 . (From Saxena, Antolovich, 1975).

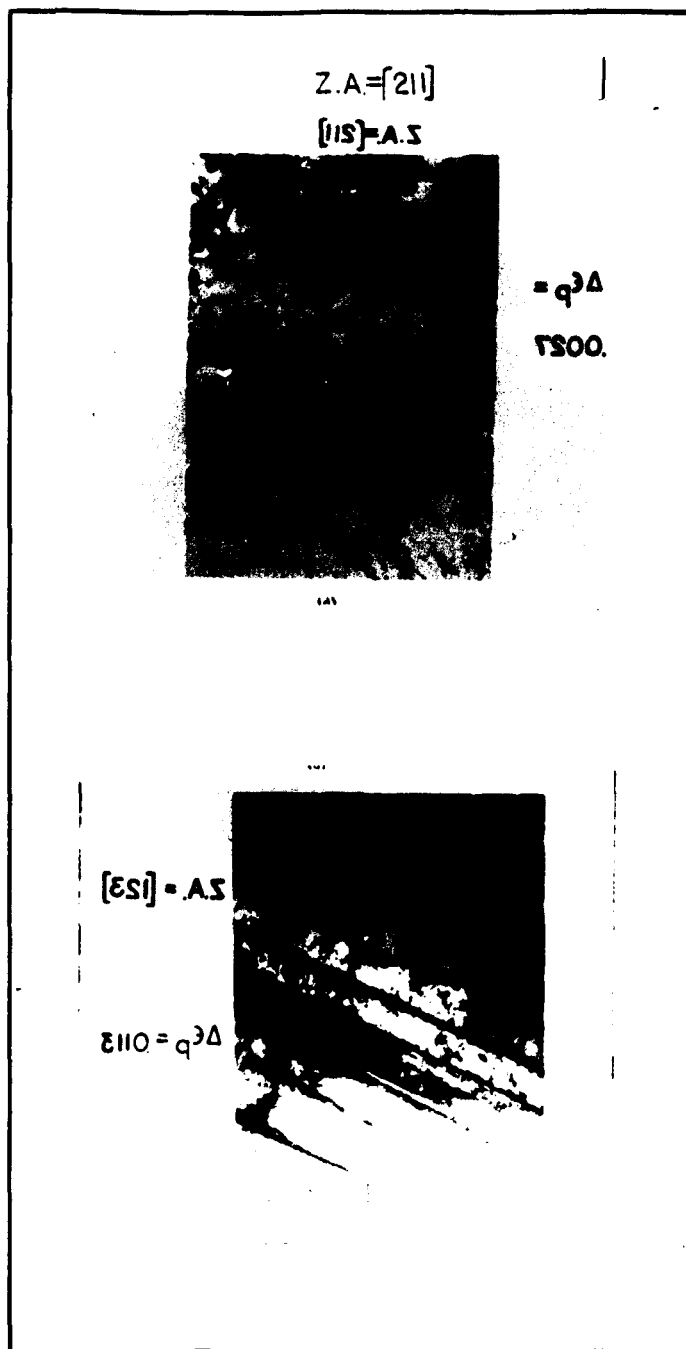


Figure 11 Low cycle fatigue substructure of Cu-4.2Al at $\epsilon_p = 0.0027$; 0.0113 . (From Saxena, Antolovich, 1975).

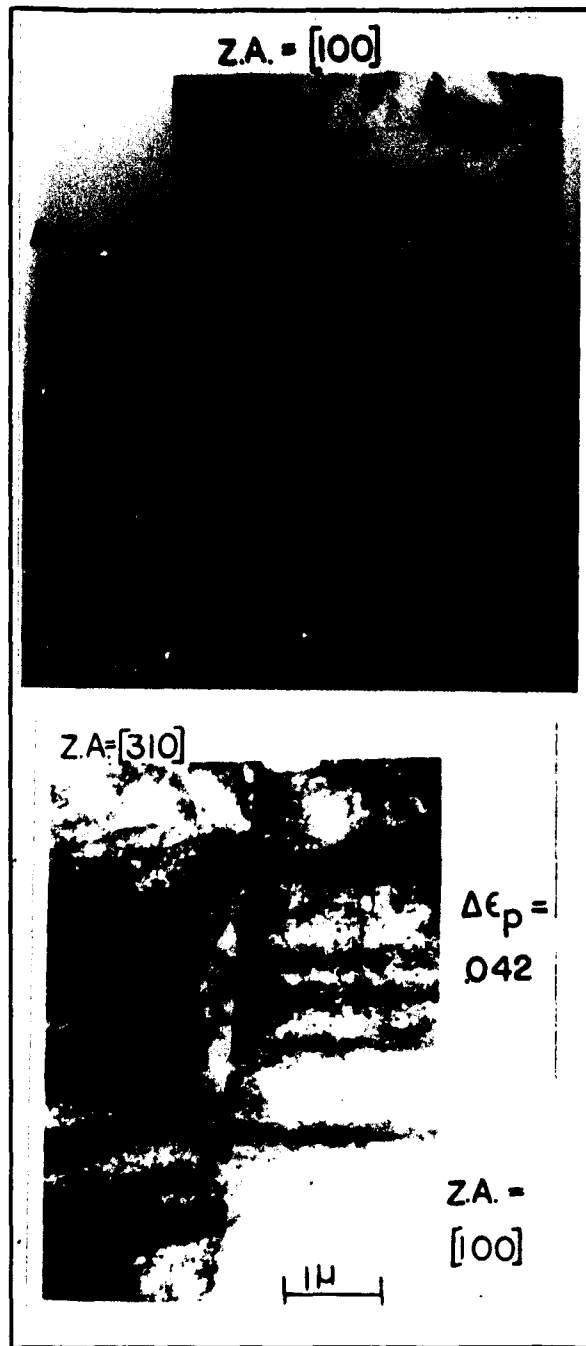


Figure 12 Low cycle fatigue substructure of Cu-6.3Al at $\epsilon_p = 0.0025; 0.042$. (From Saxena, Antolovich, 1975).

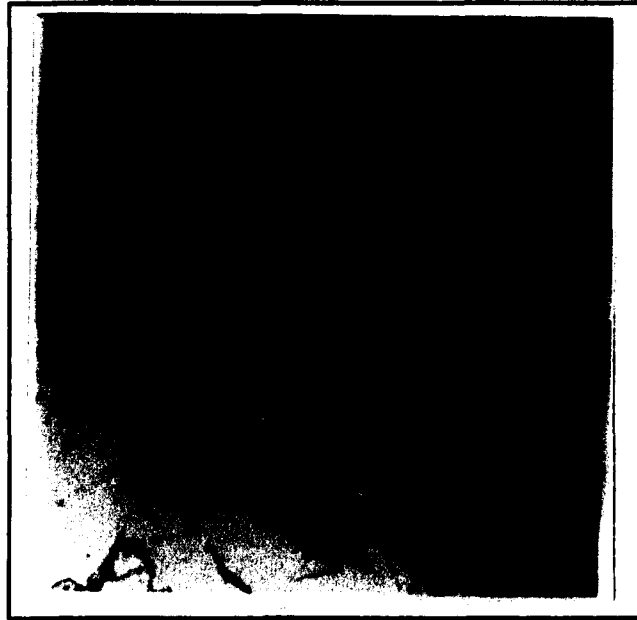


Figure 13 Planar arrays of dislocation in 304 stainless steel cycled at $\epsilon_p = 0.020$ at 25°C. (From Abdel-Raouf, Plumtree, Topper, 1974).

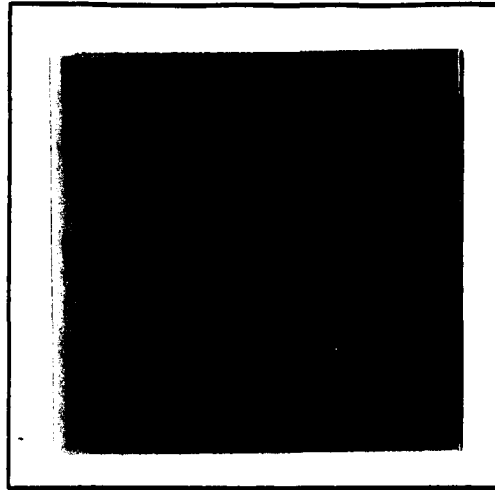


Figure 14 Cell formation in 304 stainless steel cycled at $\epsilon_p = 0.20$ at 25°C. (From Abdel-Raouf, Plumtree, Topper, 1974).

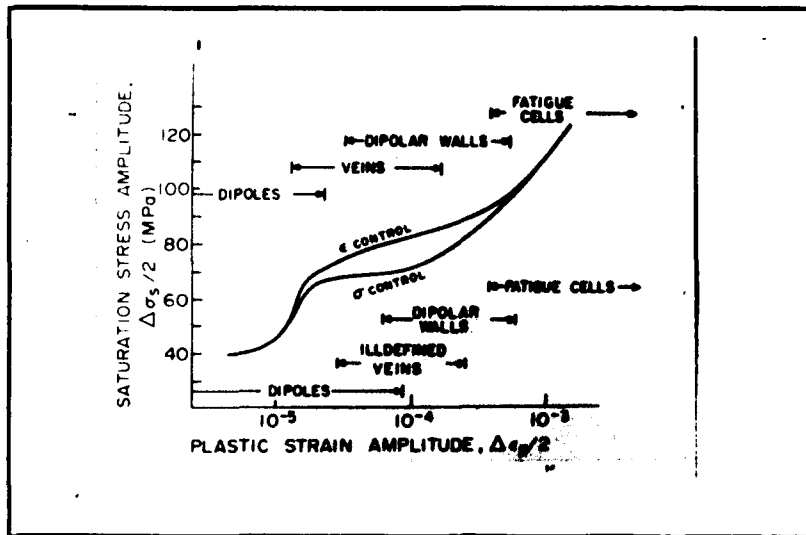


Figure 15 Schematic representation of the dislocation stress present at saturation in low amplitude fatigue of copper. Well defined loop patches have been named 'veins' in this representation. (From Figueroa, Bhat, De La Veaux, Murzenski, Laird, 1981).

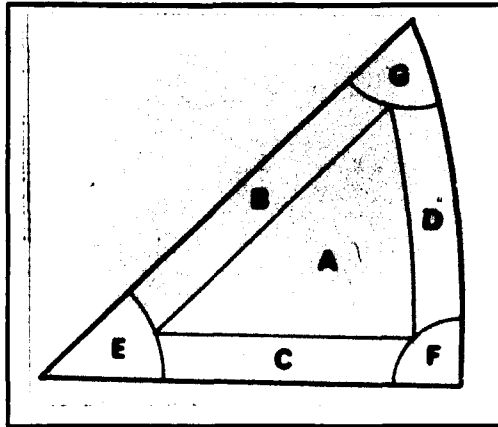


Figure 16 Various dislocation structures formed in different oriented crystals. (From Jin, Winter, 1984).

2.3.2 Ultrasonic Fatigue - In Section 2.1 the effect of ultrasound on metal strength properties were discussed. The present section deals with microstructures of ultrasounded metals, said (Kralik, Weiss, 1967; Hokenhull, Hacking, 1970; Maurer, 1970; Weiss, 1970) to be closely related to specimens fatigued about the zero mean stress. Although the microstructures are somewhat similar, there is a distinction between the mechanism of fracture in non-ultrasonic and ultrasonic frequency fatigue (Roth, Wilertz, Leax, ; Mason, 1970; Wood, MacDonald, 1970). In the former, slip occurs throughout the whole grain with fatigue fracture occurring along crystal grain boundaries while in the latter, slip bands form in adjacent grains along different directions which for longer times of vibration and higher strains develop into microcracks. The sample finally fatigues completely with the joining of microcracks in adjacent grains. Mason explained that low frequency fatigue fracture could be brought about at higher frequencies by going to high temperatures. At low temperatures, he stated, that there was insufficient time during a cycle for new dislocations to climb out of the slip plane, and microcracks occurred by debris build up in the slip plane. At high temperatures on the other hand, dislocations climbed out of the slip plane by diffusion and slip therefore occurred over the whole grain.

In one study, somewhat similar to that described in the previous section on non-ultrasonic fatigue, Weiss (1970)

examined substructures which evolved as a result of ultrasonic fatigue of polycrystalline Cu, with the increase in yield point plotted as a function of strain amplitude (Fig. 17). A frequency of 20 kHz was used in these tests with the ultrasonic generator capable of delivering a maximum output of 200 W. The microstructural observations reported in the study are reproduced here in Figs. 18-22. The substructure observed in the linear portion of the curve including that subsequent to the application of ultrasound consisted of various dislocation tangles and jogs (Fig. 18). In the steep portion of the curve the density of dipoles and dislocation loops were said to increase resulting in an alignment in the $\langle 112 \rangle$ directions (Fig. 19). Also, in this region of the curve (Fig. 20), dislocation patches as a function of grain orientation were reportedly observed. After a certain strain, there was no increase in yield stress and the reported microstructure (Fig. 21) consisted of dislocations rearranged in narrow regions. Finally, the structure (Fig. 22) was reported to be characterized by dislocation cells formed in the fractured area.

Another investigation by Westmacott and co-worker (Westmacott, Langenecker, 1965) on annealed aluminum wire subjected to ultrasound reported similar observations to explain acoustic hardening damage. Their micrographs reproduced here in Figs. 23 and 24 show a well-formed cell structure containing subgrains mostly in directions parallel

to the traces of (100) planes. Fig. 23 exhibits the differences observed in dislocation arrangements within a subgrain boundary said to range from highly irregular tangles to regular hexagonal networks. They also observed dislocation loops and dipoles in many areas of the specimen which in some cases such as in Fig. 24, were associated with an irregular subgrain boundary.

To understand the effect of dynamic recovery over SFE in structure evolution, Shea et al. (Shea, Rao, 1982) investigated microstructural changes in annealed 304 stainless steel resulting from high temperature ultrasonic vibrations. To eliminate the effect of SFE which is an important parameter controlling substructure evolution at temperatures below 300°C, their investigation was conducted at 925°C. Reported observations included an increase in surface hardening attributed to the increased dislocation density, deformation twinning and enhanced precipitation of dispersed $M_{23}C_6$ carbide. Fig. 25, reproduced from their study, demonstrated a typically observed area consisting of deformation damage, dislocation cell and subboundary formation near a high-angle grain boundary. Grain boundary $M_{23}C_6$, equiaxed cells and cell refinement were also observed in this ultrasounded substructure. Preferential transport of ultrasonic waves through the surface region was stated (Puskar, 1972 as referenced in Shea, Rao, 1982) to result in higher dislocation density and resulting surface hardness. Also in this study, it

was stated that both grain (Li, 1963, as referenced in Shea, Rao, 1982) and twin (Hornbogen, 1963, as referenced in Shea, Rao, 1982) boundaries are important sources for dislocation generation, especially when steps are present. At ultrasonic frequencies these effects are said (Zener, 1938, 1948; Schoeck, 1969, as referenced in Shea, Rao, 1982) to be pronounced due to larger dissipation of energy. Such defects have also been detected through electric resistance measurements on ultrasonic fatigue (Weiss, 1970) and wire bond specimens (Joshi, 1971). Maurer (1970), through a TEM investigation on fatigue specimens, reported that dislocation loop densities were higher in ultrasonic fatigue than in non-ultrasonic fatigue at comparable strain amplitudes. This, he suggested, could be associated with the increase in the number of vacancies produced during high speed deformation.

Further evidence of ultrasonic vibration on metal structure was reported by Fairbanks (1970). Based on his observations, he concluded that ultrasounding a heat-treated cold worked metal made it easier for recovery and polygonization to occur within the cold worked metal than recrystallization. However, he stated, that if recrystallization occurred, then a more uniform structure was obtained.

In summary, microstructures of metals subjected to ultrasonic fatigue are almost similar to that of non-ultrasonic fatigue. The difference that exists in the two

resulting microstructures is in the amount of defects present. These defects initially exist in the form of jogs and dipoles which finally lead to the formation of cells.

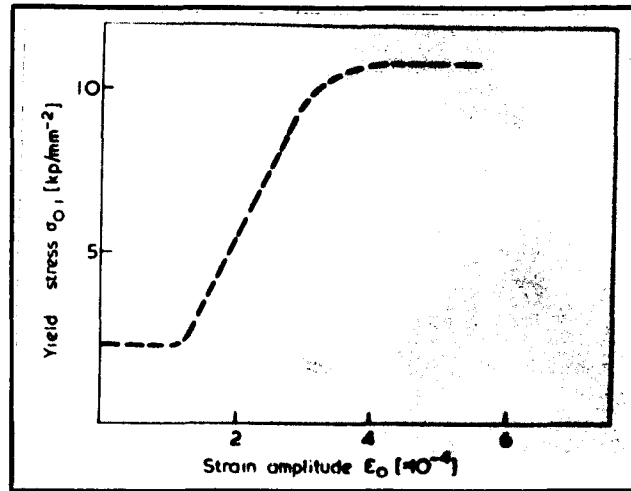


Figure 17 Cyclic stress-strain curve for copper at room temperature at 6×10^5 cycles. (From Weiss, 1970).

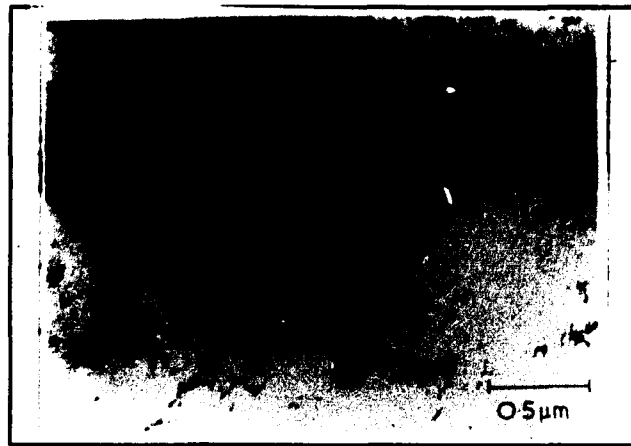


Figure 18 Polycrystalline Cu subjected to ultrasonic fatigue at 6×10^5 cycles and a strain amplitude of $< 2 \times 10^{-4}$. (From Weiss, 1970).

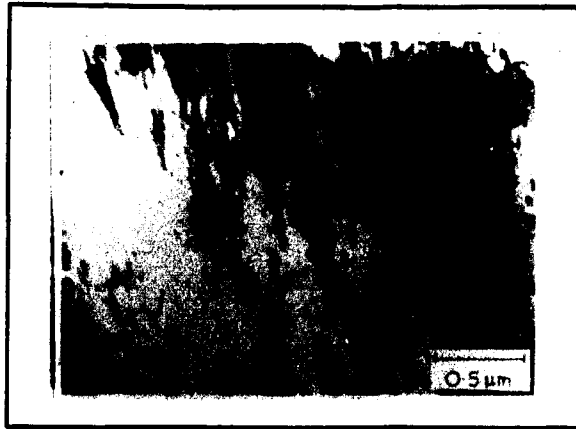


Figure 19 Polycrystalline copper subjected to ultrasonic fatigue at 6×10^5 cycles and a strain amplitude of $\approx 2-3 \times 10^{-6}$. (From Weiss, 1970).



Figure 20 Polycrystalline copper subjected to ultrasonic fatigue at 6×10^5 cycles and a strain amplitude of $\approx 2-3 \times 10^{-6}$. (From Weiss, 1970).

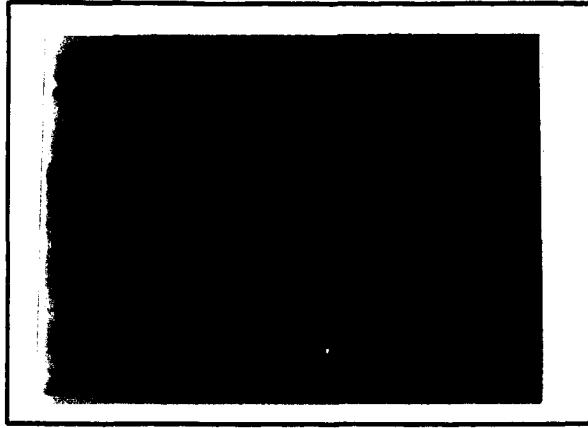


Figure 21 Polycrystalline copper subjected to ultrasonic fatigue at 6×10^5 cycles and a strain amplitude of $\approx 4-5 \times 10^{-4}$. (From Weiss, 1970).

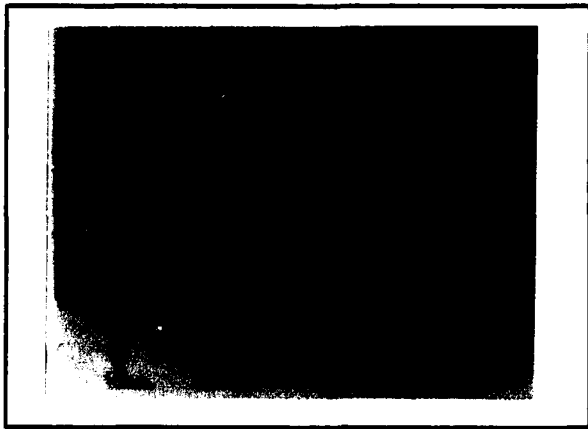


Figure 22 Polycrystalline copper subjected to ultrasonic fatigue at 6×10^5 cycles and a strain amplitude of 5.5×10^{-4} . (From Weiss, 1970).

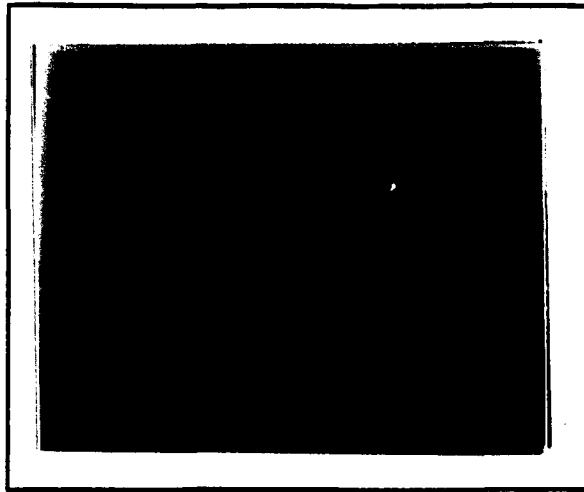


Figure 23 Ultrasonically irradiated aluminum showing sub-boundaries consisting of dislocation networks. (From Westmacott, Langenecker, 1965).

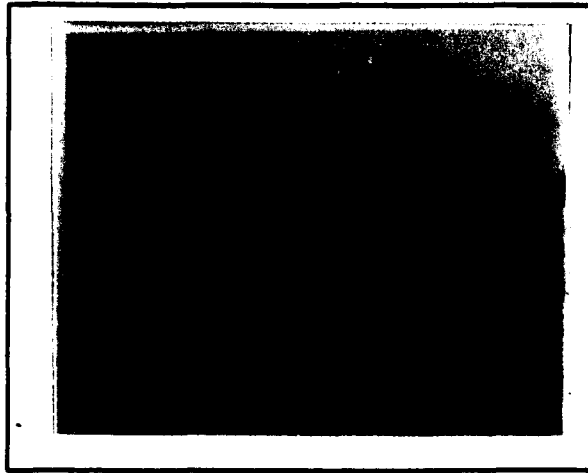


Figure 24 Ultrasonically irradiated aluminum showing high dislocation loop density in vicinity of sub-boundary; loops are 100-1000 Å in diameter; plane of foil is (312). (From Westmacott, Langenecker, 1965).

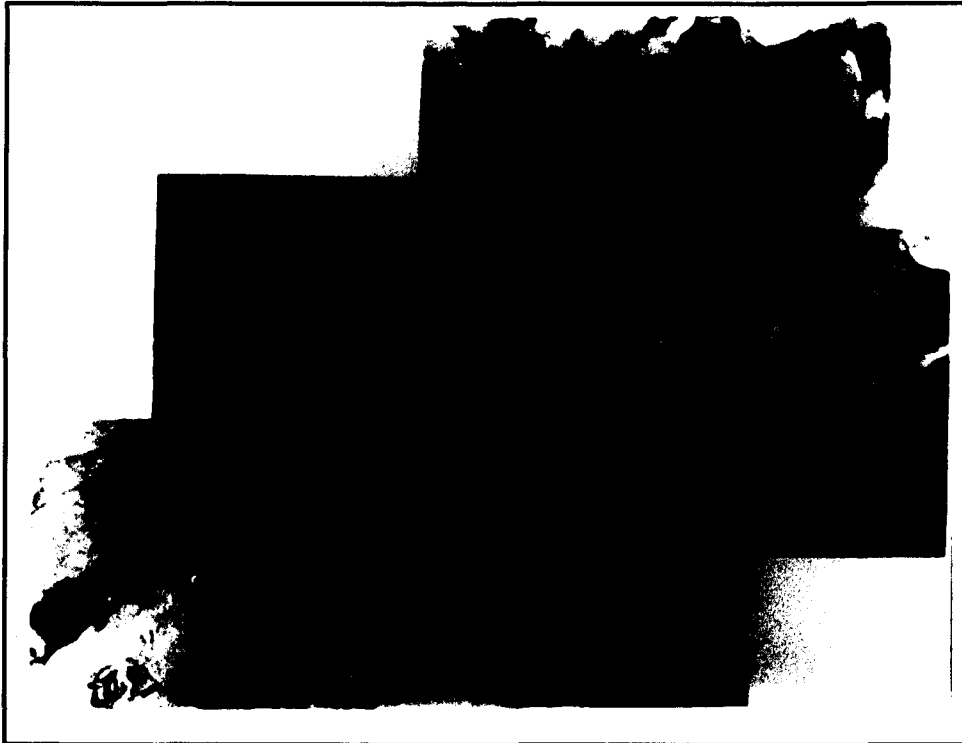


Figure 25 Composite bright field micrograph showing extensive deformation damage and dislocation cell and sub-boundary formation near a high angle grain boundary (GB) in the core of the specimen. Grain boundary $M_{23}C_6$ (C), equiaxed cells (E), and cell refinement (R) can also be seen. (From Shea, Rao, 1982).

2.4 Interfacial Reactions and Reliability - Dissimilar metals in contact can react at the interface under favorable conditions of temperature and pressure and form a reaction product. The reaction product, called an intermetallic compound, affects bond reliability and component performance over a period of time. The present section reviews possible Au-Al and Ni-Al intermetallics that could form during Al wire bonding to Au and Ni substrates.

The initial growth rate of an intermetallic is reported (Mehl, 1936; Lustman, Mehl, 1942; Kidson, 1961) to follow a parabolic relationship of the form,

$$x = K t^{1/2},$$

where x is the intermetallic layer thickness, t is the time. The rate constant,

$$K = C \exp (-Q/RT),$$

where C is a constant, Q is the activation energy for layer growth, R is the gas constant and T is the absolute temperature ($^{\circ}\text{K}$). The value of K changes for each intermetallic phase, and is dependent upon the neighboring phases which supply additional Au and Al for continued formation.

Au-Al System - Fig. 26 shows the Al-Au phase diagram with the five probable intermetallic compounds namely, AuAl_2 , AuAl , Au_2Al , Au_3Al_2 and Au_4Al . In studies on bulk samples, such as that done by Philofsky (1970a) on bonds formed by joining

high-purity Al and Au wires by butt-welding, all of the five Au-Al intermetallics were observed. These intermetallics identified by their distinct colors were also confirmed by electron microprobe. The purple phase, AuAl_2 , was observed to be present in minute quantities. At temperatures above 400°C small voids were observed in the phase attributed to the Kirkendall effect. The voids were said to be caused by vacancies piling up, and condensing as a result of Al diffusing out of the phase faster than the Au could move in the other direction. After 100 min at 460°C , these voids were observed to form a continuous line thus weakening the strength of the couple. The white phase, AuAl , was observed at long times and low temperatures or at high temperatures which, according to Philofsky indicated a difficulty in nucleation. This phase reportedly grew into the tan phase Au_2Al , which nucleated slowly but once nucleated was observed to grow at the second fastest rate. The fastest growing phase, Au_3Al , was also tan in color and was observed to nucleate immediately. Voids were also observed in this phase at temperatures above 300°C at the Au rich side while above 400°C , cracks were observed to nucleate and grow along the void line. It was presumed that these cracks were a result of stresses generated by thermal expansion differences between the phases on cooling to room temperature. The Au_4Al phase was reported to be present in most of the specimens and was said to grow at a very slow rate. Another observation reported (Philofsky,

1970b, 1971, as referenced in Horsting, 1972) in these investigations were that the strength of all intermetallics formed were higher than that of individual metals in the annealed condition and were not the cause for bond failure. In fact, it was shown that Kirkendall voids formed as a result of diffusion coalesced leading to ultimate bond failure. Bond failure was shown to be enhanced by thermal cycling.

Interfacial reactions have also been studied on Au-Al thin films. Campisano et al. (Campisano, Foti, Rimini, 1975) suggested that the end phases in Au-Al thin film reactions were dictated by phase equilibrium predicted from the phase diagrams while the formation of the intermediate compounds determined by nucleation rate and growth kinetics had to be determined experimentally. A qualitative model proposed by Majni et al. (Majni, Nobili, Ottaviani, Costato, 1981) included both thermodynamic and kinetic arguments to interpret the sequence of the observed intermetallics formed. In their study on Au-Al thin films, Majni et al. reported the sequence of these phase transformations using Rutherford backscattering and XRD techniques. It was observed that Au_5Al and Au_2Al were the first and second phases to be formed. Subsequent phase formation was said to be strongly dependent on sample preparation. Depending on the amounts of Al and Au present in the samples, the end product of the phase transformation was observed to be $AuAl_2$ for $Au \ll Al$, $AuAl$ for $Au = Al$, Au_2Al for $Au = 2Al$, Au_5Al_2 for $2Au = 5Al$, or Au_4Al for $Au \gg Al$.

Ni-Al System - When compared with Au-Al bonding, the Ni-Al system is highly reliable although problems have been reported with initial bond formation. Most bonding is done to Ni which is deposited using boride or phosphide electroless plating solutions. Reliability problems have been noted when Al is bonded to Ni electroless plating with a significant amount of co-deposited phosphorous.

Fig. 27 shows the Ni-Al phase diagram with the four possible intermetallic compounds designated as β (NiAl₃), γ (Ni₂Al₃), δ (NiAl) and ϵ (Ni₃Al). Castleman and Seigle (1958) examined the formation of these intermetallic layers in spot-welded Ni-Al bonds. After annealing for several hundred hours at 600°C they observed the γ and β phases with very thin layers of δ and ϵ phases.

In another study, Coglán et al. (Coglán, Nastasi, Mayer, 1985) investigated the phase formation and decomposition in the thin-film Ni-Al system between 300 and 425°C. It was reported that the initial reaction started at the interface in contact with the most Al-rich film resulting in the formation of NiAl₃. Subsequent reactions led to the formation of Ni₂Al₃.

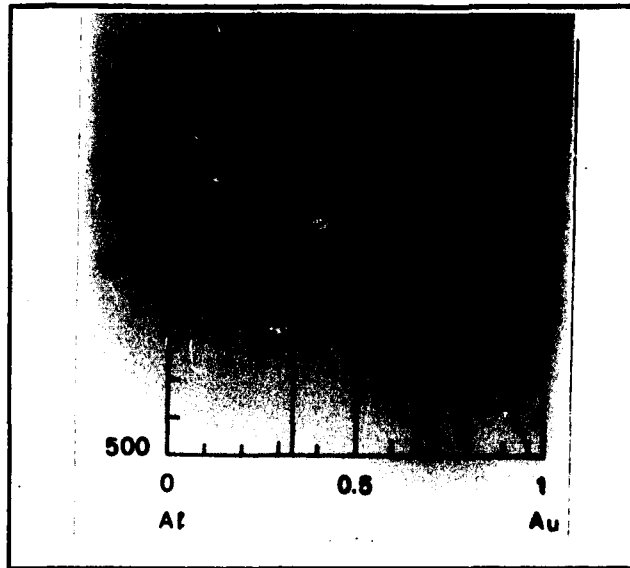


Figure 26 Phase diagram of Au-Al.
(From Majni, Nobili, Ottaviani,
Costato, 1981.)

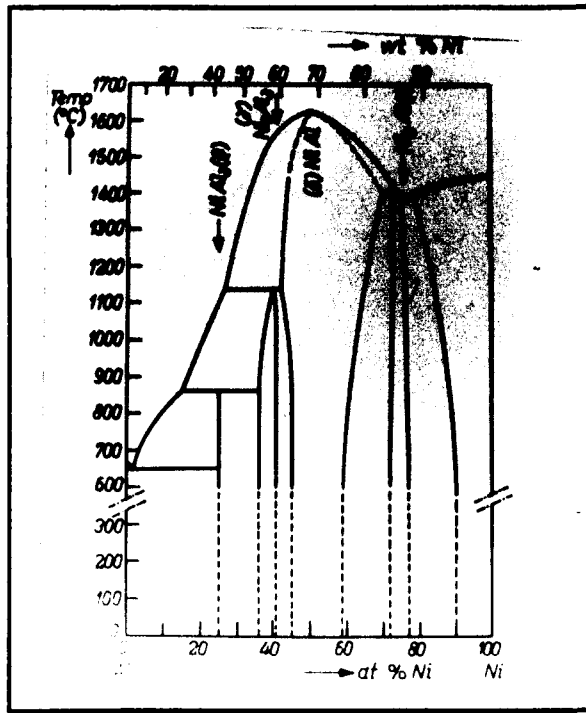


Figure 27 Phase diagram Ni-Al.
 (From Janssen, Rieck, 1967).

2.5 Summary and Research Outline - In an earlier paper Krzanowski (1989) demonstrated the advantages of using the TEM for examining wire bonds. The resolution and contrast mechanisms of the TEM in observations of metallurgical features such as precipitates, dislocations, grain boundaries and other planar defects is superior to previously used techniques. The present study employs TEM techniques to fully characterize the UBW process. Since TEM observations are restricted to extremely thin (<500 nm) electron transparent specimen areas, specimen preparation is extremely critical and unique techniques were developed as part of this research program.

First, the bonding wire, Al substrate and wire/substrate interface were examined. The wire and substrate surprisingly showed well-recovered microstructures despite considerable deformation in the wire during bonding. Examination of the bond interface in cross section view specimens showed a polycrystalline grain structure. The occasional contaminant trapped at the interface served as sources for dislocation emission in an otherwise well-recovered structure.

In subsequent research, microstructural transformation of metal substrates with different σ_{ys} , recrystallization temperature, SFE, τ_{crit} , diffusion properties and hardness were studied. The observed microstructural transformations in these substrates were compared with non-ultrasonic fatigue cycled specimens and the substructure evolution along the CSS curve.

In addition to σ_{ys} , SFE and diffusion properties, substrate transformation was also shown to be affected by bonding time and ambient temperatures. All these factors were incorporated into a model developed to estimate the extent of microstructural transformation.

Electronic components during service experience different temperatures which could result in intermetallic formation. The formation of brittle intermetallics or Kirkendall voiding could affect bond reliability. Therefore in a subsequent phase of this study, thermally induced microstructure transformations at the bond interface were examined. In this phase, microstructures of bonds to plated substrates subjected to different temperature conditions, such as annealing at various time periods or thermal aging, were studied. Intermetallics formed during the process of annealing and aging were identified in a scanning transmission electron microscope (STEM) and their effect on bond reliability measured as a function of bond strength.

Finally the UWB process was characterized in terms of substrate hardness, roughness and contamination using mechanical tests to measure bond strength. Based on these tests optimum surface roughness for good bonding could be determined for a particular metal substrate. A wire bonding mechanism could then be proposed from these and other experimental observations of this research.

CHAPTER III

EXPERIMENTAL METHODS

3.1 Materials - The bonding wires used in this study were 3 mil (75 μm) diameter Al-0.5 wt.% Mg wires, or 2 mil (50 μm) diameter Al-2.0 wt.% Si wires.

Microstructure transformations during bonding were studied on pure Al, 2024 Al, 6061 Al, commercially manufactured Ni (Ni 200, having a nominal composition of 99.5% Ni, 0.08% C, 0.18% Mn, 0.2% Fe) 0.06 mm thick foils, pure Cu (99.985%) 0.095 mm thick foils, pure Ni (99.99%), ETP Cu, ambralloy (Cu-8%Al), brass (Cu-30%Zn) and 304 stainless steel substrates. These materials were used in the annealed, cold worked, as-received, solutionized or peak-aged states as described in the thesis.

Microstructure transformations after bonding, that is, on thermally induced bond/substrate transformations, were studied on commercially manufactured Ni foil and different types of platings. These platings, on 0.125 mm thick Cu panels are described below.

Ni-P/Immersion Au : The nickel-phosphorous and immersion gold

were both plated by electroless processes. The target thickness was 5 μm of Ni-P and 0.1 μm of immersion Au. The Au was plated as soft Au, with no bath hardeners. A scanning transmission electron microscope (STEM) microanalysis showed that the Ni-P plating contained 6-7.5 wt.% P and had an amorphous structure while the immersion Au had a fine columnar grain structure. This type of substrate metallization will be referred to as "thin-gold".

Electroless Ni-Boron : Cu substrates were first plated with Niklad 4003¹ at 38-43°C for one minute, and then plated with Niklad 752¹ at 71°C to a thickness of 5 μm . The resulting deposit contained a maximum of 1% boron and an ultrafine (20-50 nm) grain structure.

Electroplated Ni/Au : Cu substrates were electroplated with Ni and soft Au. Measured thicknesses were 8.3 μm of Ni and 1.5 μm of Au. This type of substrate metallization will be referred to as "thick-gold".

Substrates used in examining hardness, roughness and contamination effects on the bonding process were annealed pure Al (99.99%) and 304 stainless steel.

3.2 Mechanical Testing - Bond strength is commonly measured by a pull test (ASTM Standards F459-84) or a shear test. In the

¹ Niklad is a registered trademark of Witco Chemical Corporation.

former (Joshi, 1971), two bonds are made, and the loop between them pulled to cause either wire or bond break. While in the latter (Maiocco, Smyers, Kadiyala, Baker; 1989), the bond is sheared off by means of a tool.

Fig. 28, from an earlier work (Joshi, 1971) on the formation of UWB between metals is reproduced here to better explain the competing processes that occur during bonding. The bond quality factor defined as q is the ratio of the bond shear strength to the initial wire strength. For a particular wire and substrate, an optimum combination of power, clamping force and bonding time results in strong bonds. If two of these parameters are held constant and the third one varied, then the bond quality factor varies according to curve (a) in Fig. 28. Competing with the bond growth is the degradation of wire strength and consequentially higher bond heel strength from acoustical fatigue and dynamic compressive deformation in accordance with curve (b) in Fig. 28. Thus, as the bond grows stronger, the wire becomes weaker and the failure mode on pulling changes from bond failure to wire failure. As the optimum region, indicated by the dotted rectangle, was approached, a noticeable decrease in the scatter data was observed by Joshi. It is this region that is desired in actual UWB application.

In pull tests conducted as part of this study, the region of curve (a) in Fig. 28 just before the dotted rectangle was sought ensuring weak bonds causing clean bond breaks instead

of wire breaks. Bond breaks resulting in strengths lower than a specific value, in this case, a quality factor of 0.25, were not included. Wire breaks were also considered as irrelevant data.

Fig. 29 shows the pull test apparatus used in the research. The substrate with bonds to be tested was clamped onto a 10-pound SM-10 Interface load cell connected to a DC strain gage conditioner and a plotter. Prior to testing the load cell was calibrated with known weights in the range of the expected bond strengths ensuring accuracy of readings. A thin tungsten hook used to pull the bonds was fitted to a threaded member capable of movement in the vertical direction and belt driven by 1/4 HP, 1 rpm motor. Pull strengths were recorded using a plotter.

Subsequent mechanical tests on plated substrates involved a modification of the pull-test described above and will be referred to as "Bondability" tests. In these tests the clamping force on all substrates tested for a specific bonding time and power was varied to get similar pull strength values, with minimal scatter. The clamping force now indicated the ease of bonding, or the bondability of a particular substrate relative to another. These tests were conducted on the different types of platings used in this research.

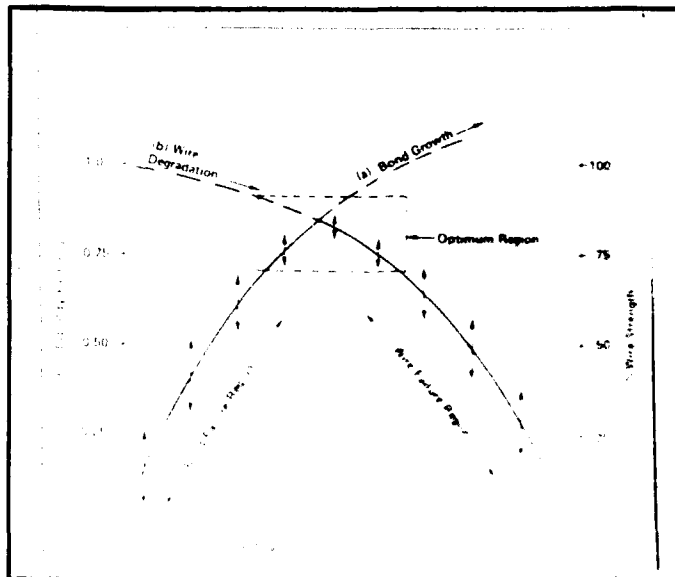


Figure 28 Competing processes during bonding (From Joshi, 1971).

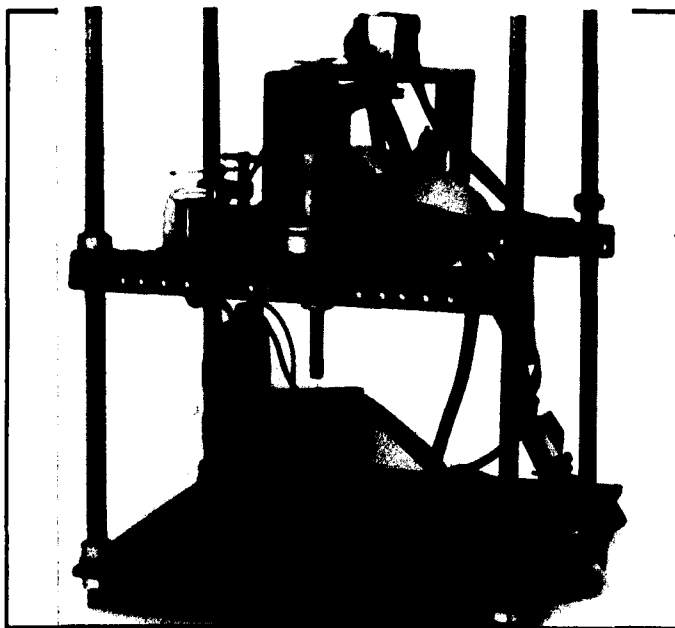


Figure 29 Bond pull-test apparatus.

3.3 TEM specimen preparation - As previously mentioned, TEM analysis involves very intricate and careful specimen preparation techniques. This is because the electron beam has to penetrate the specimen. Therefore specimen sections have to be sufficiently thin (approximately 100 nm or less) to be considered useful enough for TEM analysis. Described below are two unique techniques designed specially for this research.

Cross section view specimen preparation : Fig. 30 schematically illustrates the method used for preparing a cross section specimen. Wires were bonded to a metal foil substrate after which the wire loops were removed leaving only the bonded portion of the wire on the substrate. Next, 3.0 mm diameter holes were punched into a 0.2 mm thick Cu sheet. These holes were filled with a Ag-loaded epoxy called Epo-Tek H20E. The specimens were then placed into the epoxy so that the interface between the wire and substrate was vertical to the plane of the epoxy disc. The specimens were then cured for 90 minutes at 90°C, after which they were removed from the Cu sheet. The samples were put through a series of polishing treatments and dimpled as shown in the figure. After dimpling, the wire/bond interface was exposed on both sides of the disc. In the next step, depending upon the type of metals involved, specimens were either jet-polished or ion milled to electron transparency. Jet-polishing was done in a twin jet Fischone electropolisher using a solution of 15 or 25% HNO₃ in methanol

at -35°C . In the case of stainless steel, jet-polishing was done in a solution of 300 ml methanol, 42 ml butyl cellulose, 32 ml perchloric acid and 53 ml distilled water at -3°C . Ion milling was done at room temperature in a Balzer universal ion beam etching machine using 4-5 KeV argon ions.

Plan view specimen preparation : Plan view specimens were made from 3.0 mm diameter discs punched from metal foil substrates and reduced to 140 μm by grinding on a 600 grit paper. Specimens were then jet-polished using solutions similar to those described above. Initially specimens were jet-polished briefly from one side only, to obtain a mirror smooth finish. Al wires were stitch bonded to this jet-polished substrate surface. Typical bonding parameters that ensured strong wire bonds were a force of 96 g, 0.92 watts power and a bonding time of 60 msec. These wire bonded specimens were immersed in an aqueous solution of NaOH to etch away the Al wire leaving a bond "print" as shown in Fig. 31. The specimens were then returned to the jet-polisher and using a clear plastic disc to avoid electropolishing the side with the bond prints, jet-polished until perforation. A good specimen was one in which the etched perforation went through a bond "print".

Transmission electron microscopy was done on a Hitachi H-600 operating at 100 kV. X-ray microanalysis on thermally induced microstructurally transformed samples after UWB, was done at

M.I.T using a VG HB5 dedicated STEM operating at 100 kV equipped with a Link windowless energy dispersive spectroscopy detector. Semi-quantitative analysis was conducted using the K α lines for Ni, Al and P, and the M lines for Au. Intensity data was converted to compositions using the Cliff-Lorimer equation (Cliff, Lorimer, 1975) with efficiency factors calculated for the HB5 STEM. It must be mentioned that the samples examined were often difficult to prepare because of differential ion milling rates of the different metals, which resulted in relatively thick cross-section samples. Although samples were still electron transparent, absorption corrections would have been necessary to obtain highly accurate quantitative analysis, but since sample thicknesses were generally not known, absorption corrections could not be done.

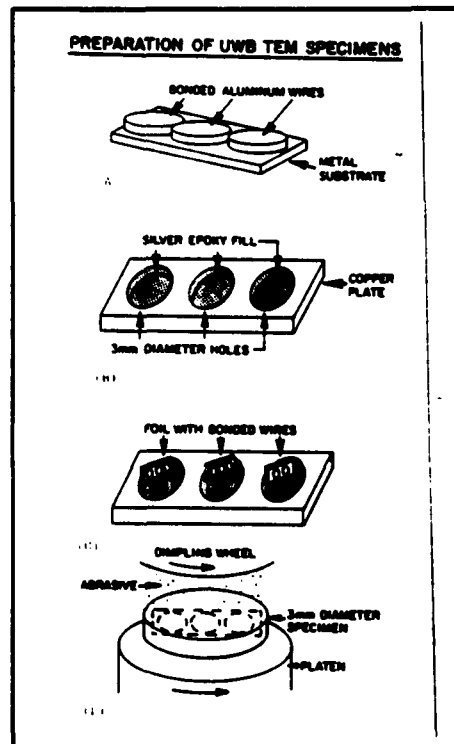


Figure 30 Cross-section view specimen preparation technique.

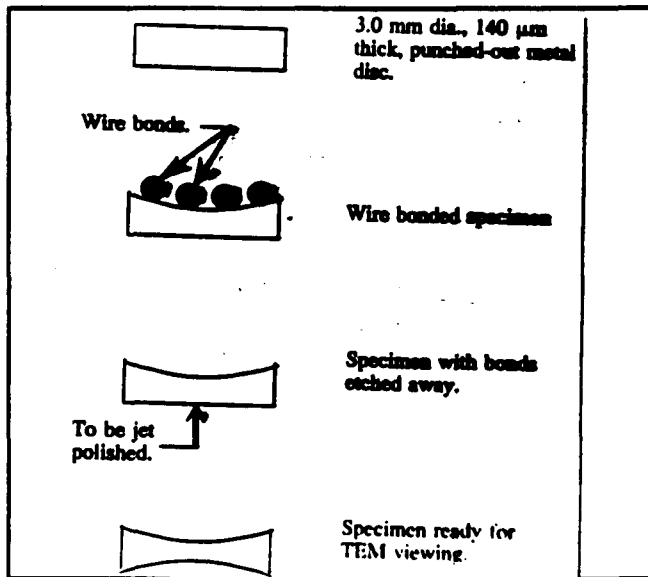


Figure 31 Plan-view specimen preparation technique.

CHAPTER IV

MICROSTRUCTURAL TRANSFORMATIONS DURING BONDING

Dislocation substructure evolution, also referred to as microstructural transformations in this thesis, were briefly described in Chapter II. It was said that these transformations through non-ultrasonic or ultrasonic fatigue cycling, were facilitated by the ease with which dislocations cross-slipped which in turn depended on the material's SFE. A further description of the cross slip process is therefore warranted since the phenomenon forms a basis for observations described in the present chapter.

Dislocation glide occurs when the slip plane contains both the Burgers vector and the line of dislocation, while cross slip occurs only when a dislocation is in the exact screw orientation. If the dislocation is extended, then the partials have to be constricted to form an unextended dislocation before it can cross slip. The constriction of the partials is made easier by thermal activation and hence the tendency to cross slip increases with increasing temperature. The constriction process is also more difficult the wider the separation of the partials, as in low SFE materials. The SFE

and the equilibrium separation distance, d , between the partials are related by the following equation (Meyers, Chawla, 1984):

$$\gamma = \frac{Gb_1b_2}{2\pi d} \left(\cos\theta_1 \cos\theta_2 + \frac{\sin\theta_1 \sin\theta_2}{(1-\nu)} \right)$$

where γ is the SFE per unit area, G is the shear modulus, b_1 and b_2 are the Burger's vector of the separated partials of the form $a/6 \langle 112 \rangle$ for a fcc metal, and θ is the angle of the Burger's vector with the dislocation line. Table 1 compares the SFE, d and recrystallization temperatures of the different metal substrates used in this study. When the SFE is high, and d is small, such as in the case of Al (250 mJ/m^2), cross slip is very easy and screw dislocations can arrange themselves into almost perfect sub-boundaries (Smallman, 1990). However, for a low SFE and large d material, such as stainless steel (23.3 mJ/m^2), the activation energy for the cross slip process is high. Nevertheless, it is said that cross slip can still occur in regions where high concentration of stress exists, as for example when dislocations pile up against some obstacle, where the width of the extended dislocation may be reduced below d .

Some other terms important to observations described in this and the subsequent chapters are concerned with the removal of cold worked conditions in a metal, namely recovery and recrystallization. Recovery is the process of

rearrangement and annihilation of dislocations causing reduction in lattice strain energy and formation of cell walls. Recrystallization, on the other hand, has to do with more significant changes.

Table 1 : Bonding Substrate Properties.

Bonding Substrates	SFE (mJ/m ²)	d (nm)	Recrytal. Temp. (°C)
Pure Al	250 ²	1.0 ³	194
Pure Ni	200 ²	2.9 ³	590
Pure Cu	90 ²	3.2 ³	405
Stainless (304)	23.3 ³	37 ⁴	775

The deformed lattice is completely replaced by a new unstrained one in which new stress-free grains grow from nuclei formed in the deformed matrix. The orientation of the new grains differ considerably from that of the crystals they consume, so that the growth process can be regarded as incoherent, that is, it takes place by the advance of high-

²Hertzberg, 1989.

³Meyers, Chawla, 1984.

⁴Estimated from calculations.

angle boundaries separating the new crystals from the strained matrix. The temperature above which recrystallization occurs can be approximated to $0.5T_m$ (T_m is the melting temperature in °K) as shown in Table 1 for the different metal substrates examined. It is also known that the rate of recrystallization depends on several important factors, namely: 1) the amount of prior deformation, that is, the greater the degree of cold work the lower the recrystallization temperature and the smaller the recrystallized grain size; 2) the temperature of the anneal, that is, as the temperature is lowered the time to attain a constant grain size increases exponentially; and 3) the purity of the sample, for example zone-refined Al recrystallizes below room temperature whereas commercial purity Al must be heated several hundred degrees.

4.1 Wire Transformations - The observations in this section have been taken from our recent publication (Krzanowski, Murdeshwar, 1990).

Substrates with different types of hardness ranging from pure annealed Al to 2024 alloy were used in this study. Figs. 32-34 show typical grain structures for 3 mil bonding wires bonded to a pure Al substrate with a high bonding time of 90 msec, typical bonding parameters of 85 gf, 60 msec, and 0.6 W, and to an as-received Al 2024 alloy substrate with bonding parameters of 100 gf, 60 msec and 0.7 W. It can be seen that all grains in these figures exhibit a very low dislocation

density. In some cases low angle grain boundaries normal to the elongated directions of the grains provide evidence for dislocation recovery. Similar grain structures were observed for all wire bonds, the only exception being specimens bonded with a high force of 130 gf which showed a slightly higher dislocation density. The absence of high dislocation density in the bonded wire microstructures are surprising since the wires deform to a thickness of about one-half of their original diameters. Exceptions to this were noted in two types of regions in the wire : 1) near interfacial contamination layers, and 2) near the tail section of the wire. An example of the latter is shown in Fig. 35, although even here it appears that some recovery occurred. It is also expected that a high dislocation density would be present on the edges of the bonded wire, since much of the surface contamination is pushed into the interface near the bond edge during bonding (Harman, Leedy, 1972).

The microstructure of the bonded wire was further examined in the specimen bonded with a large bonding time. One particularly interesting feature was the presence of dislocation loops, such as those shown in Fig. 36. These loops typically measured 30-50 nm in diameter and were not present in the wire before bonding. It was noted that such loops happened to be absent from regions close to grain boundaries indicating that the vacancies had diffused to the grain boundary. Another feature frequently observed were low angle

grain boundaries, where the plane of the boundary was normal to the direction of grain elongation. Fig. 37 shows a bright-field/weak beam image pair of low angle grain boundaries. There are also dislocation loops near these boundaries as indicated by arrows. The presence of these features and their implications on the wire deformation is discussed below.

Studies of the deformed wire showed an absence of a cold worked structure, as suggested by Joshi (1971). Since the wire undergoes significant macroscopic deformation during bonding, a competing dynamic annealing process must occur at the same time as the deformation process. Several observations in the microstructure support this conclusion. First, there is a very low dislocation density in the grains of the deformed wire, and these grains are often equiaxed. In addition, the dislocation loops observed in the wire appear to be formed by emission of vacancies from jogs, as observed in Fig. 38 for an Al substrate. The dislocations also appear to form low angle grain boundaries which lie in planes parallel to the direction of the applied force. The presence of low angle grain boundaries is consistent with microstructure expected from a deformed and subsequently annealed metal. The presence of dislocation loops, normally associated with Al rapidly quenched from annealing temperatures, is an indication that excess vacancies are created by dislocation motion, such as jog drag. During normal annealing processes these vacancies would have time to diffuse to grain boundary sinks rather than

form loops. As shown in Fig. 36 in ultrasonically bonded Al, vacancy diffusion and elimination of dislocation loops only occurs near grain boundaries leaving significant number of dislocation loops in the grains. The fact that the time of bonding is typically 50-90 msec, that no significant macroscopic heating during bonding has ever been measured (Joshi, 1971), that dislocation loops are not fully annealed out of the specimen, and that low angle grain boundaries appear along with low dislocation density elsewhere, all support the conclusion of dynamic annealing.

The absence of dislocation loops from zones near grain boundaries in Fig. 36 allow for a kinetic consideration of the dynamic annealing process. The width of this zone is approximately 0.15 to 0.25 μm . The temperature at which this process would take place if it occurred during heating of the sample can be calculated using the equation,

$$x^2 = D_v t,$$

where x is the zone width, D_v is the diffusivity of the vacancies and t is the bonding time.

Using the self diffusion coefficient of Al, in which D_0 is 1.7 cm^2/sec and the activation energy Q is 34 KCal/ mole (Brandes, 1983), the diffusivity of vacancies can be calculated from,

$$D_v = D_{Al} / X_v,$$

where D_{Al} is the self-diffusivity of Al and X_v is the fraction of vacancies. Using an activation energy of 0.8 eV/atom for

the formation of a vacancy, at room temperature the vacancy fraction is 2.6×10^{-13} . However, the loops also contribute vacancies as they dissolve. To calculate this contribution, the loop area/volume is calculated. From Fig. 36 the number of loops/projected area is calculated to be 6.7×10^{-7} loops/ \AA^2 . The sample thickness is not known, but is estimated to be between 2500 and 5000 \AA . This gives 1.3×10^{-10} to 2.6×10^{-10} loops/ \AA^3 . The loops are estimated to be 375 \AA in diameter. Considering the volume occupied by a vacancy in Al, a vacancy fraction of 3.5×10^{-5} to 7×10^{-5} is calculated. Using the above relation for D_v , the values listed for x and times of 0.09 to 0.18 sec (the time was doubled in the second case to allow for heating and cooling), a range of temperatures can be calculated. The values obtained are 227°C to 271°C with an average of 250°C. It should be emphasized that this temperature is that which would be necessary if the process of vacancy depletion near the grain boundary were to occur by a macroscopic, uniform heating of the bonded wire. In Section 2.3.2, the energy of ultrasonic vibration has been suggested to be dissipated by microstructural defects such as dislocations which provide localized heating. It is expected that the temperature during bonding would not be uniform but would vary on the microscopic level. In this case, it would be necessary to obtain an average temperature in these high defect areas of close to 250°C for 90-180 msec, or higher temperatures for shorter time periods. If room temperature is

substituted in the above analysis then to achieve the stated diffusion distance would take 138 years. In the same vein, the thermocouple measured temperature of 80°C reported by Joshi was the average temperature achieved uniformly throughout the sample. It should be noted that the above analysis neglects diffusion distance from epoxy curing temperatures and times (90°C for 90 minutes) which is approximately 0.01 μm compared to the measured width of the dislocation loop free zone of 0.15-0.25 μm .

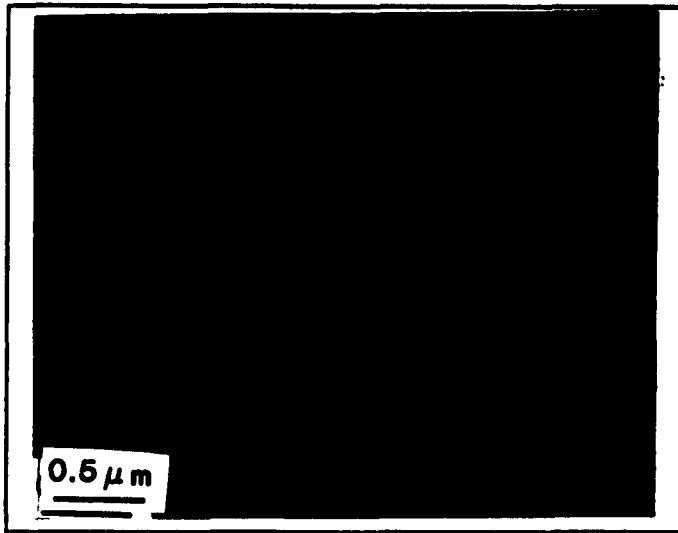


Figure 32 Microstructure of bonded wires to pure Al substrate with a high bonding time of 90 msec.

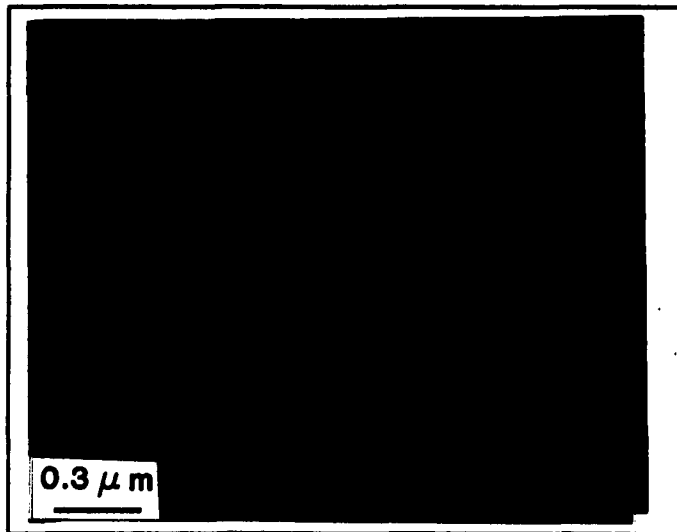


Figure 33 Microstructure of bonded wires to pure Al substrate with typical bonding parameters of 85 gf, 60 msec, and 0.6 W.

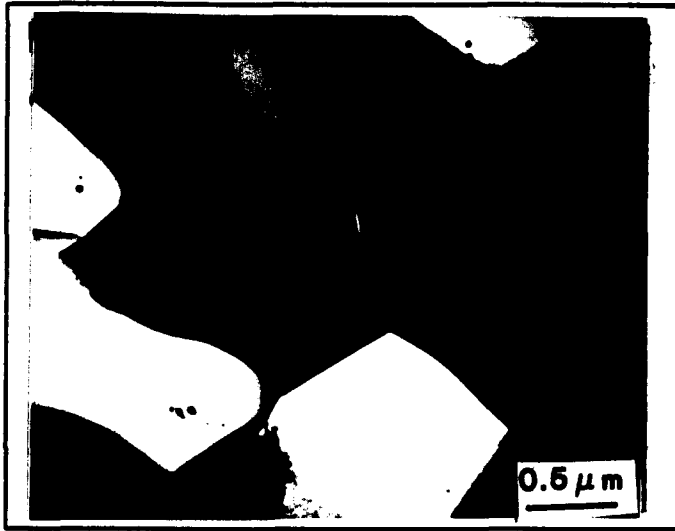


Figure 34 Microstructure of bonded wires to an as-received Al 2024 alloy with bonding parameters of 100 gf, 60 msec, and 0.7 W.

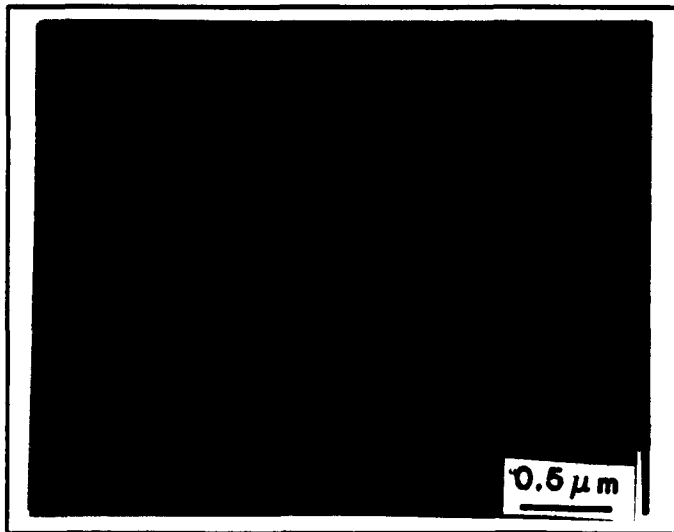


Figure 35 The grain structure near the tail section of a bonded wire. The black spots are contaminants from the silver epoxy.



Figure 36 Dislocation loops in the wire bonded with a high bonding time of 90 msec.

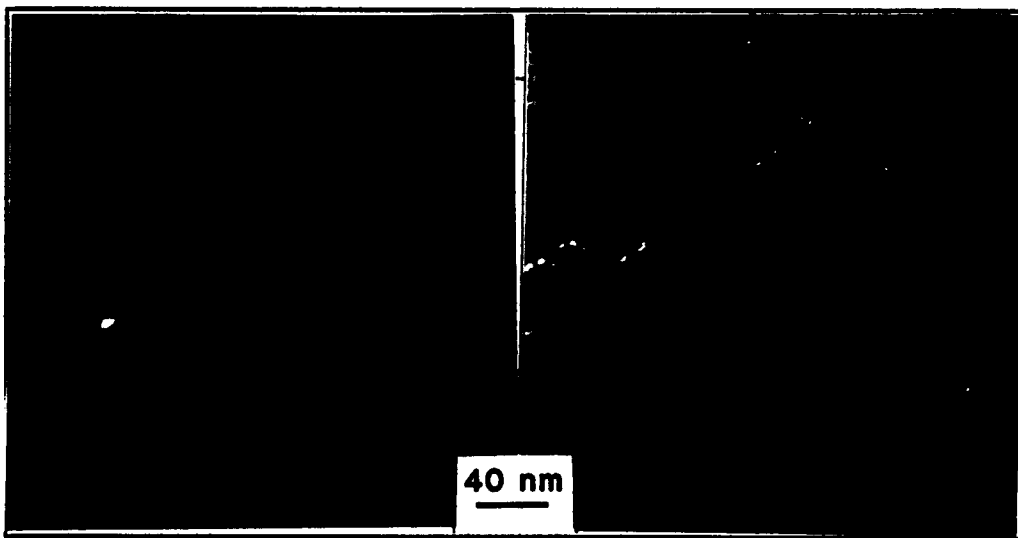


Figure 37 Low angle grain boundaries in the bonded wire in a specimen bonded with a high bonding time of 90 msec - weak beam (left) and bright-field (right) images.

4.2 Substrate Transformations - Substrates in this section have been examined in either the cold-worked or annealed states in which the dislocation density is expected to be in the order of $10^{12}/\text{cm}^2$ and $10^4/\text{cm}^2$ respectively. The microstructures of these states will not be presented here since they are well documented. However, transformations of the microstructure from the initial to the final state during bonding will be presented and discussed.

Examination of microstructure transformation of the different metal substrates were done on plan view and/or cross section view specimens. To facilitate discussion of plan view specimens some frequently used terms are to be defined. In Fig. 39 a bond is made after which the wire is etched or pulled such that a clean bond break occurs. Three distinct regions are apparent. The region outside the bond showing no change is called the outer zone (OZ), the region at the bond perimeter and just inside it where a dark coloration is formed is called the peripheral zone (PZ), while the central region of the bond is called the bond zone (BZ). It should be noted that the high magnifications often associated with TEM examination do not allow for all three regions to be viewed simultaneously and only parts of the bonding area can be examined at any given time.

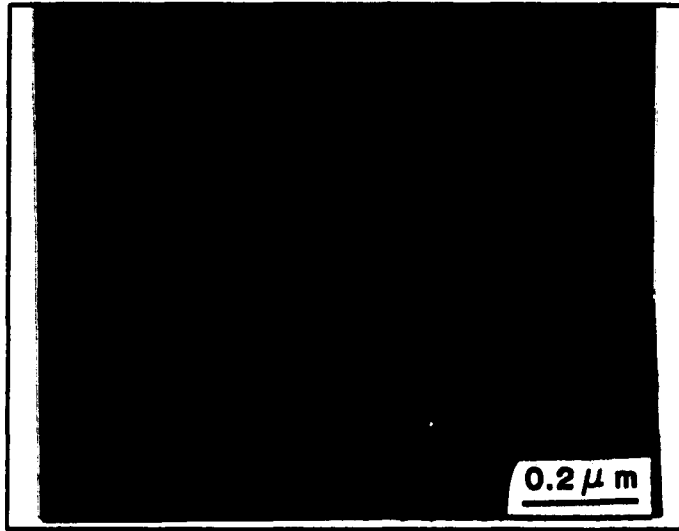


Figure 38 Microstructure of the substrate near a wire bond showing a dislocation loop forming behind a jog in a dislocation.

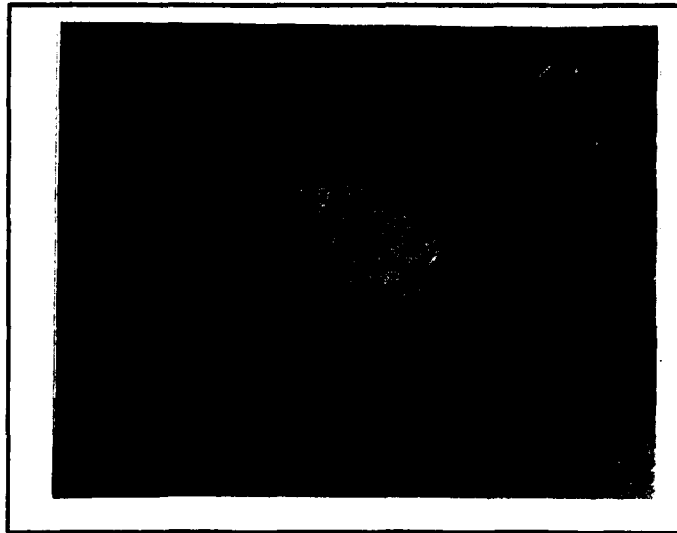


Figure 39 An etched wire bond showing three different regions of plan view specimens.

4.2.1 Transformations in Aluminum - Cross-section specimens prepared through jet-polishing were examined. The 6061 Al alloy substrates were solutionized prior to bonding by heat treating at 530°C for 4 hours before quenching in brine. An example of the resulting microstructure near the wire bond is shown in Fig. 40. Here the grains appear equiaxed with low angle boundaries, dislocation loops and low dislocation density. Fig. 38 shows hairpin-shaped dislocations with loops being pinched off. As was stated above, this feature suggests the formation of jogs which emit vacancies as the jog is dragged along during deformation. The vacancies can form loops if the diffusion distance to the grain boundary sinks is too long or the bonding time too short for the vacancies to diffuse to grain boundaries.

The microstructure away from the bond interface in Fig. 41 showed a dislocation density higher by about an order of magnitude than that of the foil before bonding (Fig. 42). This would indicate that some of the dislocations are generated during bonding or sample preparation with no evidence of dynamic annealing occurring away from the bond interface. However, when Fig. 40 and the microstructure before bonding (Fig. 42) were compared, it was concluded that dynamic recrystallization occurred in the substrate near the wire. It should be noted that despite 6061 alloy being an age-hardenable alloy, there was no precipitate formation. Considering that at 232°C the 6061 alloy requires 360 sec to

reach peak hardness, the absence of precipitates is consistent with the kinetic analysis for expected bonding temperatures, described in Section 4.1.

Fig. 43 shows a bond interface of a pure annealed Al substrate bonded at a high time of 90 msec. Here, the interface appears to be randomly oriented grains joined together, similar to a grain boundary in a polycrystalline metal. In fact, while observing the bond interface it was often difficult to distinguish between the interface and the grain boundaries in the wire or substrate. The presence of contamination along the bond in other locations made it possible to find the bond interface, such as in Fig. 44 which was presented in an earlier work (Krzanowski, 1989). The substrate was a peak aged 2024 alloy with an as-received surface bonded with parameters of 100 gf, 60 msec and 0.7 W. An x-ray microanalysis reported that the contaminated region consisted of elements such as S, Cl, and possibly metal oxides. It was expected that the region in Fig. 43 would exhibit good adhesion, while the contaminated region in Fig. 44 would exhibit poor adhesion. An additional effect of contamination in the specimen bonded with a high time is shown in Fig. 45, where dislocations are observed to be emitted from the contaminated region. In general, the relatively clean interfaces coincided with the absence of dislocations near the bond interface. Ar ion plasma cleaned samples appeared to have fewer contaminated regions of the type shown in Fig. 44,

although this was difficult to quantify due to the small portion of the total bond area observed in the TEM.

A comparison of the microstructures in Fig. 40 and 43 revealed an interesting feature. The grain size in the 6061 alloy was much smaller than that of pure Al which seemed to suggest that these were different degrees of dynamic recovery. Considering the initial microstructure as part of this comparison, the substrate in Fig. 43 started as annealed pure Al with large grains relatively free of dislocations, while the 6061 substrate in Fig. 42 has a higher dislocation density of $10^{12}/\text{cm}^2$. This high dislocation density will result in more dissipation of ultrasonic energy. It therefore appears that the initial defect density in the substrate will have a significant impact on the extent of dynamic annealing which occurs during bonding.

The initial states, cold worked or annealed, of the substrate prior to UWB and their effect on the ensuing microstructure transformation is further discussed in the following sections below.



Figure 40 Microstructure of the 6061 substrate near a bonded wire. The bond interface is shown across the top.

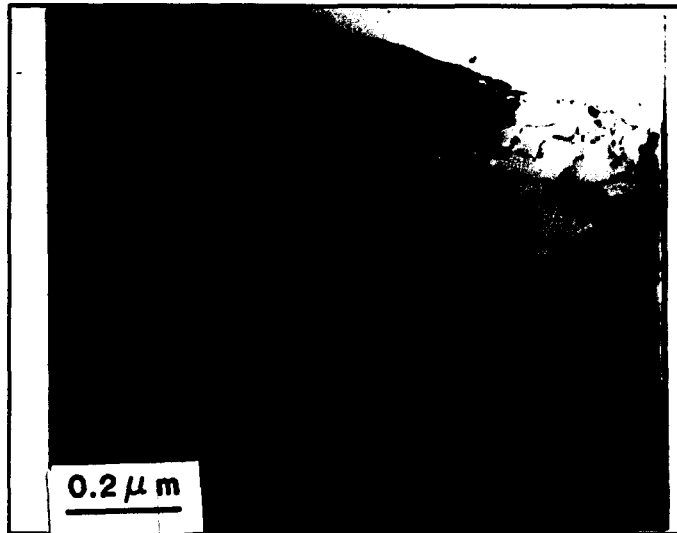


Figure 41 Microstructure of the 6061 substrate away from the wire bond area.

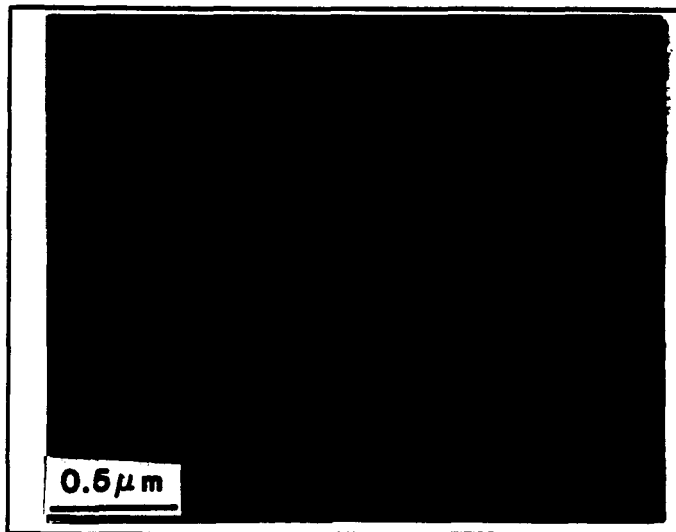


Figure 42 The condition of the 6061 substrate prior to bonding.

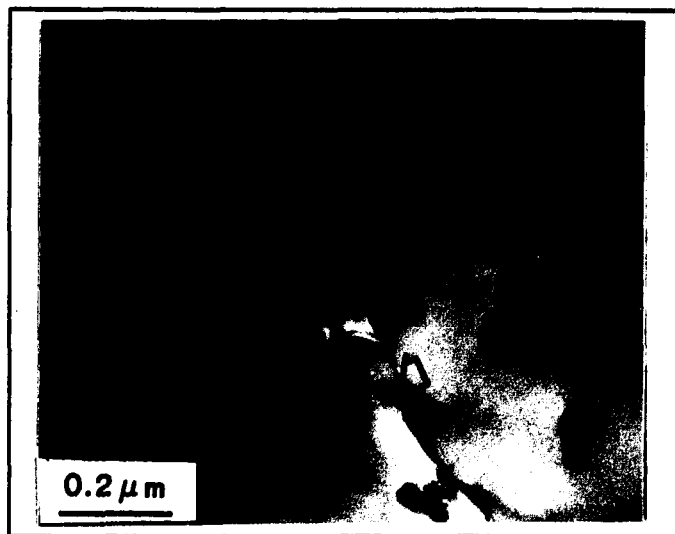


Figure 43 Image of the bond interface in the pure Al substrate bonded with high bonding time. The bond interface is indicated by arrows.

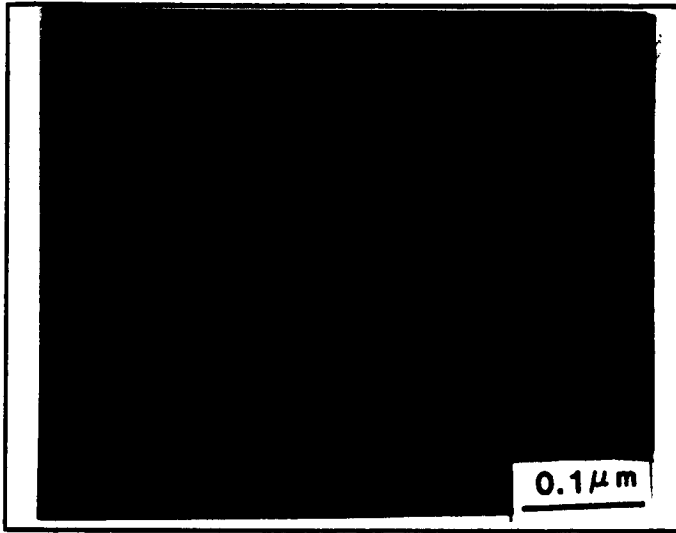


Figure 44 Image of the bond interface in a contaminated region (Krzanowski, 1989).

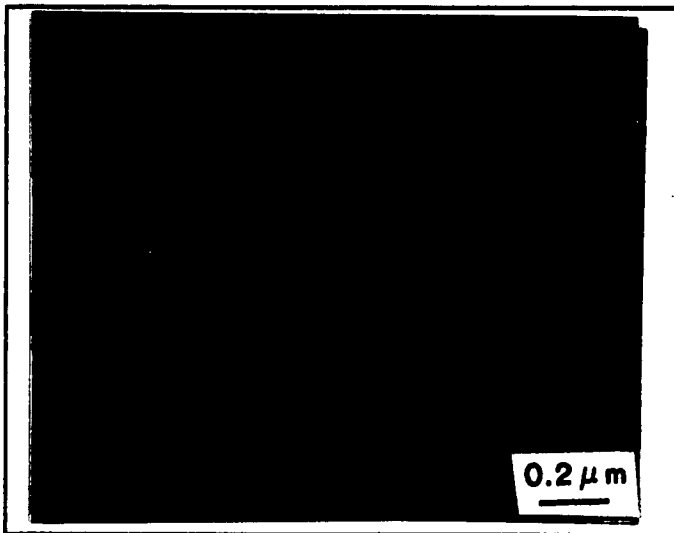


Figure 45 Image of the bond interface with dislocations emitted from a contaminated region (indicated by arrows).

4.2.2 Transformations in Nickel - In this study, both pure Ni and a commercially manufactured Ni200 substrates were examined. However, the microstructures shown here are of wire bonds to the latter.

The Nickel substrate plan view specimens examined were either in the cold worked or annealed states. The 42% cold-worked state was brought about by rolling, while annealing consisted of heating the as-received foil at 760°C for 2 hours. A H-Ar gas environment was used to minimize oxidation effects. Cross section specimens were also examined to corroborate observations.

Typical microstructures observed in the BZ of plan view annealed specimens are shown in Fig. 46 and 47. Distinct square shaped dislocation cells are seen in the former, while in the latter dislocation veins can be seen possibly the result of a transition to cell formation. The distinct dislocation networks gradually fade to less distinct networks (Fig. 48) upon moving towards the PZ which could be either/or both of the following explanations: 1) a result of the difference in dislocation interaction intensity due to grain orientation, as reported in section 2.3.1 (Jin, Winter, 1984); 2) an effect of the variation in stress in the bonded region. The second explanation gives credence to the fact that during bonding, the maximum stress causing flattening of the wire is directed along the wire axis under the tool. The stress would therefore decrease away from the wire axis.

Commonly occurring microstructural features in the BZ such as dislocation dipoles (D), loops (L) (Fig. 49), and dislocation bundles leading to dislocation rich (A) and poor (B) regions are observed in Fig. 48. This type of structure is typically expected of dislocation veins which consist of a loose agglomeration of dislocation loops and dipoles. Evidence for the effect of ultrasound on the microstructure is provided by dislocations emanating from the incoherent steps of the annealing twin (T) in this micrograph. This is consistent with previous reports on the effect of ultrasound on the microstructure (Shea, Rao, 1982).

A dramatic change in the microstructure from the regular network of dislocation cells in the BZ to the intense dislocation activity at the PZ is seen in Fig. 50. This activity is characterized by dark regions of intense but inhomogeneous deformation. A selected area diffraction pattern analysis of this area (Fig. 51a) indicated traces of Al, which is unusual since the Al wire is etched away during sample preparation. In Fig. 51a the obtained diffraction pattern is compared with that of an Al diffraction ring pattern. It is possible that this could be a result of mechanical mixing between the wire and substrate. Outside the bond area, in the OZ (Fig. 51b), an annealed grain structure not affected by the cellular dislocation networks of the BZ or the inhomogeneous deformation of the PZ is observed.

Cross section annealed specimens (Fig. 52) revealed

similar although not as distinct cells in the BZ extending from the top, at the bond interface through the substrate thickness. It should, however, be pointed out that during the course of cross section specimen preparation the steady erosion of the material through polishing and the final ion milling treatment reduces the substrate thickness to less than 25 μm . No evidence of inhomogeneous deformation that characterized the PZ in the plan view specimens was observed in these specimens suggesting that this feature of the UWB is of maximum intensity at the surface and is also restricted to the surface. Ion milling also causes radiation damage, the extent of which depends on the material ion etching rate. TEM image resolution of a specimen prepared using this technique may therefore be effected.

Plan view cold worked and bonded specimens in Fig. 53 showed subgrains with lower dislocation densities than a typical cold worked Ni microstructure prior to bonding. The grain structure here showed a faint hint of recovery. The difference in microstructures between cold worked and annealed states during bonding, is worth further discussion.

The total dislocation stored energy (U_T) state can be calculated as follows,

$$U_T = U_{\text{Core}} + U_{\text{Strain Energy}}$$

U_{Core} is an approximation of the strain energy at the dislocation core where the severe lattice distortion cannot be explained by linear elasticity theory. $U_{\text{Strain Energy}}$ is the strain

energy at a distance $5b$ (Meyers, Chawla, 1984) from the core beyond which the theory is better applied.

$$U_T = \frac{Gb^2}{10} + \frac{Gb^2}{4\pi(1-\nu)} (1-\nu \cos^2\theta) \ln \frac{\rho^{-1/2}}{5b}$$

where, G is the shear modulus, b the Burger's vector, ρ is the dislocation density, ν is the poisson's ratio and θ is the angle between b and the dislocation line. For an edge dislocation, that is, when $\theta=90^\circ$, Table 2 gives the total dislocation stored energies for annealed and cold worked metal

Table 2 : Total dislocation strain energies.

Metal Substrate	b (nm)	G (GPa)	Annealed U_T (J/Mol)	Cold Worked U_T (J/Mol)
Al	0.286	26.1	30.40e-07	706.17
Cu	0.255	48.3	32.19e-07	77.07
Au	0.288	27.0	32.72e-07	758.44
Ni	0.249	76.0	39.58e-07	107.98

substrates. The difference between the dislocation energies of the annealed and cold worked states are expected. However, a considerable difference is seen when these energies are compared with the recrystallization activation energies, Q , in

Table 5 (Section 5.3). For example, the dislocation energy of Al in the annealed and cold worked states are 30.40×10^{-7} J/mol and 706.17 J/mol, respectively, while the recrystallization activation energy is 142000 J/mol. This implies that the total dislocation energies are too small to be of any significance in UWB microstructure transformations while the presence of higher metal defects associated with a cold worked state implies that more ultrasonic energy is dissipated at these defects. The actual transformation, possibly brought about through diffusion of atoms is discussed further in Chapter V.

Examination of pure annealed Ni substrates showed a similar microstructure to that of Ni200 described here.

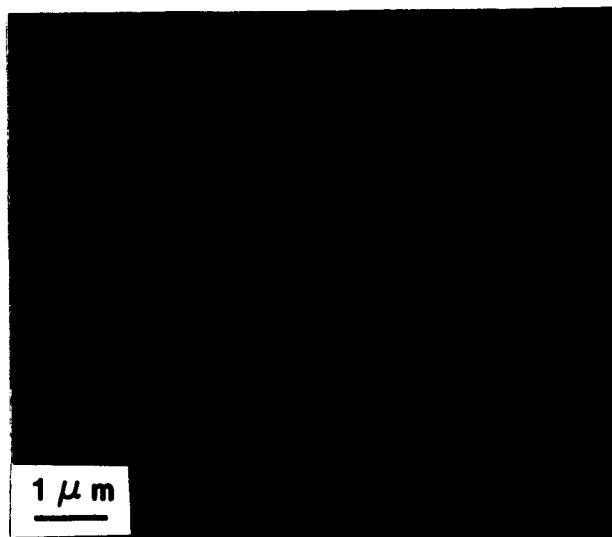


Figure 46 Distinct dislocation cells observed in the BZ of an annealed Ni substrate. ($z = [113]$).

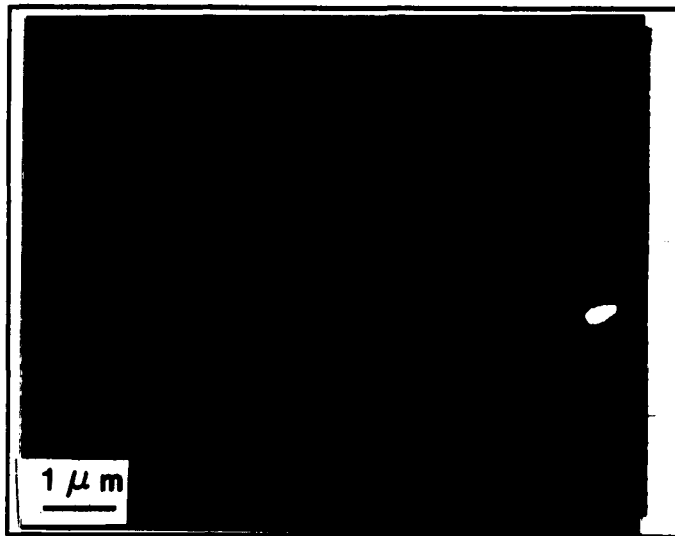


Figure 47 A transition from dislocation cells to veins in the BZ of an annealed Ni substrate.



Figure 48 Dislocation veins in the BZ of an annealed Ni substrate.

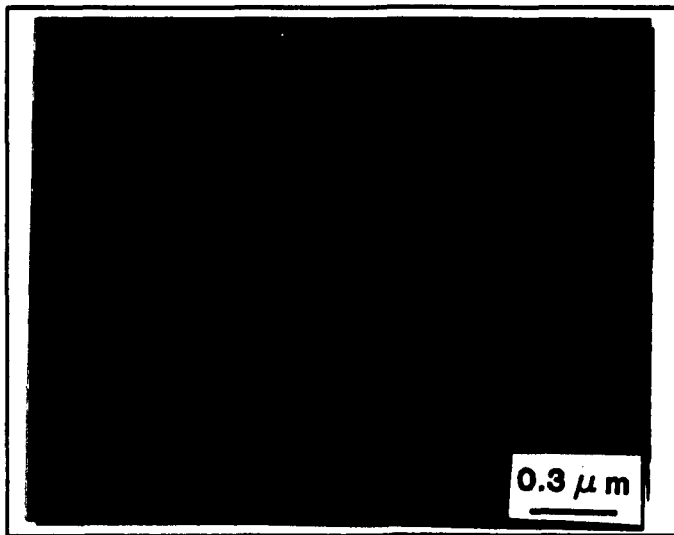


Figure 49 Magnified image of the dislocation veins in the BZ.

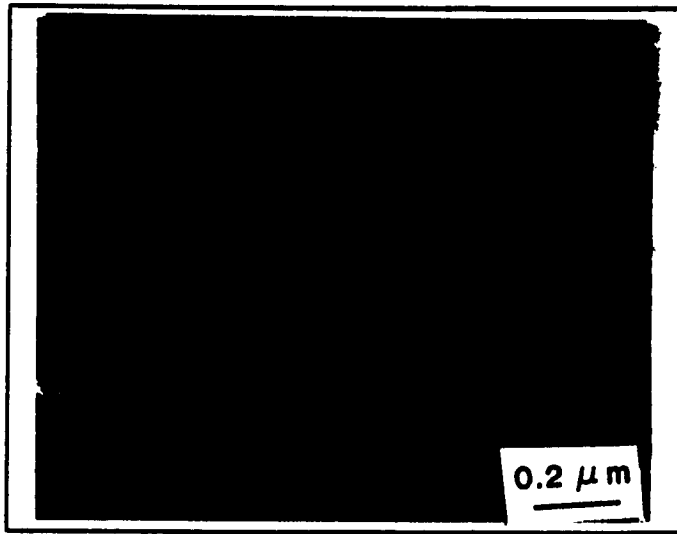


Figure 50 Intense dislocation inhomogeneous deformation at the PZ for an annealed Ni substrate. ($z=[011]$).

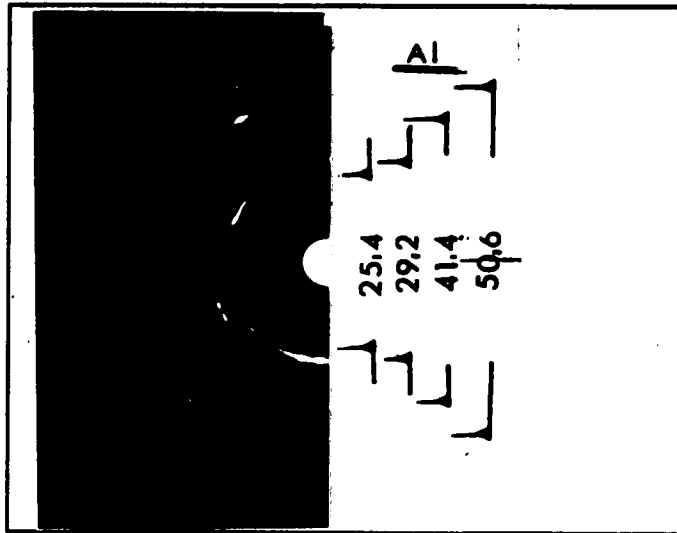


Figure 51a Selected area diffraction pattern of the PZ compared to Al.

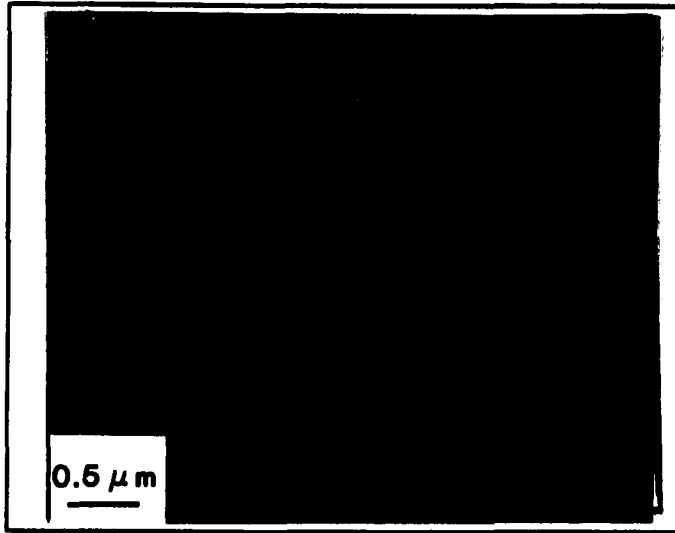


Figure 51b Typical annealed grain structure in the OZ.

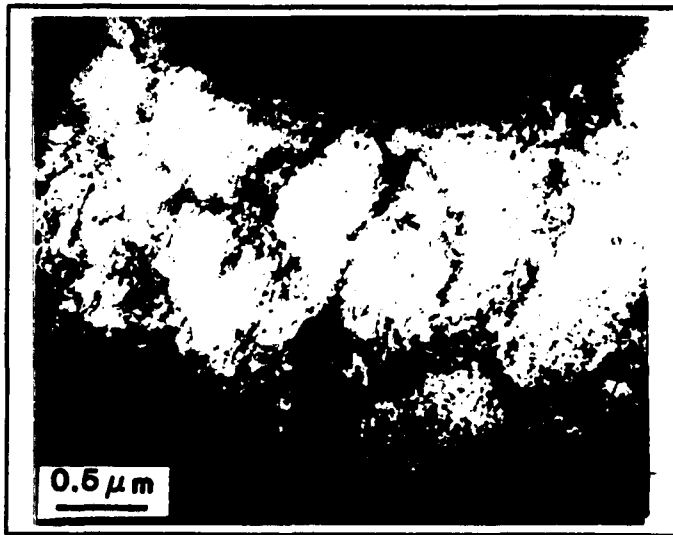


Figure 52 Cross section view Ni substrate showing dislocation cells.



Figure 53 Dislocation cells in the BZ of a cold worked Ni substrate.

4.2.3 Transformations in Copper - Copper substrate plan view specimens examined were either in the cold worked or annealed states. The 53% cold worked state was brought about by rolling, while annealing consisted of heating either at 260°C (Pure Cu) or at 372°C (ETP Cu) for 1 hour depending upon the purity of the metal.

Microstructural changes in annealed pure Cu substrates from the BZ to the OZ are shown in Fig. 54-56. The dislocation patterns in the BZ shown in Fig. 54 and 55 are very different from that of either Al or Ni substrates presented in the previous sections. The small rectangular subgrain structure here shows a considerable increase in dislocation activity and appears partially recrystallized. At this point, it is difficult to distinguish between a recovered and a recrystallized microstructure. The difference in contrast between subgrains in this micrograph is indicative of misorientation that characterizes recrystallization, however, the observed structure is most likely to be partial recovery. For recrystallization to occur, sufficient thermal energy needs to be supplied thereby transforming the entire microstructure. Observations in this study indicate variation in the size of transformed cells and subgrains which is typically expected in structures showing different degrees of recovery. The subgrains at the center of the BZ in Fig. 54 are elongated with sharp thin walls and considerable dislocation activity within. Annealing twins (T) can also be seen in this

microstructure. As the PZ is approached in Fig. 55, this rectangular small grain structure of the BZ, transforms into somewhat rounded equiaxed grains. An explanation similar to that in the previous subsection could account for the change in cell structures observed here, namely, the difference in the intensity of dislocation interactions and/or the variation in bonding stress. However, the mechanism that facilitates change in structure from rectangular to round equiaxed grains may be the result of compatibility stresses produced at the grain boundaries leading to enhanced multiple slip as suggested by Roven and Nes (1991). A similar hypothesis was used in Section 2.3.1 to explain cell formation in non-ultrasonic fatigue microstructures. The dramatic change in the microstructure at the PZ is clearly visible in Fig. 56 with the dark areas demarcating the bonded region from the unchanged OZ.

Microstructures at the BZ of a cold worked Cu substrate in Figs. 57 and 58 are also quite different from that of the cold worked Ni substrates. Here a dynamically annealed structure is seen with thick walled, completely recovered low angle grain boundaries having dislocation-poor interiors. All the dislocations typical of the cold worked structure prior to bonding seem to be dispersed to the cell walls. The microstructure of the peripheral and outer zones were similar to the observations described above for these zones, with inhomogeneous deformation characterizing the former and the

unchanged structure characterizing the latter. Subsequent observations on annealed ETP Cu (99.9%Cu, 0.04% O) substrates did not reveal any significant difference from that of the pure Cu substrates. The total dislocation strain energies for annealed and cold worked states are 32.19×10^{-7} J/mol and 77.07 J/mol (Table 2) respectively. When compared to the much larger recrystallization activation energy of 2×10^5 J/mol, the ineffectiveness of the total dislocation energy in bringing about these observed microstructural transformations is clearly evident.

Substrates of pure Cu and its alloys, namely ambralloy and brass were also examined. These substrates were heat treated to obtain grains of two different average size and the ensuing microstructure transformation on bonding was studied. Since that study was part of a further investigation into the effect of σ_{ys} on microstructural transformation which led to the development of a model, it has been described in the next chapter.

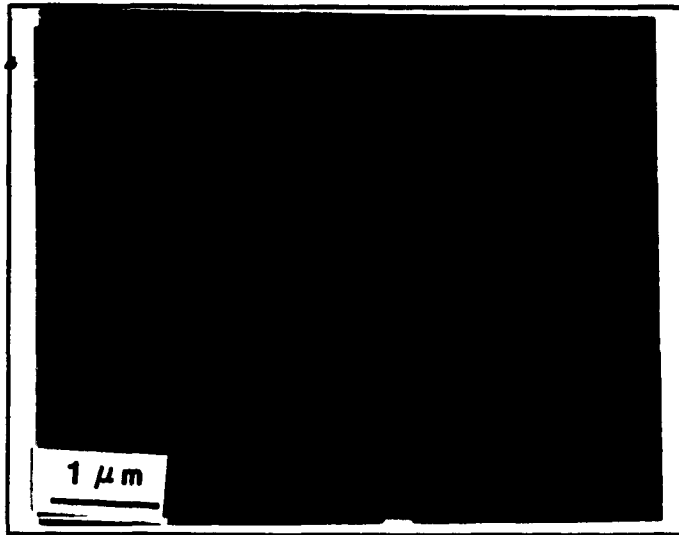


Figure 54 Recovered subgrains in the BZ of an annealed Cu substrate.



Figure 55 Round equiaxed grains in the BZ of an annealed Cu substrate.

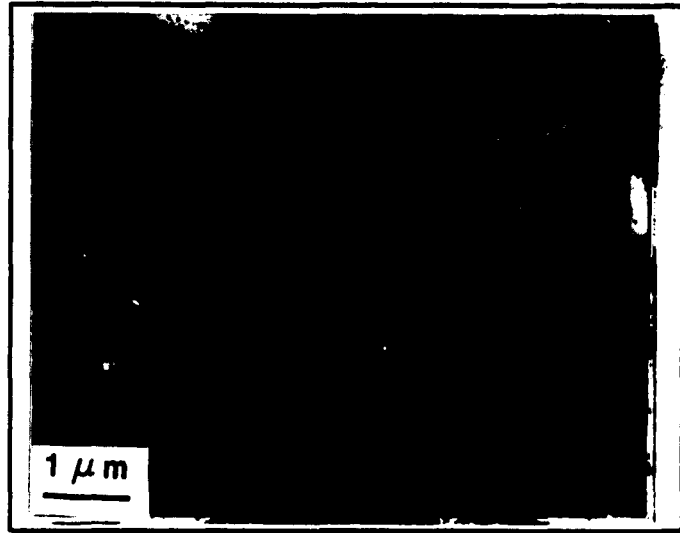


Figure 56 Intense dislocation inhomogeneous deformation at the PZ of an annealed Cu substrate.

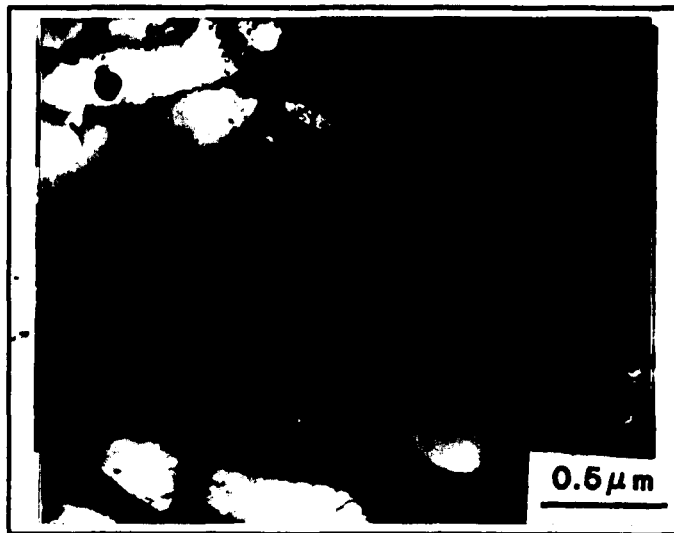


Figure 57 Low-angle thick walled completely recovered cells in the BZ of a cold worked Cu substrate.

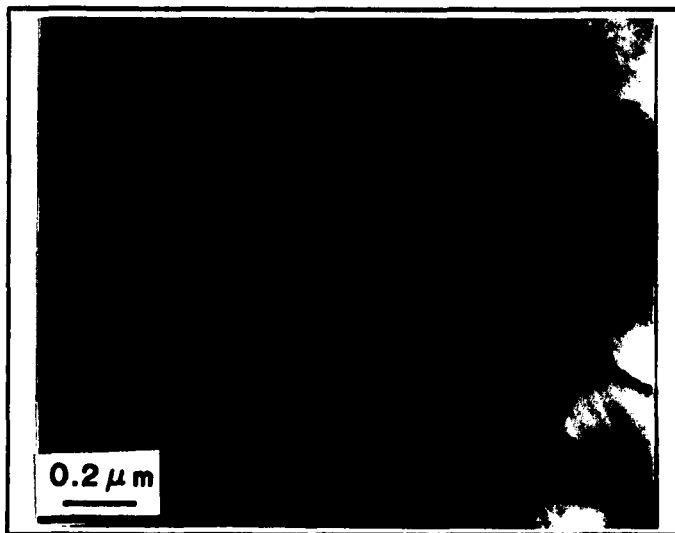


Figure 58 Low-angle thick walled completely recovered cells in the BZ of a cold worked Cu substrate.

Effect of the bonding time : As stated earlier, the bonding time associated with the UWB process is on the order of 20-90 msec. This short bonding time makes the process particularly attractive in typical automated manufacturing environments, where mass production emphasis is on speed and accuracy. However, from a research standpoint, the observations are restricted to a limited time span which adds to the complexity of the investigation. Fig. 59 shows the microstructure in the BZ at a relatively short bond time of 20 msec for an annealed Cu substrate. No cell formation was observed but incipient dislocation interaction is observed which is quite a contrast to the partially recovered structure (Fig. 53) obtained for a bonding time of 60 msec. When the bonding time is increased to the maximum of 95 msec the only change observed, is a more round, equiaxed cell structure, recovered to a greater degree (Fig. 60).

For annealed Ni substrates an increase in the bonding time to 95 msec results in a tendency to form dislocation cells as seen in Fig. 61, in addition to dislocation pileups as in Fig. 62. The curvature of these dislocation pileups indicates that the dislocations originated at the grain boundary and propagated away from it. Note the numerous types of dislocation interactions that take place, especially tangles and multi poles.

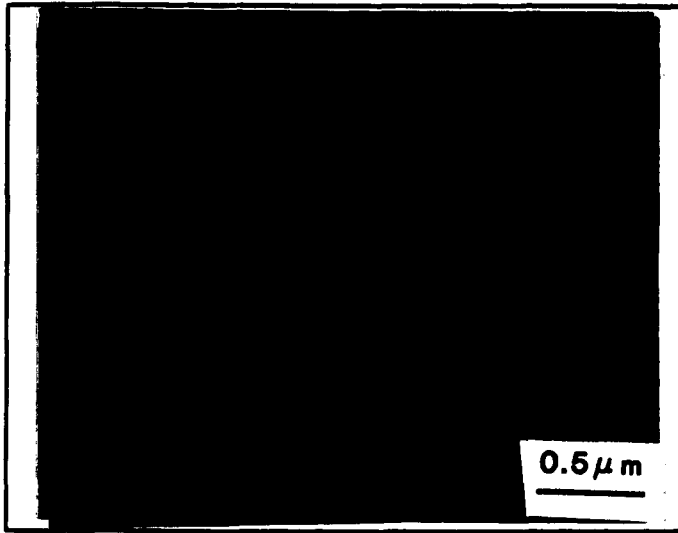


Figure 59 Microstructure of the BZ in an annealed Cu substrate at a bond time of 20 msec.

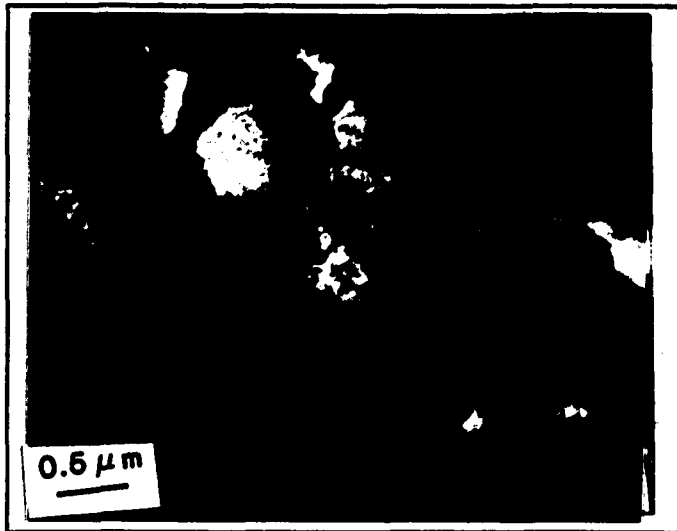


Figure 60 Microstructure of the BZ in an annealed Cu substrate at a bond time of 95 msec.



Figure 61 Microstructure of the BZ in an annealed Ni substrate showing dislocation cells. (t = 95 msec).

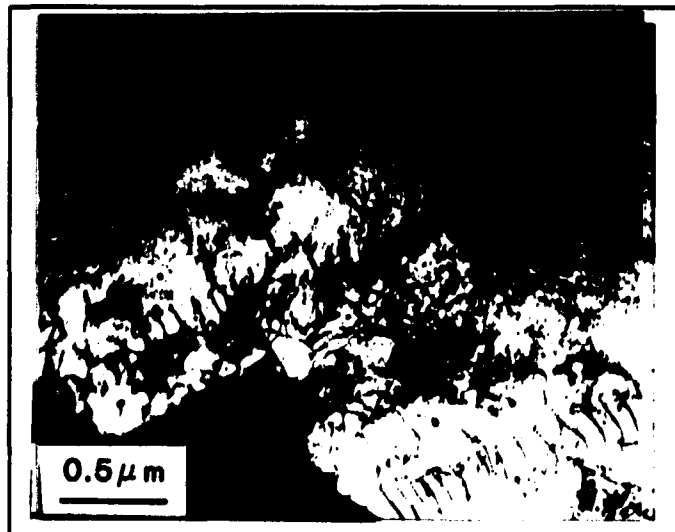


Figure 62 Microstructure of the BZ in an annealed Ni substrate showing dislocation pileups. (t = 95 msec).

4.2.4 Transformations in Stainless Steel - Annealed plan view specimens were examined. Annealing consisted of heat treating at 760°C for 2 hours. The microstructure observed in the BZ shown in Figs. 63 and 64 shows planar dislocation arrays. Typical dislocation configurations can be seen in the form of jogs, loops (L), dipoles (D), pileups (P) and nodes (N). As expected with low SFE materials, the presence of stacking fault segments can also be seen. The curvature of dislocations in the pileups of Fig. 63 indicates propagation away from the grain boundary. The planar microstructure here is a strong contrast to the cellular structure observed in Al, Ni or Cu. The PZ is as described earlier for the other substrates examined, while the OZ shows no change in structure.

The results from studies on microstructures obtained during non-ultrasonic cyclic testing were described in Section 2.3.1. It should be noted that in these studies, a particular substructure - dipoles, veins, walls or cells, was observed, each over a specific strain range⁵ only. For instance, Table 3 shows strain range and stress values for different metals as reported in the literature for which cell formation was observed during non-ultrasonic cyclic testing. In fact referring back to the schematic representation of the substructures formed during cyclic strain response of Cu in Fig. 15 (Section 2.3.1), it can be seen that these dislocation substructures form at a specific

⁵Strain range is twice the strain amplitude.

plastic strain range only. The strain range during bonding is an unknown quantity which remains constant for each substrate examined.

Table 3 : Literature data for cell formation during non-ultrasonic cyclic testing.

Metal	Appx. $\Delta\epsilon_p$ for cells	σ_p (MPa)	Reference
310 Stainless	8.8×10^{-3}	496	Jin, Zhong, Chen, 1990.
Comm. low alloy steel	4.1×10^{-3}	350	Roven, Nes, 1991.
OFHC Cu	1.0×10^{-3}	160	Figureoa, Bhat, De La Veaux, Murzenski, Laird, 1981.

From the microstructural observations described here, it is evident that the least transformed substrate is stainless steel, followed by Ni, Cu, and Al which shows maximum transformation. Using SFE arguments alone, the substrate with the maximum SFE would be expected to show a maximum transformation, in this case Al followed by Ni, Cu and stainless steel which was not observed. Although it appears that SFE influences microstructural transformation, the extent of its role is not known. It has also been shown that the total dislocation energies of a substrate prior to bonding are too small to be of any significance in these transformations.

Finally, if a microstructural analogy is permitted with

non-ultrasonic fatigue cycled specimens, then a reference should be made to the microstructural evolution along the CSS curve. The CSS curve described in Section 2.3.1 can be divided into three regions, each characterized by a difference in slope and substructure. Initially the substructure consists of dislocation loops in region I that develop into veins and PSBs (which some researchers attribute to the reason for the plateau of the CSS curve) in region II and finally to dislocation cells and subgrains in region III. The plastic strain range for which a plateau exists on this curve is very small.

In substrates examined in this study, similar microstructural features known to characterize region I such as dislocation loops, pile ups, etc., some features known to characterize region II such as dislocation veins, and cells and subgrains known to characterize region III, are seen. For instance, stainless steel shows region I microstructural features, Ni shows some region II features, Cu shows a transition from region II to region III features, while Al shows region III features. The important difference between non-ultrasonic cyclic studies and this study is that in the former, the same metal specimens are used while the strain range is varied. In the latter, using the same strain range (motion of the tool during bonding) the metal substrate specimens are changed, thus introducing different material properties. It is quite possible then that an analogy between

microstructures developed in non-ultrasonic cycling and UWB is valid provided material properties that cause the microstructural transformations can be properly considered.

Based on the observations described in this chapter a model has been developed in Chapter V which evaluates the extent of these microstructure transformations due to ultrasonic energy.



Figure 63 Microstructure of the BZ in an annealed stainless steel substrate.

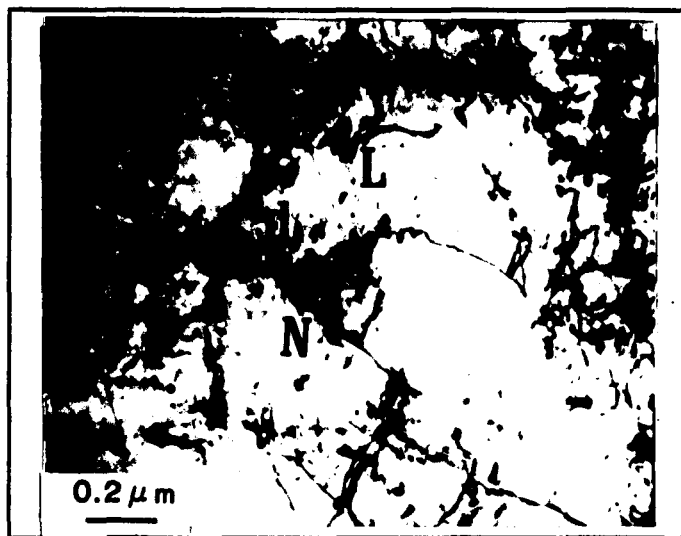


Figure 64 Microstructure of the BZ in an annealed stainless steel substrate.

CHAPTER V

THE EXTENT OF MICROSTRUCTURAL TRANSFORMATIONS DURING BONDING

In the preceding chapter microstructural transformations in Al, Ni, Cu and stainless steel were examined. It is clearly evident that ultrasonic irradiation during bonding caused the microstructural transformation. The extent of the roles that material properties such as SFE, σ_{ys} , diffusion processes and recrystallization temperature play in the transformation is not known. It appears that metal SFE indicates the type of microstructural transformation to be expected - planar or wavy, while the initial state of the metal - the degree of cold work or anneal, characterized by a specific dislocation density is expected to enable dissipation of ultrasonic energy. Therefore the extent of substrate microstructural transformation is thought to be a complex relationship between atomic diffusion and mobility depending on the dislocation density of the initial state of a substrate. This approach formed the motivation for developing a model to estimate the extent a substrate transformed during the UWB process.

First the concept of different metal substrate properties

affecting microstructural transformations will be further investigated by considering σ_{ys} in Cu and its alloys. Then diffusion processes in a substrate and its affect on substrate transformation will be studied by increasing the ambient temperature during bonding. Finally, microstructural observations in this and the preceding chapter will be discussed in the light of the developed model to gauge the effectiveness of the model.

5.1 σ_{ys} and its Influence on the UWB Process - The σ_{ys} of a metal can be varied by either alloying or changing the grain size.

This section describes microstructural observations of bonding to metal substrates where both alloying and grain size refinement are used to obtain different substrate σ_{ys} -values. The substrates Cu and its alloys, namely ambralloy⁶, and brass⁷, in addition to different σ_{ys} also have different SFE, with Cu (90 mJ/m²) having the largest and brass and ambralloy having extremely low SFE of <10 mJ/m² and <5 mJ/m², respectively. Two different average grain sizes of approximately 10 to 100 μ m, were obtained in the metals via various heat treatments.

The linear intercept method described in Meyers and Chawla (1984) was used to measure the average grain size d in

⁶Nominal composition Cu-8%Al.

⁷Nominal composition Cu70%-30%Zn.

the heat treated specimens. In this method, the mean intercept

$$l = 1/N_l = 2/S_v,$$

where N_l is the number of grain boundary intersections per unit length and S_v is the grain boundary area per unit volume. Assuming that the grains are spherical to a first approximation,

$$S_v = \left(\frac{1}{2}\right) \frac{4\pi r^2}{\left(\frac{4}{3}\right)\pi r^3} = \frac{3}{2r} = \frac{3}{d}.$$

The factor 1/2 is introduced because each surface is shared between two grains. Therefore,

$$d = (3/2) l.$$

In Cu an average grain size of 10.16 μm was counted in the as-received annealed metal, while an average grain size of 75.12 μm was obtained by 50% cold working and then annealing at 850°C for 40 minutes. In ambralloy, an average grain size of 29.89 μm was obtained by annealing for 40 minutes at 700°C, while an average grain size of 70.58 μm was obtained by 50% cold working and then annealing at 800°C for 40 minutes. A two step heat treatment was required for the ambralloy specimens in order to minimize second phase growth. This involved lowering the furnace temperature from either 700°C or 800°C to 500°C and maintaining the temperature for one hour before quenching the heat treated specimens in water. In brass, an average grain size of 38.39 μm was counted in the as-received annealed metal, while an average grain size of 104.51 μm was obtained by 50% cold working and annealing at 750°C for 40

minutes.

The σ_{ys} of metal specimens can also be theoretically calculated via the Hall-Petch relationship,

$$\sigma_{ys} = \sigma_0 + kd^{-1/2},$$

where σ_0 and k are experimental constants. σ_0 can be considered to be the overall resistance of the lattice to dislocation movement while k can be considered to be a "locking parameter" that measures the relative hardening contribution of grain boundaries.

Experimentally, σ_{ys} was determined using flat rectangular cross section tensile test specimens with a one inch gage length, quarter inch width and a thickness ranging from 150 μm to 400 μm and made from the heat treated metals. Due to the very thin cross section in some of the large grain specimens there were barely one or two grains contained within the specimen thickness. The specimens could therefore hardly be referred to as polycrystalline specimens, a requisite for any comparison of the experimental σ_{ys} to be made with the theoretically calculated value using the Hall-Petch relation. However, in most instances, the experimental σ_{ys} compared reasonably well with the theoretical value as shown in Table 4. Since the Hall-Petch constants were not available for ambralloy the theoretical σ_{ys} has not been included in the table.

Microstructurally, the BZ in plan view specimens of small and large grain Cu, brass and ambralloy specimens were studied

Table 4 : Experimental and theoretical σ_{ys}

S.#	Material/Heat Treatment	Grain μm	Expt. σ_{ys} MPa	H-P σ_{ys} MPa
12	Cu/As-received	10.16	61.51	60.01
13	Cu/50%CW/900°C 40m	75.12	38.93	38.19
22	Brass/As-received	38.39	131.11	95.14
23	Brass/50%CW/750°C 40m	104.51	60.26	75.43
32	A.Alloy/700°C 40m/ 500°C 1h/Quenched	29.89	128.24	-
33	A.Alloy/800°C 40m/ 500°C 1h/Quenched	70.58	70.94	-

in the TEM. Fig. 65 is the transformed microstructure of a small grain Cu specimen showing cell formation and some features similar to those described in Section 4.2.3. The entire grain in this figure consists of well formed rounded cells. The difference in contrast between cells is indicative of recrystallization although the observed thick cell walls would be typical of a recovered structure. The cells here appear to be similar to those in Fig. 55. It is quite conceivable that due to the small grain size, greater compatibility stresses are developed at the grain boundaries leading to enhanced multiple slip. A similar effect described by Roven and Nes (1991) in studies on non-ultrasonic fatigue cycled specimens (Section 2.3.1) was said to transform the microstructure from PSBs to a dislocation cell structure. The microstructure of the large grain Cu shown in Figs. 54 and 55 are different from that of the small grain structure of Fig.

65 in terms of the degree of dynamic recovery or recrystallization, and in the observed cell wall thickness. The similarity that exists is in the shape of the cell structure in some areas of the large grain specimen (Fig. 55) to that of Fig. 65. These apparent differences and similarities between the two microstructures could indicate:

- 1) that grain size affects the transformation by introducing greater compatibility stresses in the small grain structure;
- 2) that the dislocations would have a reduced mean mobility distance since the grain boundaries of the small grain structure specimen would constrain their movement; and
- 3) that the rate of dynamic recovery is constant for both the small and the large grain specimens, however, the generated dislocation density is larger for the small grain specimen due to more sources of dislocation present in the form of grain boundaries. The combination of these possibilities could very well account for the thicker dislocation cell walls.

Fig. 66 is the transformed microstructure of a small grain ambralloy specimen. Planar dislocation arrangements, such as stacking fault segments (S) and pileups, are typically expected in low SFE metals. Dislocation pileups occur as a result of an obstacle blocking the slip process. They form until the force on the leading dislocation in the pileup is sufficient to make it break through the obstacle or in the case of screw dislocations, until the force is sufficient to cause cross slip of the leading dislocation. The

microstructure also shows splitting of dislocations into partials and some tangles in other areas of the specimen (not shown in the figure). Similar features observed in the small grain specimen were seen in the large grain microstructure but spread over the entire grain. A plausible explanation for the lack of any significant difference between the two microstructures is the extremely low SFE of the alloy which inhibits the dislocation cross slip process thought to contribute to some extent to the cellular structure observed in the Cu specimens above.

Perhaps the most interesting observations of specimens examined in this section were that of the brass specimens which showed different dislocation substructures - planar as in Fig. 67, or wavy with cell formation as in Fig. 68. Often, as in the case of the small grain metal, both planar and wavy features were seen (Fig. 69) in the same grain. This figure also shows dislocation veins in addition to cell formation. A similar line of reasoning as above can be followed here to explain the microstructure transformation. In the small grain brass specimens, the combination of the SFE, cell size and the larger compatibility stresses may have been just sufficient to cause cell formation. An interesting comparison between the planar substructure formed in brass and that of ambralloy shows an absence of pileups typically expected in low SFE metals. This may imply that the dislocations in the brass specimens are in the initial stages of vein or cell formation.

Fig. 70 is the boundary between the PZ and the OZ. The PZ at the bottom shows subgrains very similar to those observed in Cu (Fig. 54) while the OZ at the top shows planar dislocation activity. On closer examination of the boundary between these zones, dislocations can be seen propagating out of the bonding area. This observation could indicate that the region (OZ) surrounding the BZ resists deformation occurring in the BZ during UWB. The PZ which shows intense deformation is believed to be due to oxides and other surface contaminants which are dispersed away from the BZ during wire bonding.

Another interesting observation related to the brass specimens was that a planar microstructural transformation (Fig. 71) could be obtained using low bonding parameters⁸, while a cellular (wavy) microstructure transformation (Fig. 72) could be obtained by increasing the bonding parameters. This observation is similar to that described for Cu in Section 4.2.3 where an increase in the bonding time resulted in a cell formation. Another explanation could also be related to the SFE, dislocation mobility and cell compatibility stresses of the specimen being at a threshold value such that an increase in the bonding parameters is sufficient to cause an instability resulting in a cellular structure.

⁸Low bonding parameters indicates small values of bonding time, force and power.



Figure 65 Microstructural transformation of the BZ in a small grain Cu specimen.



Figure 66 Microstructural transformation of the BZ in a small grain ambralloy specimen.

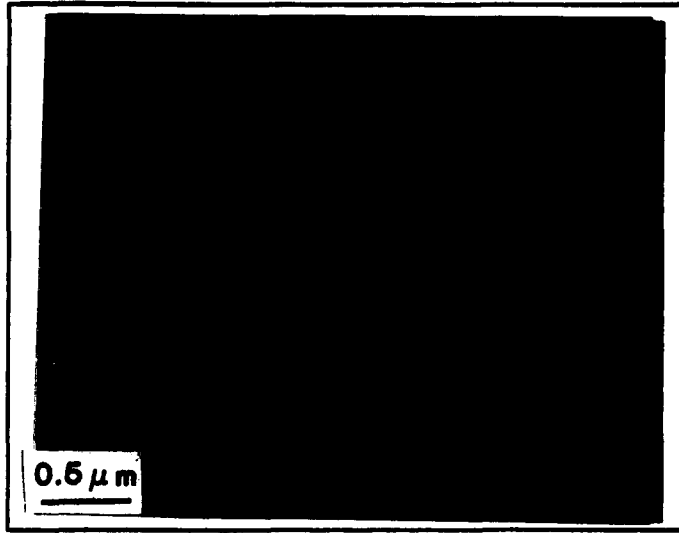


Figure 67 Planar dislocation structure in the BZ of a large grain brass specimen.



Figure 68 Wavy dislocation structure in the BZ of a large grain brass specimen.



Figure 69 Planar and wavy dislocation structure in the BZ of a small grain brass specimen.



Figure 70 Boundary between the PZ and OZ in a large grain brass specimen bonded using small parameters.

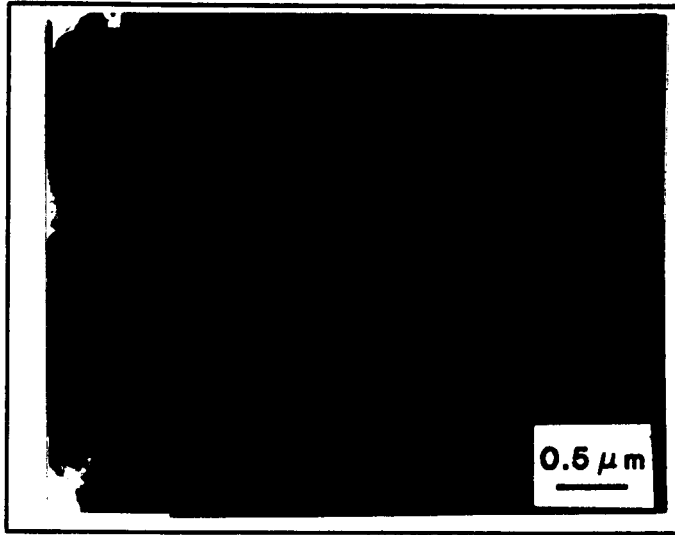


Figure 71 Boundary between the PZ and BZ in a large grain brass specimen bonded using small parameters.

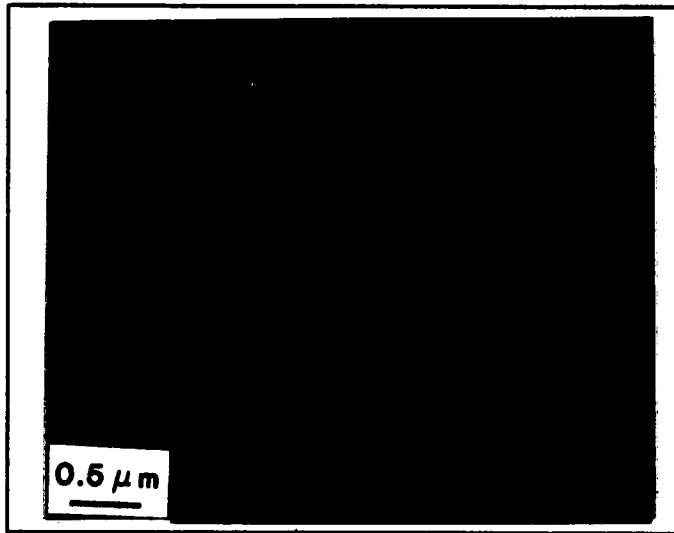


Figure 72 BZ in a large grain brass specimen bonded using large parameters.

5.2 Ambient Temperature and its Influence on the UWB Process-

The influence of temperature on the UWB process has often been a source of much debate. Earlier, in Section 4.1, a diffusion kinetic analysis based on dislocation loops observed in Al grains was shown to give an average bonding temperature of 250°C. Next, in Section 4.2.2 and 5.1, the transformed microstructure of substrates bonded at ambient temperatures of 20°C was described as partial recovery with dislocation veins and cells characterizing the BZ. In this section, observations of 3 mil Al wire bonded to annealed Ni200 substrates at ambient temperatures of a 150°C and 350°C are described.

Figs. 73 and 74 are transformed microstructures observed in plan view Ni specimens bonded at ambient temperatures of 150°C. Dislocation cells can be seen within a grain (Fig. 73) which appear to be smaller closer to the PZ in Fig. 74. The small grains in and near the PZ could indicate intense deformation possibly the result of oxide particles from the wire and surface contaminants being pushed outside away from the bond center during bonding.

At an ambient temperature of 350°C, wire bonding causes a greater degree of recovery with microband formation (Fig. 75), while the OZ in Fig. 76 shows large annealed grains not affected by the transformations in the BZ.

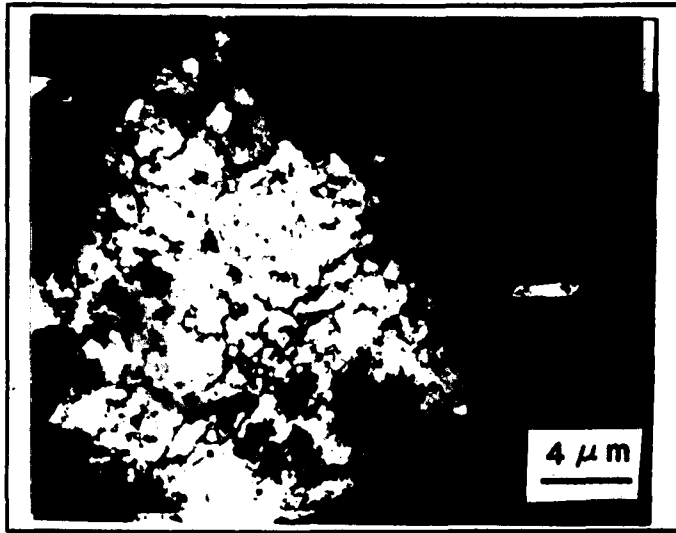


Figure 73 Microstructural transformation of the BZ in a Ni substrate bonded at 150°C.

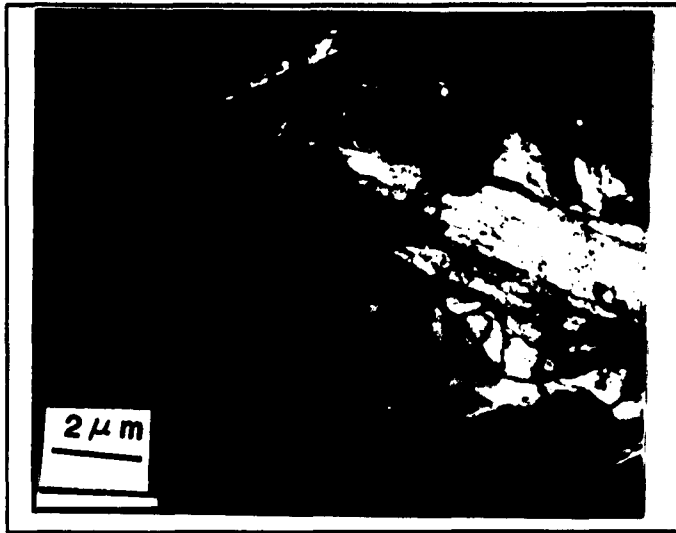


Figure 74 Microstructural transformation of the BZ in a Ni substrate bonded at 150°C.



Figure 75 Microbands in a Ni substrate bonded at 350°C.

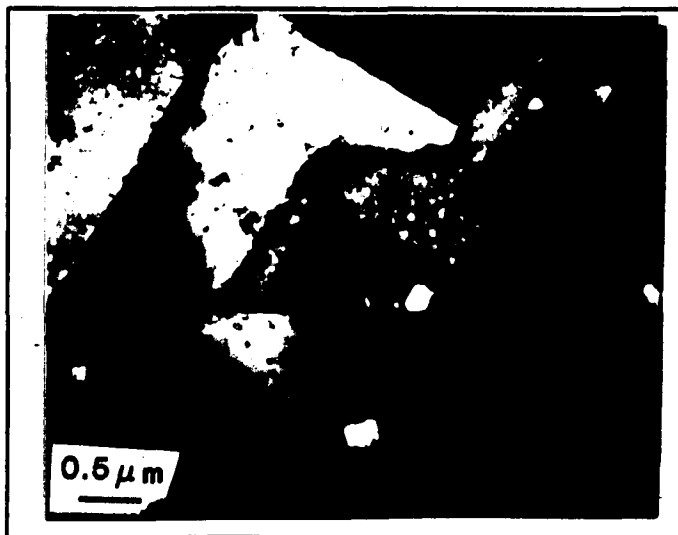


Figure 76 OZ of a Ni substrate bonded at 350°C.

5.3 A Model for Substrate Microstructural Transformation -

During UWB substrate microstructures transform to different extent. Some substrates such as stainless steel show little transformation with a few planar arrays characterizing the BZ, while others such as Al show complete recovery. The model developed below attempts to estimate the extent to which a substrate microstructure transforms during the UWB process using a parameter ω ranging from 1 to 0. When $\omega = 1$ it indicates complete substrate recovery and maximum transformation while $\omega = 0$ would indicate no recovery and minimum transformation.

At the outset, it should be stated that this is the first attempt of any kind at modelling substrate microstructural transformation during UWB. The model is simplistic in its approach and will warrant further improvements as the results of future investigations become known. The model required the following assumptions:

1) σ_{ys} characterizes the minimum stress required for dislocation slip, 2) Q the activation energy for microstructural transformation is the same as that for self diffusion, 3) an ambient temperature of 20°C exists with a substrate temperature rise of 100°C during bonding. The assumption for temperature rise is an arbitrary value stemming from the fact that reported values of average temperatures developed during the UWB process range from 80°C-250°C.

There are three stages associated with a microstructure

transformation:

(i) Dislocations need to be generated. Based on the above stated assumption related to σ_{YS} , this is possible if the applied stress of the bonding process is greater than the metal yield strength, that is:

$$\sigma_{App} > \sigma_{YS}.$$

The larger the ratio of σ_{App}/σ_{YS} , the greater is the number of dislocations generated during the process. This also implies that when $\sigma_{App} \leq \sigma_{YS}$, no dislocations will be generated as the deformation would be elastic and therefore no transformation occurs. The σ_{App} can be varied by changing the bonding parameters, but for the purpose of this model it is assumed as a constant value equivalent to 400 MPa. This value was chosen based on the fact that for all the substrate microstructures examined in this research, cold worked Ni foil showed minimal transformation and its σ_{YS} was assumed to be similar to that of shock tested Ni (Meyers, Chawla, 1984), approximately 400 MPa.

The reasoning described here gives rise to the first term in the model,

$$D = 0.1 \sigma_{App}/\sigma_{YS}.$$

The constant 0.1 is a scaling factor to make all terms in the model similar in range. The numerator can therefore be regarded as a constant $k_1 = 40$ MPa.

(ii) Cell formation. Cell formation is associated with the

metal SFE. The larger this value, the easier is dislocation cross slip resulting in cell formation. Also, the SFE is inversely related to the separation distance between the partials d_p . In the metal substrates examined, Al shows the maximum cross slip with a SFE = 250 mJ/m² and a d_p = 1 nm which formed the basis for the second term in the model,

$$C = k_2/d_p,$$

where k_2 = 1 nm.

(iii) Recovery effects. Dislocation annihilation is part of a recovery process where dislocations glide and interact with each other, or a thermally activated diffusion process involving climb. This term in the model would be associated with diffusion distances and activation energies for self diffusion. In this case it is assumed to be equal to that required for microstructural transformation. Al with Q = 142 KJ/mol showed the most recovery of the metal substrates examined. This formed the basis for the third term in the model,

$$X = k_3/Q,$$

where k_3 = 142 KJ/mol.

In addition to these three terms, the model needs to account for bonding time and ambient temperature. The greater the bonding time, the greater the transformation, as shown in Section 4.2.3 for Cu substrates. Also an increase in the ambient temperature was shown in the preceding section to

result in increased transformation. The bonding time was normalized by 0.06 seconds, the time required for good bonding, while the temperature was normalized by an ambient of 293°K, thus forming the basis for the last two terms of the model.

The final equation of this model can therefore be written as,

$$\omega = D \times C \times X \times K \times S, \quad \text{or}$$

$$\omega = \left(\frac{k_1}{\sigma_{ys}}\right)^m \left(\frac{k_2}{d_s}\right)^n \left(\frac{k_3}{Q}\right)^p \left(\frac{T}{k_4}\right)^q \left(\frac{t}{k_5}\right)^r$$

where the constants are, $k_1 = 40$ MPa, $k_2 = 1.0$ nm, $k_3 = 142$ KJ/mol, $k_4 = 293^\circ\text{K}$ and $k_5 = 0.06$ sec. The exponents m , n , p , q and r are weightage allowances to account for any effects not properly considered in the final equation of this model. For now they equal 1.

Table 5 lists the ω values along with different terms used in the model when applied to the different metal substrates with microstructural transformations at room temperatures, described in Chapter IV. It can be seen that

Table 5 : ω -model parameters for different metal substrates.

Metal	Q kJ/mol	σ_{ys} MPa	D	C	X	K	S	ω
Ni	279.7	70	0.57	0.34	0.51	1	1	0.099
Cu	200.3	60	0.67	0.31	0.71	1	1	0.147
Al	142.0	40	1.00	1.00	1.00	1	1	1.000
γ -Fe	284.1	280	0.14	0.03	0.49	1	1	0.0021

Al with an $\omega = 1$ shows maximum transformation, followed by Cu with $\omega = 0.147$. Ni and stainless steel with ω 's of 0.099 and 0.0021 are considerably smaller than that of Al or Cu and the corresponding microstructures also show some or little transformation.

Similarly the ω values of substrates of Cu and its alloys with ambient room temperature microstructural transformations described in this chapter are listed in Table 6. It can be seen that the highest ω values are associated with Cu which shows extensive microstructural transformation when compared with ambralloy showing little transformation. However, the small differences in the ω values between brass and ambralloy do not correlate well with the observed microstructural

Table 6 : ω -model parameters for Cu alloy substrates.

Metal	L μm	σ_{ys} MPa	d° nm	D	C	X	ω
Cu	10.16	61.51	3.2	0.65	0.31	0.71	0.143
	75.12	38.93		1.03			0.227
Brass	38.39	131.1	43	0.31	0.02	0.71	0.004
	104.51	60.26		0.66			0.009
A.alloy	29.89	128.2	96	0.31	0.01	0.72	0.0022
	70.58	70.9		0.56			0.004

transformation. A possible reason for this could be in the values of SFE used in calculating d_1 for these alloys. Also the model may not properly account for some of the diffusion

⁹ Estimated by calculations.

mechanisms taking place. The trend in the ω values is that the larger grain microstructure shows more transformation than the smaller grain microstructure, although whether the actual transformation observed follows this trend is questionable.

If for instance the grain size was substantially reduced to $0.005 \mu\text{m}$, such as in a fine electroplated structure, say Cu. The σ_{ys} obtained using the Hall-Petch relationship would be 1581.14 MPa. This would give a $D = 0.0253$. When introduced into the model, $\omega = 0.0056$, implying very little transformation. This is a substantial reduction from the earlier calculated ω of 0.147 for an annealed substrate. The value of 0.0056 is now in the same order of magnitude as stainless steel shown to have an $\omega = 0.0021$. The model agrees with microstructural examination of plated metals where no evidence for any transformation was observed even at extremely high magnifications.

Microstructural observations related to an increase in the ambient temperature described in Section 5.2 can also be justified on the basis of the developed model. In the case of Ni when the ambient temperature was increased to 150°C , the parameter $K = 1.44$ resulting in an $\omega = 0.143$. For an ambient temperature of 350°C , $K = 2.13$, giving an $\omega = 0.21$. Considering that the value of annealed Cu is 0.147, the microstructure observed in the case of Ni substrates bonded at higher temperatures shows slightly more recovery. The effect is small and is correctly predicted by the model.

Table 7: ω as a result of change in the ambient temperature.

Ambient Temp. °C	Microstr. Trans. Observed	ω
20	Veins/Disl. cells	0.099
150	Cells with some recovery	0.143
350	More recovery but still mainly subgrains, similar to Cu.	0.210

The values of ω and the microstructural observations are compared with those of Ni substrates bonded at an ambient temperature of 20°C in Table 7. It can be seen that as the ambient temperature increases, ω also increases from 0.099 to 0.210 and consequentially the extent of the microstructure transformation. An interesting similarity is the ω obtained for Ni bonded at an ambient temperature of 350°C (0.210) and that of Cu substrates bonded at an ambient temperature of 20°C (0.147). The microstructure in both instances shows evidence for a greater degree of recovery.

Microstructural transformations of Cu substrates by varying the bonding time as described in Section 4.2.3 can also be justified by the model. The S term is calculated for $t = 20, 60$ and 95 msecs to get ω 's of 0.049, 0.147 and 0.233, indicating more transformation with increase in the bonding time.

From the observations in this section it is seen that substrate transformation is effected by changing the bonding

ambient temperature, the average grain size or the bonding time. The implication of these observations on the UWB process will be incorporated into the proposed bonding mechanism to be described in Chapter VIII.

CHAPTER VI

MICROSTRUCTURAL TRANSFORMATIONS AFTER BONDING

Most observations reported in this chapter were presented at the recently concluded IVth Electronic Materials and Processing Congress in Montreal, Canada.

Reliability of UWB in electronic packages depends strongly on the type of package metallization used and the extent of exposure to aging or thermal cycling treatments. This is due to the formation of intermetallics that form under favorable conditions of temperature and pressure over time as was described in Section 2.4. Their detrimental effect on bond strength is affected by property changes as a result of a composition gradient, and in some cases also due to Kirkendall porosity.

In the previous chapter UWB was examined on both plan-view and cross-section view specimens. Although significant microstructural changes due to bonding were observed in both the wire and substrate, an analysis of the interface revealed no evidence for melting indicating that the UWB process is a true solid state process, also noted in an earlier paper (Krzanowski, 1989). In order to understand

possible metallurgical interactions between the wire and substrate, specimens can be cross-sectioned and observed using optical, scanning or transmission electron microscopy. The first two techniques have limitations, particularly in spatial resolution when very thin metallization layers are used. In this chapter TEM techniques are employed to investigate bimetallic interfaces created by bonding 2 mil diameter Al-2 wt% Si wire to plated Cu substrates. Specimens were examined in the "as-bonded", aged and thermal cycled conditions. It should be noted that in the as-bonded condition, specimens were heated to 90°C for 90 minutes during sample preparation. Energy dispersive spectroscopy (EDS) techniques were employed using a STEM to conduct a microchemical analysis of the wire bond interfaces. Finally pull and bondability tests were used to determine the reliability of bonding to these substrates.

6.1 Thermally Induced Transformations in Nickel - The Ni-Al system is highly reliable and tends to form intermetallics at higher temperatures than the Au-Al system. The following description is a result of thermally induced microstructure transformations after bonding onto bulk Ni and NiB plating.

6.1.1 Transformations in Bulk Nickel - Specimens of Al wires bonded to well-cleaned Ni foils were thermally aged at 500°C for different time periods. These were then metallographically mounted and polished for optical and

scanning electron microscopy viewing. Fig. 77 shows a SEM image of an intermetallic whose thickness was measured using an Ortholux Ernst Leitz Wetzlar optical microscope. The intermetallic plotted as a function of the square root of the aging time in Fig. 78 obeys the parabolic growth law described in section 2.4.

An x-ray micro-analysis in the SEM of the intermetallic indicated a composition varying from Ni-rich close to the Ni substrate at the bottom to Al-rich close to the Al wire at the top. Since spatial resolution of the SEM is limited and the microprobe used tended to drift, the details of this analysis have not been included.



Figure 77 SEM image of Al wire bonded to bulk Ni aged at 500°C for 24 h. Average intermetallic thickness in these specimens was 75 microns.

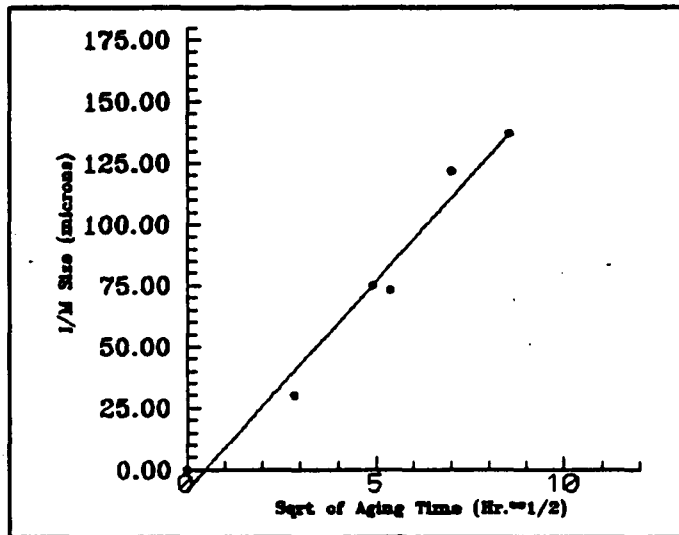


Figure 78 Al/Ni intermetallic thickness obeys the parabolic growth law.

6.1.2 Transformations in Nickel Boron Substrates - These substrates were examined in the as-bonded, aged and thermally cycled conditions. Fig. 79 shows a typical image of the Ni-B/Al wire interface in the as-bonded condition. The Ni-B substrate has a fine grain structure (20-50 nm), and forms a sharp interface with the wire. The microstructure of the Ni-B substrate is not affected by the wire bonding process. This is in sharp contrast to wire bonding of annealed coarse grained (50 nm grain diameter) Ni specimens in Fig. 47 (Section 4.2.2), where cell walls spaced 1 μ m apart were observed after bonding. This observation indicates that the extent of microstructural transformation during ultrasonic wire bonding can depend significantly on the initial microstructure of the substrate as discussed in section chapter V.

Table 8 : Analysis of Al/NiB interface (as-bonded specimen)

Distance from interface (nm)	Wt.% Ni	Wt.% Al
- 50	7.3 \pm 2.2	92.7 \pm 5.8
- 10	8.0 \pm 1.4	92.0 \pm 3.5
- 10	99.0 \pm 2.7	0.95 \pm 0.2
+ 50	99.7 \pm 3.1	0.25 \pm 0.1

A point chemical analysis was conducted on an as-bonded Al/Ni-B specimen in the STEM. The compositions, tabulated in Table 8 as a function of the distance from the wire-bond interface were obtained using the Cliff-Lorimer (1975)

equation. This analysis, described below was used to obtain the point composition for all specimens described in subsequent sections of this chapter.

A relative elemental sensitivity factor, k_{AB} , for element A relative to element B is defined as,

$$k_{AB} = \left(\frac{C_A}{C_B} \right) \left(\frac{I_B}{I_A} \right)$$

where C_A is the weight fraction of element A and I_A is the background corrected x-ray intensity. B is a reference element, which is usually taken to be silicon, although in this analysis, iron was used. Rearranging the equation,

$$C_A = k_{AB} \left(\frac{I_A}{I_B} \right) C_B$$

where the intensity ratio I_A/I_B is used to determine C_A . k_{AB} is a constant containing specimen specific factors, such as ionization cross sections, stopping powers, and sample absorptions for the elements A and B, as well as instrument-specific factors, such as x-ray window absorption and detector efficiency.

From Fig. 79 and Table 8, it appears that the wire-bond interface is chemically sharp to within ± 10 nm from the interface. There also appears to be a significant amount of Ni in the wire, however some of this may be due to spreading of the electron beam and scattering from the Ni-B substrate.

A second Ni-B/Al wire specimen was examined which had been aged for 8 hours at 125°C. An elemental map for this

specimen is shown in Fig. 80, where the elements O, Ni, and Al were mapped (the B level was too low to be detected). In this specimen a significant amount of O was present at the interface, mostly associated with the Al wire. Although quantification of oxides using energy dispersive analysis is difficult, the ratio of the Al/O peak led to the conclusion that aluminum oxide (Al_2O_3) was present at the interface. A thin layer of Ni oxide may also be present. The presence of Al oxides at wire-bond interfaces has been proposed in previous work (Krzanowski, 1989; Krzanowski, Murdeshwar, 1990) and as suggested in the previous chapters, may significantly contribute to the observed inhomogeneous deformation of the PZ.

Specimens subjected to 1500 and 3000 thermal cycles were also examined in the TEM. The wire bond interfaces again, appeared chemically sharp, with no indication of intermetallic phase formation.

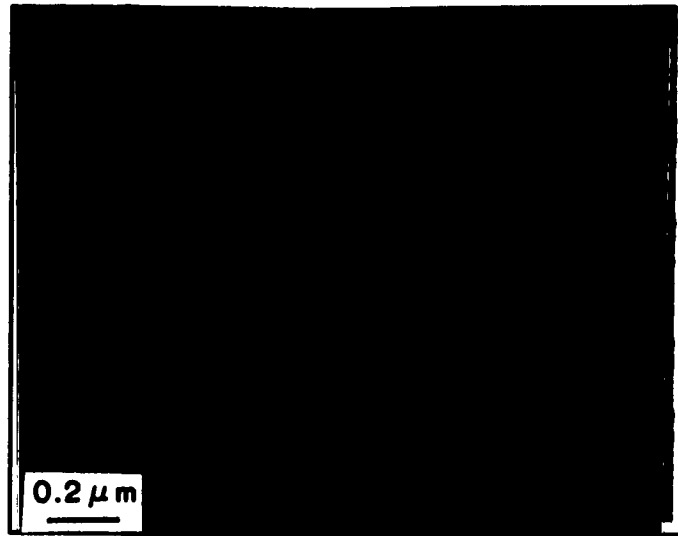


Figure 79 STEM image of the Al/Ni-B interface. Al is on the upper right and the Ni-B is at the lower left.

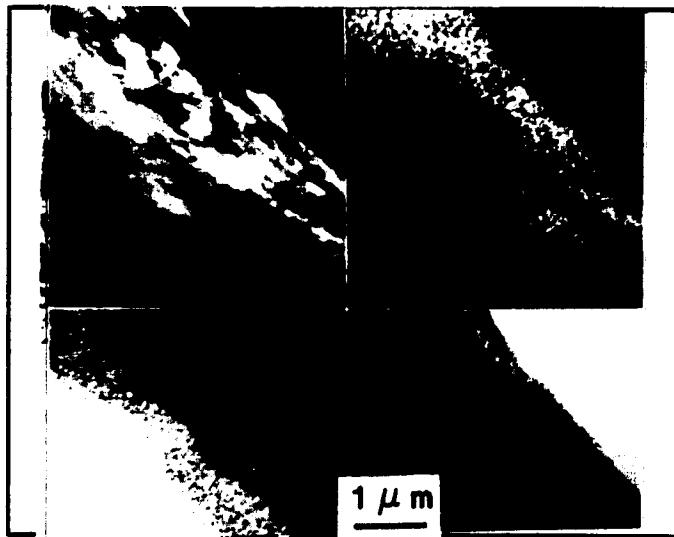


Figure 80 STEM image and elemental maps for Al/Ni-B specimen aged for 8 h at 125°C. The map shows O, Ni, and Al.

6.2 Transformations in Thin Gold Substrates - Examination of specimens with thin-Au metallurgy showed some surprising and interesting results. The Au layer on the Ni-P surface is typically 0.1 μm thick, and it was expected that this layer would be removed by bonding. However, TEM examination of thin-Au specimens shows that this does not occur.

Figs. 81 and 82 show bright field images of as-bonded specimens in the STEM and TEM, respectively. In each case, the Ni-P and Al wire are shown with a thick, dark layer in between. An elemental map of Fig. 81 is shown in Fig. 83, showing the location of the Al, Ni, and Au. The dark layer is primarily Au, with significant amounts of Al and Ni. The specimen was further studied by placing the beam on specific locations and conducting a semi-quantitative microchemical analysis. The locations are indicated by numbers in Fig. 81 with the results listed in Table 9. The first point in the Ni-P plating consists primarily of 7.5 wt.% P and 93.1 wt.% Ni. The second point in the lower part of the dark layer contains Al, Au, Ni and P. The table lists both weight and atomic percents, and shows the atomic ratio of Au to Al is 2.7, which is very close to the known equilibrium phase of Au_3Al_2 of ratio 2.5. The third point in the upper part of the dark layer, has a composition very similar to the second point. The fourth point is in the Al wire consisting mainly of Al with some Ni present. The observed Ni in this area may be in part due to scattering from the Ni substrate. Based on these

Table 9 : Microanalysis of points labelled in Fig. 81.

Point	% Al ¹⁰	% Au ¹⁰	% Ni ¹⁰	% P ¹⁰
1	0.45/0.9	-	93.1/86.0	7.5/13.0
2	4.7/25.0	92.7/67.6	2.1/5.1	0.5/2.3
3	4.7/24.7	92.0/66.1	2.7/6.5	0.6/2.6
4	90.0/95.0	0.1/0.01	9.4/4.5	0.1/0.5

observations, it can be concluded that the Au remains on the substrate during bonding, and reacts primarily with Al to form the intermetallic Au₅Al₂.

Fig. 84 shows a STEM image of a thin-Au sample aged at 125°C for 48 hours. The amorphous Ni-P substrate is seen on the left side of the image with the Al wire on the upper right. On the lower right portion of the interface, a layer of unreacted Au is present, while on the upper portion of the interface, a reaction product is present. In this case, the unreacted Au is present because it is located adjacent to a void between the wire and substrate. An elemental map for Fig. 84 is shown in Fig. 85 for Al, Ni, and Au which also confirms the presence of the unreacted Au layer. The results of the point microchemical analysis conducted on the specimen in Fig. 84 is listed in Table 10. The first point again shows

¹⁰ Weight/Atomic percent.

primarily Ni and P. The second point is the unreacted Au also containing 3.0 wt.% Ni, while the third point in the intermetallic adjacent to the Ni-P contains significant amounts of Al, Au, and Ni. The fourth point in the intermetallic close to the Al wire contains primarily Al and Au. The fifth point in the wire shows primarily Al with small amounts of Au and Ni.

Table 10 : Microanalysis of points labelled in Fig. 84.

Point	% Al ¹¹	% Au ¹¹	% Ni ¹¹	% P ¹¹
1	0.38/0.78	0.28/0.08	92.20/86.50	7.1/12.6
2	0.87/5.60	96.10/85.50	3.00/9.00	-
3	10.70/32.40	59.10/24.60	29.60/41.30	0.7/1.7
4	12.00/47.50	85.00/46.10	2.30/4.30	0.6/2.2
5	95.70/98.90	3.10/0.40	1.30/0.60	-

Analysis of the intermetallic at the fourth point, shows a Au/Al ratio close to 1, indicating that the phase is close to the known equilibrium phase of AuAl. The higher enrichment of this intermetallic phase, in comparison to the specimen in Fig. 81, is consistent with the longer aging time and higher aging temperature. If Ni was excluded from the analysis of the

¹¹ Weight/Atomic Percent.

third point, then the Au/Al ratio is close to 1. However, it is interesting to note that the (Au+Ni)/Al ratio is 2.03 which is close to the Au/Al ratio in Au₂Al. This is consistent with Philofsky's (1970,a) work where the AuAl phase was observed to grow into the Au₂Al phase.

Table 11 : Microanalysis of points labelled in Fig.86.

Point	% Al ¹²	% Au ¹²	% Ni ¹²	% P ¹²
1	91.10/97.90	6.80/1.00	1.90/1.00	0.12/0.12
2	50.70/86.20	45.50/10.60	3.50/2.70	0.37/0.55
3	0.92/5.20	91.10/70.80	6.60/17.20	1.30/6.7
4	0.05/0.11	0.11/0.03	93.70/88.8	6.10/11.0
5	2.10/4.30	0.92/0.26	90.90/84.7	6.10/10.7

A thin-Au specimen subjected to 1500 thermal cycles specimen is shown in Fig. 86. In this image, the Al wire is on the lower left and the amorphous Ni-P substrate is at the upper right. An elemental map is shown in Fig. 87 which confirms the dark area on the upper portion of the interface to be an intermetallic and indicating the presence of a void in the lower portion of the interface. The results of a point microchemical analysis

¹² Weight/Atomic Percent.

conducted on the points labelled in Fig. 86 are listed in Table 11. The first point in the Al wire shows primarily Al with some traces of Au and Ni. The second and third points in the intermetallic layer primarily contain Al and Au respectively. The third point also contains significant amounts of Ni and could be a ternary intermetallic compound. However, it is interesting to note that the $\text{Au}/(\text{Al}+\text{Ni})$ ratio is 3.2 which is in between the Au/Al ratio in Au_3Al_2 and Au_2Al of 2.5 and 4. Points four and five are in the Ni/P layer, with the latter being adjacent to the void. The composition of both these points are similar and show the P content to be 6.1 wt.%. In this specimen, there was no unreacted Au layer adjacent to the void, indicating that the thin Au layer initially present interdiffused either with the NiP or, along the interface during the thermal cycling process.

From the foregoing analysis, a consistent picture of the diffusion process for thin-Au specimens begins to emerge. First, diffusion of Au and Al at the interface occurs to form Au_3Al_2 . This intermetallic forms rapidly either during specimen preparation or immediately after bonding. At long periods of aging, the Au_3Al_2 layer adjacent to the Al wire transforms into a thin layer of AuAl while the layer adjacent to the Ni forms a ternary compound of the type $(\text{Au}, \text{Ni})_2\text{Al}$. During thermal cycling, no AuAl was detected, however Au_3Al_2 incorporates Ni to transform into a ternary compound.

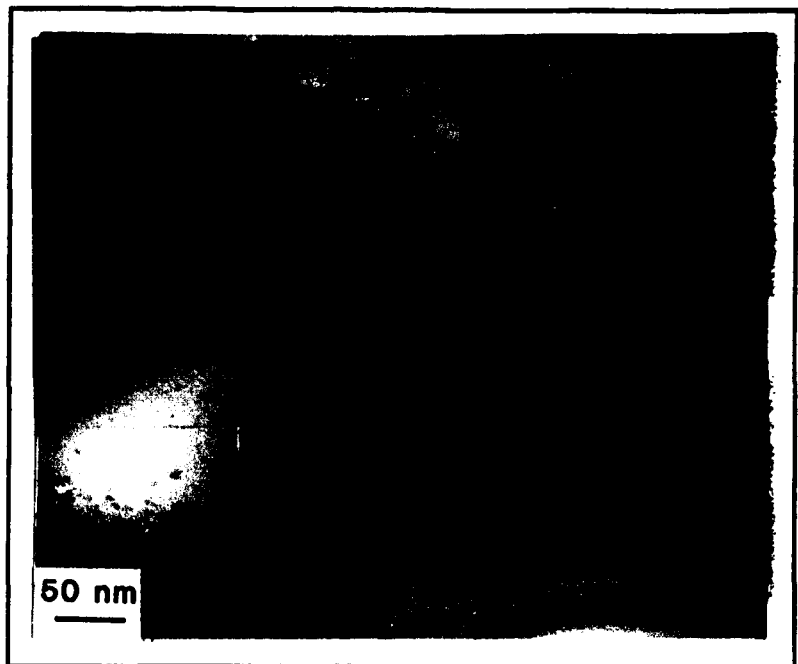


Figure 81 Bright-field image of the thin-Au specimen in the as bonded condition. The Al wire (top) and the Ni-P substrate (bottom) are separated by an intermetallic layer (dark region).

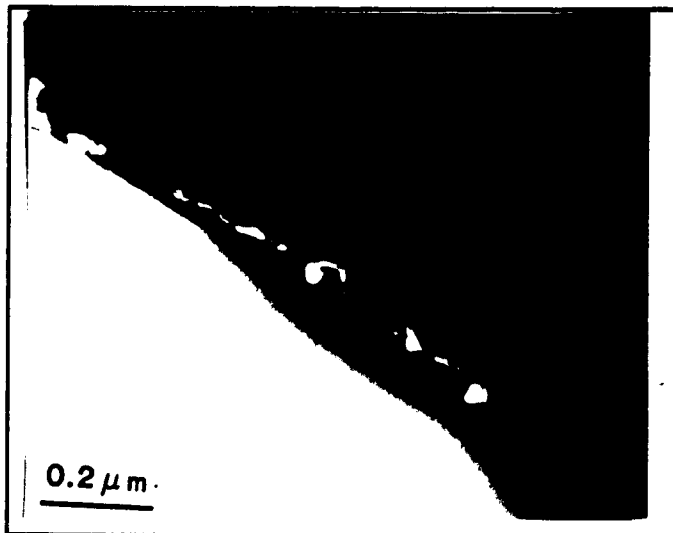


Figure 82 Bright-field image of the thin-Au specimen in the as bonded condition.

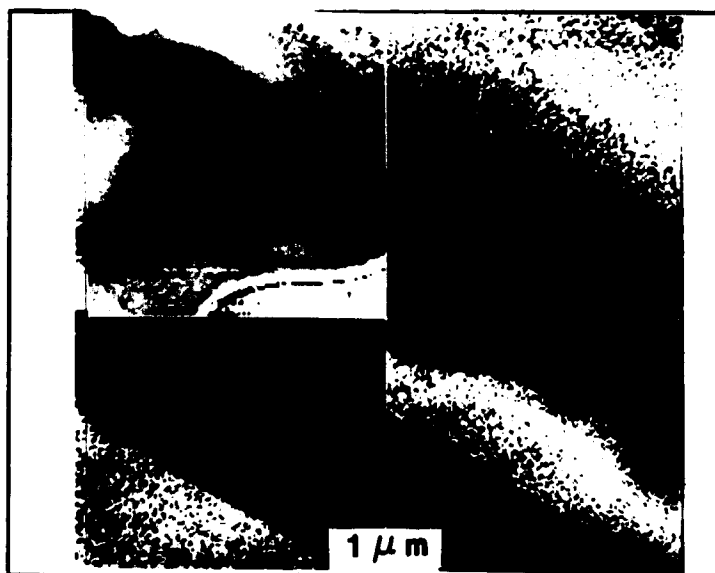


Figure 83 Elemental map for the image shown in Fig. 81. The upper left corner shows the image followed by Al, Ni, and Au maps.

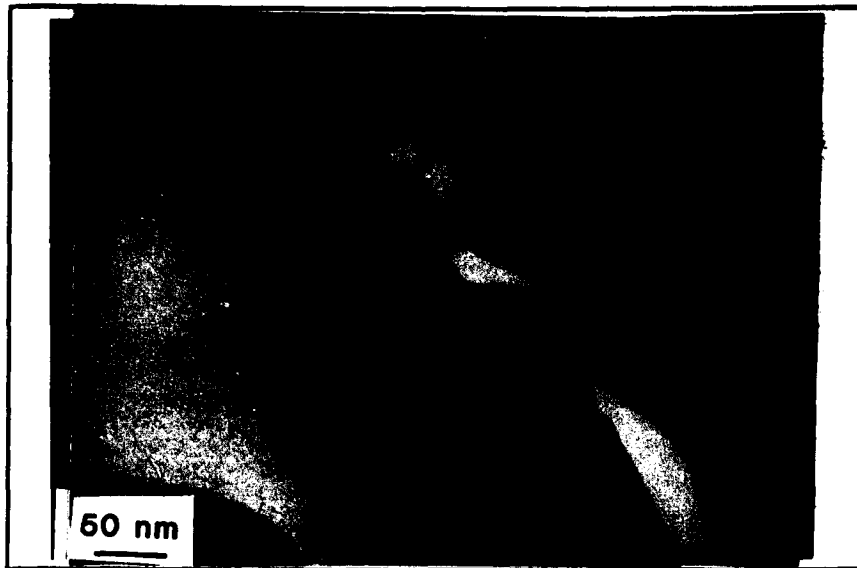


Figure 84 STEM bright-field image of the thin-Au specimen aged for 48 h at 125°C. Note the unreacted layer of immersion Au on the Ni-P coating near a void.



Figure 85 Elemental map for the image shown in Fig. 84. The image is shown along with Al, Ni, and Au maps.

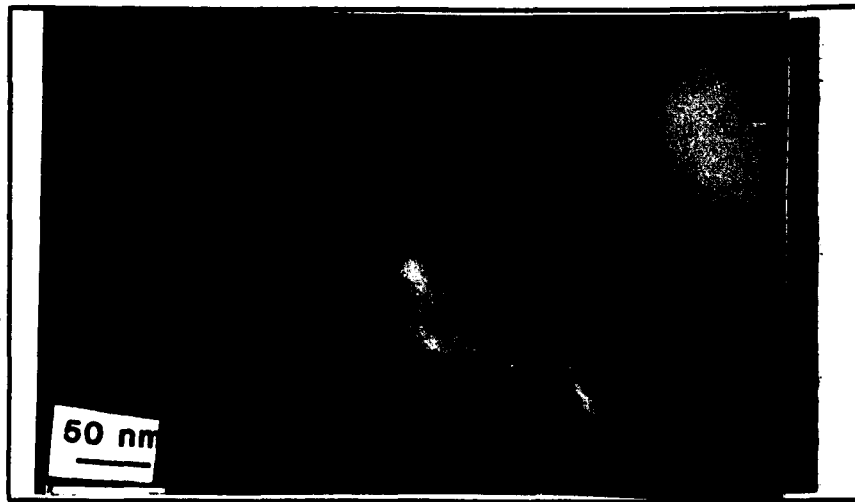


Figure 86 STEM image of a thin-Au specimen after 1500 thermal cycles. Al is at the lower left while Ni-P is at the upper right.



Figure 87 Elemental map for the image shown in Fig. 86. The image is shown along with Al, Au, and Ni maps.

6.3 Transformations in Thick Gold Substrates - Observations of thick Au plated specimens that were examined in the TEM and STEM were difficult for two reasons: 1) during ion milling, the thick-Au layer thinned much more rapidly than the Al or Ni, leading to electron transparent Au areas with thick Al and Ni areas, and 2) rapid diffusion of Al and Au made TEM observations of the true as-bonded condition impossible. The results are therefore presented only for specimens subjected to 1500 and 3000 thermal cycles and aged (8 hours at 125°C) conditions.

An elemental map for a specimen subjected to 1500 thermal cycles is shown in Fig. 88 along with a dark-field image in the upper left corner. The point microchemical analysis is given in Table 12. The first point is adjacent to the original Al/Au interface, and shows the presence of Al, Au, and Ni; examination of the atomic percents reveal that the composition is mostly Al. The other side of the Al/Au interface (second point) shows nearly equal atomic percentages of Al and Au, and also contains a significant amount of Ni. Based on the Al/Au ratio, the intermetallic would be AuAl, but the presence of Ni may result in the formation of a ternary intermetallic compound. The third point in the middle of the layer, revealed mostly Au, with Al and Ni present in nearly equal atomic amounts. The Au/Al ratio is 4.9, which does not correspond to any intermetallic phase in the Au/Al system, but is closer to Au₅Al. However, it is also interesting to note that the

Au/(Al+Ni) ratio is 2.4, which is close to the Au/Al ratio in Au₃Al₂. At this point it is not known whether a new ternary intermetallic phase is formed, or if Ni is substituted for Al in the Au₃Al₂ compound. A TEM bright field image of the Intermetallic formed between the second and third points is shown in Fig. 89. It is quite possible that the voids near the edge on the right side of the image are a result of Kirkendall porosity. Analysis of the fourth point in the Au layer adjacent to the Ni substrate, reveals the presence of only Au and Ni. Finally, the fifth point gives the composition of the Ni substrate as nearly pure Ni. This analysis shows that while some Au diffuses into the Al wire, there is little diffusion of Au into the Ni substrate. Furthermore, both Al and Ni diffuse into the plated Au layer.

Table 12 : Microanalysis of points labelled in Fig. 88.

Point	% Al ¹³	% Au ¹³	% Ni ¹³
1	43.30/78.20	43.50/10.80	13.20/11.00
2	10.30/42.00	83.90/47.10	5.80/10.90
3	2.50/14.40	91.80/71.00	5.60/14.70
4	-	75.50/47.90	24.50/52.10
5	0.28/0.62	0.74/0.22	99.00/99.20

¹³ Weight/Atomic percent.

Analysis of a specimen subjected to 3000 thermal cycles is shown in Fig. 90, with a dark-field image of the specimen in the upper left portion of the image. The results of the point microanalysis experiments are shown in Table 13. In this specimen, a distinct layer was observed to have formed at the original Al/Au interface, analyzed as the first point. The

Table 13 : Microanalysis of points labelled in Fig. 90.

Point	% Al ¹⁶	% Au ¹⁶	% Ni ¹⁶
1	12.80/49.70	84.10/44.70	3.10/5.60
2	3.30/19.10	94.60/75.20	2.10/5.70
3	1.80/6.20	54.20/25.20	44.00/68.60
4	0.15/0.33	0.61/0.18	99.20/99.50

composition reveals the formation of the AuAl intermetallic compound containing very little Ni. Analysis in the intermetallic phase close to the Al wire (second point) shows the composition to be similar to that found in the specimen subjected to 1500 thermal cycles. An analysis of the point adjacent to the Ni in the Au layer (third point) revealed the presence of mostly Ni and Au, while in the Ni layer the composition was essentially pure Ni. These observations show

¹⁶ Weight/Atomic percent.

that the specimen subjected to 1500 thermal cycles is similar to that subjected to 3000 thermal cycles except that in the latter a more distinct layer of the AuAl compound is formed at the Al/Au interface.

Fig. 91 shows a dark-field image and an elemental map of the specimen which was aged for 8 hours at 125°C. Unfortunately, this specimen was relatively thick so the microchemical analysis was limited to the areas near the small (dark) holes in the Au layer. On the Ni side of these holes, the composition was 26 at.% Al, 12 at.% Ni and 62 at.% Au. The Al side revealed 48 at.% Au, 7.4 at.% Ni, and 44.6 at.% Al. These results indicate that AuAl forms on the Al side, while a ternary Au-Al-Ni forms on the Ni side.

The formation of voids was noted in most of the thick-Au specimens. Fig. 92 is a typical area in an intermetallic layer of a 1500 thermal cycled specimen displaying voids. These voids are usually about 0.1 - 0.5 μm in diameter. However, it is not known if the voids form due to the ion milling process, Kirkendall porosity, or both. The formation of voids in relatively thick sections of the Au layers indicates that at least some of the voids were probably due to Kirkendall porosity.

From the foregoing analysis, a consistent picture of the diffusion process for thermally cycled thick-Au specimens begins to emerge. First, there is some diffusion of Au or Al into the Ni plated layer. In the Au layer near the Au/Ni

interface, ternary intermetallic compounds of the type $Au_3(Al,Ni)_2$ are formed. Near the Al side the intermetallic is less rich in Ni, while for longer diffusion times the formation of the compound AuAl was observed.

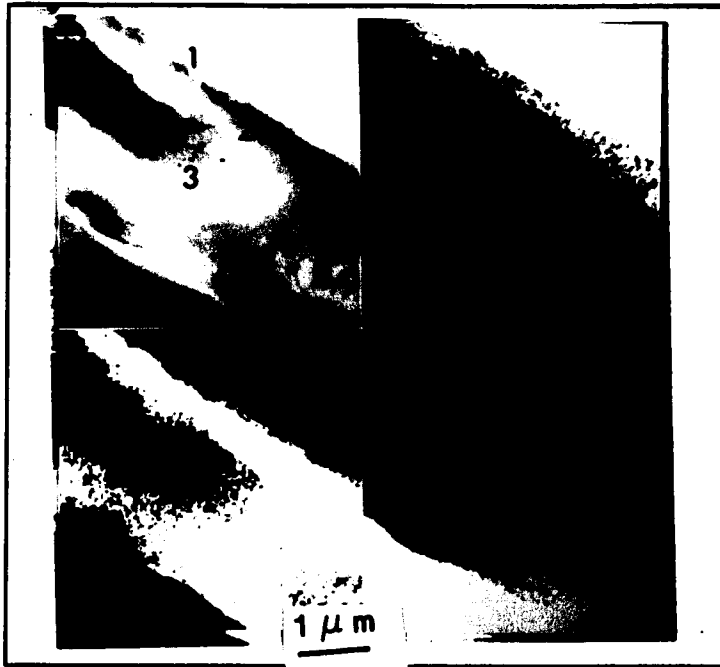


Figure 88 Dark-field STEM image and elemental maps for thick-Au after 1500 thermal cycles.

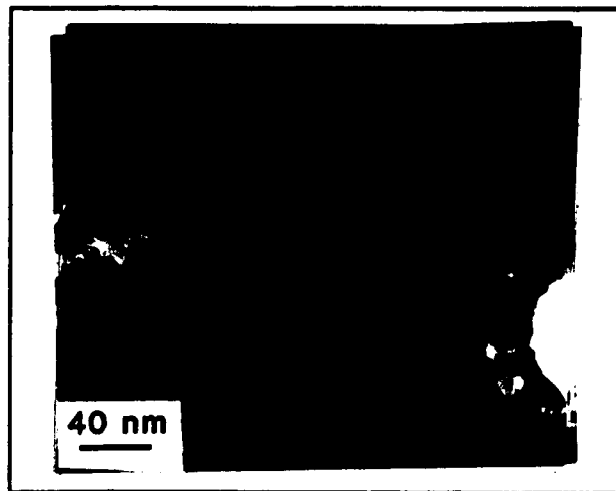


Figure 89 TEM bright-field image of the intermetallic formed in the thick-Au specimen after 1500 thermal cycles.

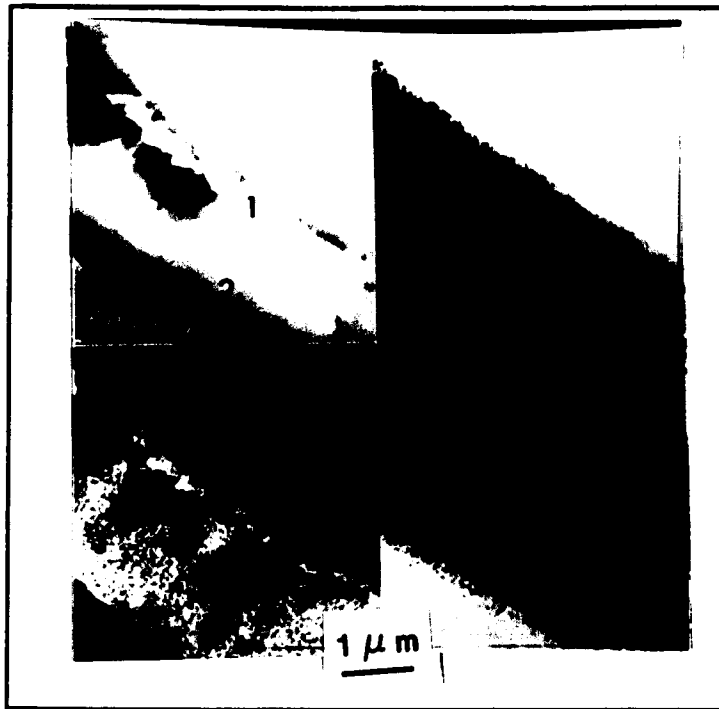


Figure 90 Dark-field STEM image and elemental maps for thick-Au specimens after 3000 thermal cycles. Numbers indicate locations for microchemical analysis.

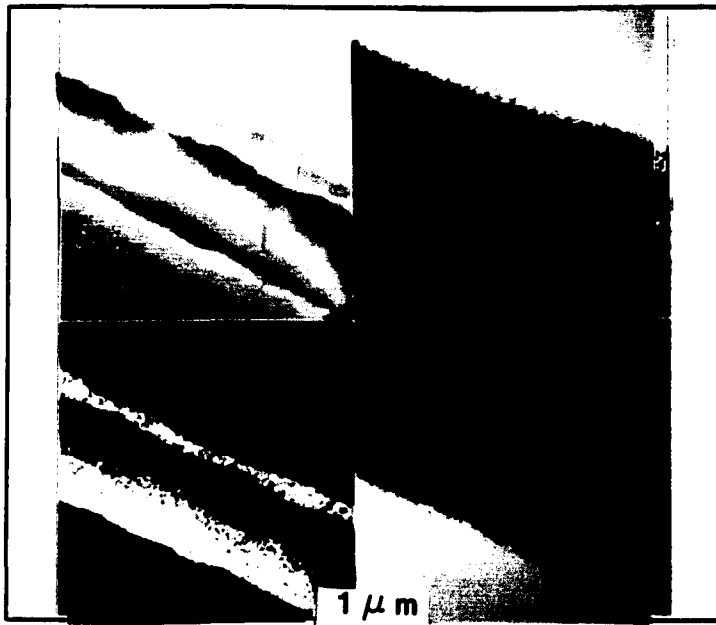


Figure 91 Dark-field STEM image and elemental maps for a thick-Au specimen aged 8 h at 125°C.

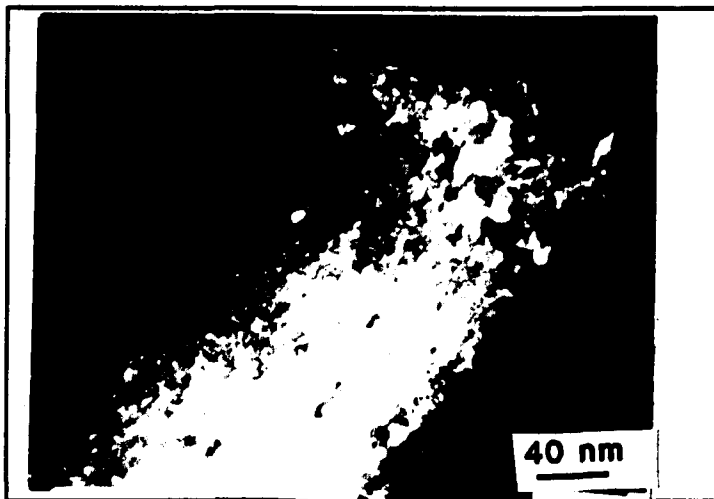


Figure 92 TEM image of the intermetallic in a thick-Au specimen subjected to 1500 thermal cycles. Note the presence of voids.

6.4 Bond strength measurements - To further understand the role of substrate microstructure a bondability test was done using Al-0.5 wt% Mg 3 mil wire on different plated substrates. The results shown in table 14 indicate the ability of a substrate to deform under the wire during bonding. The tests were done on Ni-P, Ni-B and Ni platings with no Au plating, and on Au plated Ni. From the table, it can be seen that substrates such as Ni-P and Ni-B, expected to be the hardest have the lowest pull strengths. The electroplated Ni had a larger grain size than the Ni-B, and therefore measured a higher pull strength. The Au plating, expected to have the lowest yield strength, had the highest pull strength. These observations interpreted as a function of grain size were discussed in chapter V with respect to the developed model.

To evaluate detrimental effects of observed intermetallics formed at bond interfaces, bond pull strengths were measured by the method described earlier in Section 3.2. These studies were conducted on each type of substrate materials for bonds in the as-bonded condition, and after 1500 and 3000 thermal cycles. The bond pull strengths for bond breaks only are shown in Fig. 93. The percentage of pull tests which resulted in bond breaks (as opposed to wire breaks) for each case is shown in Fig. 94. The thin-Au specimens had consistently lower bond pull strengths in comparison to the thick-Au or the Ni-B specimens, although even for the thin-Au specimens the strength level was

Table 14 : Bondability test results.

	E/P Ni	Electroless Ni-P	Electroless Ni-B	E/P Au on Ni
Full Strength (gm)	19.5	14.0	14.4	24.2
No. of bond breaks	14	15	12	17

relatively good. There does not appear to be any consistent pattern of bond strength degradation with thermal cycling. The percent of bond breaks vs. thermal cycles also failed to show any consistent trend. Therefore, despite the formation of intermetallic compounds in the Au-plated substrates, the bond strength was not significantly affected.

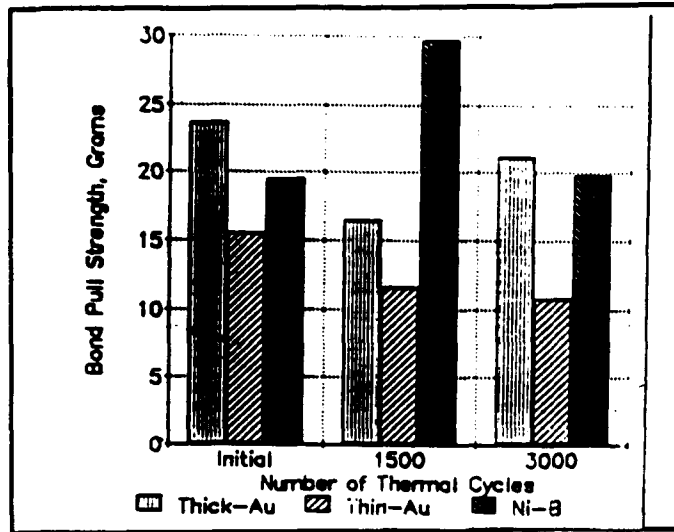


Figure 93 Bond pull strength for wire bonded specimens in the as-received condition, and after 1500 or 3000 thermal cycles.

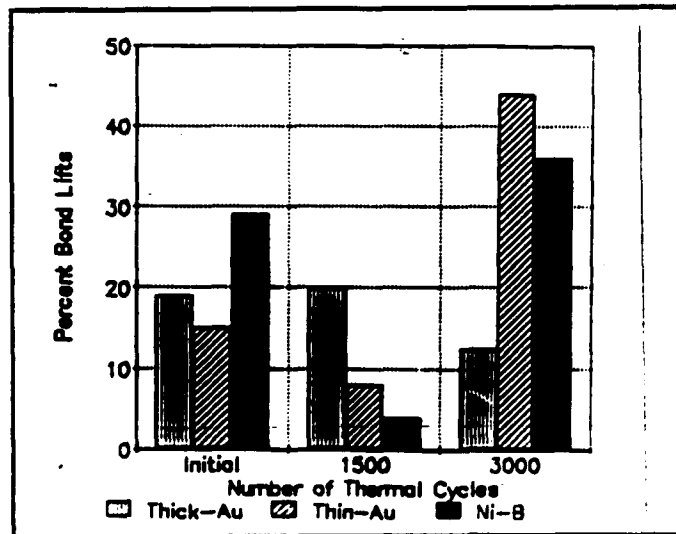


Figure 94 Percent of bond lifts for wire bond specimen test results in Fig. 93.

CHAPTER VII

THE EFFECT OF SURFACE CONDITION ON UWB

In Section 4.2.1, contamination at the bond-wire interface was discussed implying a relationship between surface roughness, substrate hardness and the extent of contamination. Based on observations in that section, it was thought that if the contaminant was contained only within surface asperity wells and not expelled from the bond interface, roughening the substrate surface would result in good bonding. This line of thought is quite in tune with Joshi's (Joshi, 1971) investigation where it was reported (Riben, Sherman, Land, Geisler, 1967, as referenced in Joshi, 1971) that a surface roughness of 75 μm or less was ideal for ultrasonic bonding of Al-Al and Al-Au. It was also observed by Joshi, that slightly oxidized Cu substrates yielded better bonds than an electropolished Cu substrate. The need for an optimum surface roughness was attributed in that study to elimination of slippage during bonding.

This chapter further investigates these topographic features of the substrate surface and its relationship to the bond strength. Substrates of two extreme types of hardness

were used. The soft substrate was annealed pure Al, while the hard substrate was annealed 304 stainless steel. The degree of surface roughness in the Al substrates was varied by electropolishing in 15% HNO₃ in methanol at -35°C, and by polishing with either 0.05 μm alumina, 3.0 μm diamond paste, or by grinding with a 600 grit paper for a 40.0 μm surface finish. Surface roughness variations on the stainless steel substrates were similarly obtained with the exception of the electropolishing which was not conducted.

To study the effect of contamination on prepared substrate surfaces, they were coated with an approximately 40.0 nm thick carbon layer in a Ladd vacuum evaporator. Al wires bonded onto these, and the clean substrates were then pull-tested to determine bond strength, by the method outlined in Section 3.2. 80-90% of the pull tested bonds resulted in bond breaks, with the remainder being wire or heel breaks. However, only the data from the bond breaks were used in the analysis presented below.

7.1 Aluminum Substrate - The bond pull strengths for wires bonded to the Al substrates are shown in Fig. 95. A data point represents the average of approximately 20 pull tests each with bond breaks. The error bars represent the standard deviations about this average. For the clean Al substrate, the 3.0 μm finish gives the highest strength, while for the C-coated substrate, the 0.05 μm finish is the highest. However,

the differences in strength between substrates are not significant, with the possible exception of the 0.05 μm substrate. It should be noted that even with the electropolished finish and 40.0 nm of C-coating on a specimen surface, excellent bond strength was obtained.

The incorporation of surface contaminants is demonstrated in Figs. 43-45. For clean surfaces, as in Fig. 43, bare metal to metal contact will result in high bond strength. If surface contaminants are present on the bonding surface, then the factors effecting bond strength are its size, surface roughness and the substrate hardness. When the contaminant is larger than the asperity wells, such as in Fig. 44, then inadequate metal to metal contact results in low bond strength. When the asperity wells are larger than the contaminant size, such as in Fig. 45, they serve as locations for placing the contaminants so that asperity tips can bond. This implies that the worst condition for bonding would be a smooth surface heavily contaminated. This bonding condition was created with an electropolished finish on an Al substrate coated with C. Wires bonded to this substrate showed pull strengths no worse than samples with other surface roughness/contamination conditions suggesting that in the initial stages of the bonding process, contamination is removed until bonding of the wire begins. After that point, the remaining contamination will be entrapped along the interface. This explanation is valid for Al wire bonding to

soft metal substrates since both surfaces are readily flattened by ultrasonic vibrations.

7.2 Stainless Steel Substrate - The bond pull strengths for wires bonded to the stainless steel substrates are shown in Fig. 96. A data point represents the average of approximately 20 pull tests each with bond breaks. The error bars represent the standard deviations about this average. Clean surface samples showed no significant variation in pull strength with surface finish. For the C-coated specimens, the 0.05 μm finish sample showed significantly lower pull strengths, while the 3.0 μm finish sample showed the same pull strength as the uncoated sample. The significance of the 40.0 μm finish sample showing a lower pull strength with the C-coating is questionable.

A maximum strength was found for a roughness of 3.0 μm . Without C-coating, a high pull strength was found for all surface roughness conditions. This suggests that in the case where the roughness is 0.05 μm the interface is not flattened sufficiently to enable all of the C to be expelled from the bond interface, and that the amount of C trapped along the interface is sufficient to reduce the bonding area and consequently the bond strength. When the roughness is increased to 3.0 μm , the C is contained within the bond by being displaced to low-lying asperity wells thus allowing bonding to occur at asperity tips. With rougher surfaces, the

C appeared to cause an insignificant decrease in bond strength.

A TEM image of bonding to a hard substrate is shown in Fig. 97. In this figure a cross section view specimen of Al wire is bonded to Ni-B plating. The void in the Ni-B plating can be considered to be an asperity well. In this case the Ni-B plating is hard and does not soften with ultrasonic vibrations. The Al wire therefore has to soften sufficiently in order to fill the asperity, thus ensuring complete metal to metal contact. In fact in the bondability tests on Ni-B plating described in the previous chapter, a possibility for low bond strength could also be the presence of many such voids in the plating that could ultimately hinder adequate metal to metal contact.

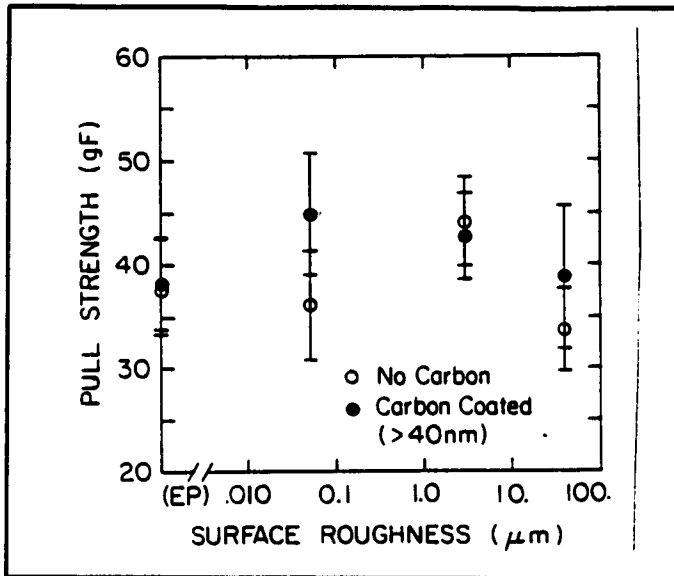


Figure 95 Bond pull strength versus surface roughness for wires bonded to pure Al substrates.

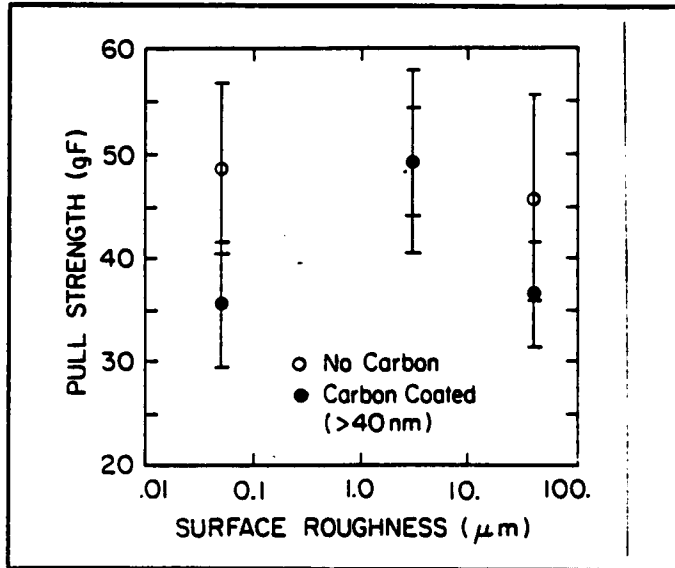


Figure 96 Bond pull strength versus surface roughness for wires bonded to 304 stainless steel substrates.

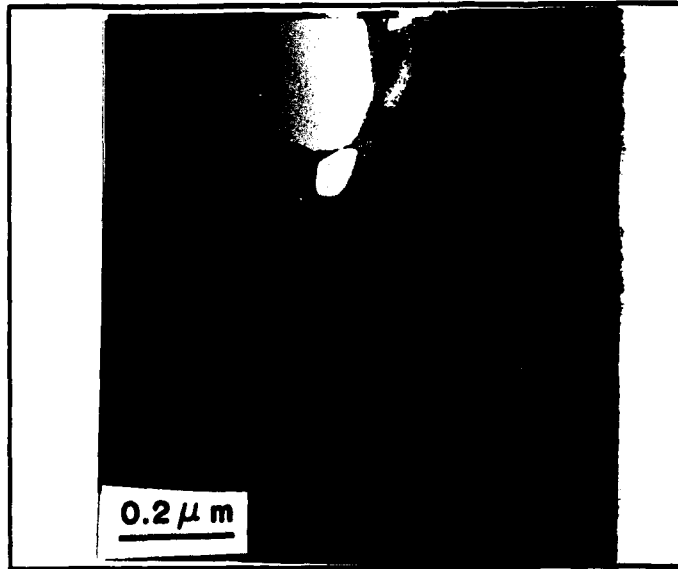


Figure 97 Cross section view specimen of Al wire bonded to Ni-B plated substrate.

CHAPTER VIII

DISCUSSION

8.1 Proposed Mechanisms of Bonding and Microstructural

Development - A bonding mechanism can be hypothesized based on observations stated in this research and by building upon proposals from earlier investigations. First, a brief summarization of the substrate microstructure observations described in chapter IV is presented in Table 15.

The Al wire and substrate, both reveal dynamically annealed completely recovered microstructures even though the former underwent considerable deformation during bonding. Dislocation loops were observed in both microstructures. A kinetic analysis based on the width of a zone near a grain boundary in the wire depleted of loops indicated possible temperatures attained during the bonding process. The substrate microstructure was characterized in terms of the extent it transformed during wire bonding. The Al substrates showed the maximum transformation of all metal substrates examined in this study by showing complete recovery. The Cu substrates showed less recovery than Al with partially

Table 15 : Summary of observed substrate transformations.

Substrate Used	Microstructure Observation	
	Cold Worked	Annealed
Al	Equiaxed grains. Low angle grain boundaries. Dislocation loops. Low dislocation density. Strong evidence for dynamic recovery.	Randomly oriented grains similar to a polycrystalline material. Size of grains seems to suggest dynamic recovery.
Ni	Considerable dislocation activity. Some evidence for cell formation.	Dislocation veins. Dislocation dipoles. Low dislocation density. Dislocation bundles. <u>No evidence</u> of either dynamic recovery or recrystallization. Tendency to form cells at larger bonding times.
Cu	Thick walled cells could suggest recovery.	Cell formation with subcells. Increase in dislocation activity within cells. Thickness of subgrain wall could suggest partial recovery. Rounded, equiaxed cells at larger bonding times.
γ Steel	-----	Planar dislocation activity. Loops, dipoles, pileups, and nodes.

recovered dislocation cells. Ni and stainless steel substrates were much less transformed by UWB with the microstructure in the former characterized by dislocation veins and the latter showing some planar dislocation activity. As stated earlier in Section 4.2.3, there is some ambiguity at this point in the

observed Al and Cu microstructures regarding recovery or recrystallization. Microstructurally, a recrystallized grain structure is expected to consist of small thin walled misoriented subgrains causing much contrast variations. Such a structure would characterize the entire specimen microstructure. On the other hand, a recovered grain structure is expected to contain large thick walled grains with the extent of recovery varying from point to point in the specimen. This is different from a recrystallized structure which exists throughout the entire specimen. For substrates examined in chapter IV, this structure variation is observed. Therefore even though recrystallized type cells are observed in some specimens, it is thought that the variations in the microstructure are largely an effect of recovery. Whether it is recrystallization or recovery, the common feature standing out in substrates examined needs emphasizing, namely the strong bonding of the Al wire to the substrate despite the observed microstructural differences in transformations. This indicated that microstructural transformations are a result of the bonding process and not a criterion for good bonding.

Observations of aged bonds to bulk Ni and electroplated Au and Ni substrates showed that intermetallics form at the wire-substrate interface given the optimum conditions of temperature and aging time and have been further discussed in the next section. A factor relevant to the present discussion

though, is the difference in the extent of microstructural transformation observed in large grain annealed Ni bulk specimens and fine grain Ni-B plating. The former showed ultrasonic transformation in the form of dislocation veins while the latter showed no visible effect of UWB. This phenomenon was discussed in Section 5.3 with respect to the ω values of the developed model. An interesting effect to be noted is the possible effect of the ratio of the bonding wire diameter (d_w) to the grain size (d). If this ratio is small, the compatibility stresses developed between the grains is small since only the grains below the wire deform plastically and little deformation occurs outside this area. If the ratio is large, then there will be many grains that deform to accommodate the effects associated with the UWB. This will result in larger compatibility stresses developed in the grain boundaries and the grains themselves will show very little or no transformation. The ω values of the model shows this effect.

Perhaps the most important requirement for good bonding is the cleanliness of the bonding surface in conjunction with substrate topography. Asperity tips in soft substrates sufficiently soften by ultrasonic irradiation leading to flattening and thereby ensuring good metal to metal contact. Asperities do not soften in hard substrates, in which case the Al wire softens enough to fill the asperity wells. For smooth electropolished substrate surfaces, the bond shows no

significant increase in pull strength. A possible cause for this is that slippage between wire and substrate with tool vibration prevents adequate contact during initial bond formation. For very rough surfaces, the asperity wells are large and desired wire deformation may not take place, thus resulting in poor bonding. This implies that an optimum surface roughness is required for good bonding irrespective of the substrate hardness (bonds of reasonable strength can even be obtained on ceramics). The essential criterion here is that the wire should be able to deform sufficiently enough to cause metal to metal contact for good bonds.

Various proposals on the bonding mechanism presented through the years are described in Section 2.2. It has been established that no movement between wire and substrate occurs, ruling out mechanisms related to friction bonding. It has also been established that neither melting nor diffusion play a role in the bonding process. In fact, sufficient evidence has been provided in these investigations to indicate that UWB is a solid state process.

At the start of the bonding process it is acknowledged that initial vibrations break up and disperse the oxide coating on the wire exposing bare metal contact. Some of this may be incorporated in the bond as contamination detected through an EDAX analysis. It is speculated that softening is due to defect generation when acoustic energy is dissipated at defects in the Al wire. This phenomenon has been suspected to

be associated with the effect of ultrasonic vibrations on metals and has been demonstrated in early work, by the decrease in the yield point and static stress in metals subjected to ultrasound, and in electrical resistance studies. In fact Severdenko et al. (Severdenko, Klubovich, Stepanenko, 1972) offered a plausible explanation based on dislocation theory which is briefly described in Section 2.1. There is strong evidence in previous investigations and in this study to indicate the dissipation of ultrasonic energy at microstructural defects. These studies show that the greatest accumulation of dislocations in samples subjected to intense ultrasound is found at the grain boundaries, cracks, and other defects, which are preferred sources for the nucleation of new dislocations. It should also be noted that relatively less energy is required for dislocation movement than to nucleate new dislocations. In short, the acoustic energy from ultrasonic irradiation of the specimen is absorbed in areas of the crystal lattice which bear the mechanism of plastic deformation, such as dislocations and grain boundaries and is almost unabsorbed in those areas free from defect zones in the crystal. This could explain the greater degree of recovery observed in the Al and Cu substrates when cold-worked. In cold-worked metals it would be easier to activate existing dislocations rather than to nucleate new dislocations, while in annealed metals dislocations are generated from grain boundaries. Activation of existing dislocations in the former

would give ample opportunity for dislocation interaction resulting in dislocation annihilation and other similar effects, possibly diffusion climb.

When the wire, substrate and tool make contact in the UWB process, intense dislocation movement occurs in the wire. This is evident in Fig. 59 where the bonding time is lowered to 20 msec. The wire begins to soften upon ultrasonic irradiation due largely to the numerous point defects generated. Dislocation movement originating at the top of the wire at the tool-wire interface moves away to the wire-substrate interface. More defects are generated here as the ultrasonically softened wire follows the contours of the substrate. The constraining effect of the wire-substrate interface beyond which dislocations cannot travel, causes them to lock firmly against the microscopic grooves in the substrate leading to adhesion. Due to intense dislocation activity in this region, recovered grains form. (as in Al) with the wire-substrate region being akin to a grain boundary interface in polycrystalline metals. Using this hypothesis the high strengths of wire bonds could be explained based on the fact that metal grain boundaries have higher strengths than the grains themselves.

As already stated while developing the model in Section 5.3, the substrate experiences simultaneous ultrasonic irradiation with the extent of damage depending upon the substrate material used. If the material encourages

dislocation movement, such as Al with a low σ_{ys} , then maximum microstructural transformation is observed. In the case of a high σ_{ys} material, such as stainless steel, minimum microstructural transformation is observed. The extent of ultrasonic damage observed in the substrate is a combination of a conducive to cross slip, namely SFE and the diffusion properties of the material. It is possible that in the case of a hard substrate, ultrasound may not be able to penetrate the substrate enough and sonic reflection could occur leading to undesirable excess softening of the wire. In some instances during bonding when this is, it can be overcome by decreasing the bonding parameters.

The analogy of ultrasonically transformed microstructures to non-ultrasonic cycling microstructures in Chapter IV is interesting. This can be put in the proper perspective by looking at the overall picture and singling out substrate properties conducive to atom movement resulting in a transformation.

The intense deformation observed in the PZ in Section 4.2 is a result of oxides from the wire or the contaminants from the substrate breaking up and being dispersed to the outside of the bond. Thus allowing for the necessary metal to metal contact.

8.2 Thermal Transformations and Reliability - The results of the experiments on thermally induced bond transformations

after bonding show that Al-Au intermetallic compounds readily form during aging or thermal cycling of Al wire/Au-plated substrate specimens. As described in section 2.3, intermetallic formation in the Al-Au system has been widely studied due to a commonly observed problem known as "purple-plague".

In experiments conducted in this research, bonds were aged at 125°C and thermally cycled to peak temperatures of 125°C. In addition, specimens not aged or thermally cycled were still exposed to a temperature of 90°C for 1 1/2 hours during sample preparation. In previous work (Okuni, Koizumi, Araki, 1987) on Au/Al intermetallic formation, it was shown that at low temperatures the Au_3Al_2 and Au_2Al form most readily, with $AuAl$ and $AuAl_2$ also observed. In this research, in thin-Au specimens, Au_3Al_2 was observed in specimens heated to 90°C. The $AuAl$ phase layer next to the Al wire transforms to $AuAl$ while the layer adjacent to the Ni forms a ternary compound with a composition close to $(Au,Ni)_2Al$ after aging at 125°C for 48 hours. Since the amount of Au available for reaction with the Al is limited due to the thin Au plating and the amount of Al is essentially unlimited, the formation of the more Al-rich phases at longer and higher aging times is expected. The formation of Au_3Al_2 is consistent with previous studies conducted using low aging temperatures. The Au_2Al phase was also observed in previous studies, but not in this research. However, it is thought that this phase may have

formed at intermediate annealing temperatures and times. In the thin-Au specimens subjected to 1500 thermal cycling, composition of the intermetallic was close to $Au_3(Al,Ni)_2$ although the intermetallic next to the wire was Al rich while that next to the Au was Au rich with substantial Ni content. However, the composition measurement of this phase may have been affected by absorption or beam spreading.

The amount of Ni found in the intermetallics of the thin-Au specimens was low except in the 48 hour/125°C specimen which contained 29.60 wt.%. In the thick-Au specimens, the amount of Ni in the Au layer near the Au/Ni interface was much higher, up to 44 wt.% as observed at point 3 in Fig. 78 and summarized in Table 13. Some of the Ni may be due to beam spreading, but there does appear to be significant Ni diffusing into the Au, which complicates phase identification. In the specimen subjected to 1500 thermal cycles, the composition of the intermetallic was near $Au_3(Al,Ni)_2$. In the 3000 cycle specimen, a distinct layer of AuAl was found at the original Au/Al interface. Further towards the Au/Ni interface, a phase with composition is again closer to $Au_3(Al,Ni)_2$. Based on previously done studies, it is surprising that the Au_2Al phase was not observed. However, it is possible that the Ni content of the phase makes formation of Au_2Al thermodynamically or kinetically unfavorable.

It is interesting that in both the thin-Au and thick-Au thermally cycled specimens, ternary intermetallics formed with

compositions close to Au_3Al_2 , while for specimens aged at $125^\circ C$ in addition to a ternary intermetallic, AuAl intermetallics also form. Another interesting point to note is that the thin-Au plating layer only $0.1 \mu m$ thick remained intact during bonding. This suggests that UWB is not a result of a friction between the wire and substrate as is the case in friction welding.

The pull strength data for the Au-plated substrates did not show any significant reduction in bond strength with aging or thermal cycling. However, extensive void formation was not observed, so the bond strength observations are consistent with the results of Philofsky (1970). In the thick-Au specimens, a very high purity (100%) soft Au was used, and it is well known (Horsting, 1972) that impurities can have a detrimental effect on bond strength after aging. The use of high-purity soft Au in this research may therefore have prevented excessive voiding and bond strength degradation.

There were no observations of intermetallic phase formation in the Al wire/Ni-B substrate specimens. This is not surprising, since Colgan et al. (Colgan, Nastasi, Mayer, 1985) found that intermetallics in the Ni-Al system start to form at about $300^\circ C$. In this research, the interface appears chemically sharp with little diffusion between the Ni and Al, although an Al oxide layer was observed in one case. The presence of an Al oxide layer could be detrimental to bonding or bond strength, although pull test data show the bond

strength was satisfactory. However, if the Ni was more heavily oxidized the pull strength could be reduced or bonding could be more difficult. This situation could not occur with Au substrates since there are no Au oxides, so oxides present at the interface are those due to the Al alone which appear tolerable. These oxides are most likely present after bonding to the Au substrates, but were not observed here because of the diffusion reactions which occurred. Nonetheless, with the use of Ni substrates, the formation of Ni oxides and their effects on bonding and bond strength are a concern. Substrate cleaning methods which remove any excessive amounts of Ni oxides would result in high bond reliability.

CHAPTER IX

CONCLUSIONS

Bond formation in the UWB process is a solid state process, with no melting at the interface. Microstructural examination of the Al wire showed dynamic annealing with dislocation loops, low angle grain boundaries and the absence of a cold worked structure. The average bonding temperature was estimated to be 250°C using a kinetic analysis. It is expected that this temperature distribution is nonuniform with regard to position and time, and higher temperatures could be achieved in high defect density regions.

Microstructural examination of the bonding substrates showed transformations to different extents. While the Al substrate showed maximum transformation, with features similar to that of the wire, the Cu substrates showed a lesser extent of dynamic recovery. Ni substrates showed a dislocation vein structure while the stainless steel substrates transformed the least with planar dislocation arrangements characterizing the microstructure. Increasing the bonding time resulted in further transformation.

Similar features in microstructures of transformations

observed in bonding substrates with those reported in non-ultrasonic fatigue cycling studies was noted. The transformed microstructure of different metal substrates was found to be analogous to reported substructures that developed in a metal along the CSS curve during non-ultrasonic fatigue cycling. Stainless steel showed region I features, Ni showed region II features, Cu shows a transition from region II to region III, while Al shows region III features.

A simple model was developed to estimate the extent of the microstructural transformations in the bonding substrates during UWB. In addition to demonstrating its effectiveness when applied to different metal substrates, the model also showed good agreement with experimental observations related to substrate grain size and ambient temperatures variations. However, the model was somewhat less effective in estimating the extent of the microstructural transformations in Cu alloys.

Intermetallics formed at the wire-bond interface for bulk Ni substrates and obeyed the parabolic growth law. Bonding of the Al wire to Ni-B plated substrates did not result in any intermetallic formation in either the aged or the thermally cycled conditions. However, Al_2O_3 was found to be present at the bond interface. Bonding of the Al wire to thin-Au plating did not cause removal of the Au plating during bonding. After 90 minutes at $90^\circ C$, the Au layer entirely transforms to Au_3Al_2 . After 48 hours at $125^\circ C$ the AuAl intermetallic phase and a

ternary phase with composition close to $(\text{Au,Ni})_2\text{Al}$ was detected as Ni diffuses into the Au layer. Thermal cycling resulted in extensive intermetallic formation with no AuAl formed but an intermetallic phase of Au_3Al_2 with Ni was detected. Wire bonding to the thick-Au plating revealed extensive reaction between the Al and the Au, and also diffusion of Ni into the Au layer. In addition to the AuAl intermetallic, a ternary phase of composition close to $\text{Au}_3(\text{Al,Ni})_2$ was detected in the specimens subjected to 1500 and 3000 thermal cycles. Bond pull strength measurements in the as-received specimens and those subjected to thermal cycling showed no consistent degradation of bond strengths. In all cases the bond strength was maintained at an acceptable level. Consistent with these results, no extensive voiding at the bond interfaces was observed.

Substrate topography, hardness and contamination studies showed that bond adhesion is achieved by the removal of oxides and contaminants from the metals being joined creating contact of bare metal surfaces. Contamination can be present within the bond interface at low-lying asperity regions. The presence of contamination along the interface causes dislocation generation at the interfaces. Bond strength studies on Al substrates were independent of substrate topography and contamination. Bond strength studies on stainless steel substrates indicated the need for optimum surface roughness and contamination played a larger role in smooth specimens.

CHAPTER X

SUGGESTIONS FOR FUTURE WORK

As is associated with any research investigation, there is always scope for future work. This need especially applies in an area such as UWB, rapidly taking on more significance with the miniaturization of electronic circuitry. The failure of even a single bond in the circuit interconnections could lead to the failure of the entire component.

Important areas warranting further investigating would be the microstructural development of a particular metal substrate using small variations in bonding parameters. This would enable researchers to relate the type of microstructures that could be expected of substrates for good or bad bonding.

Microstructural work characterizing the developed dislocation substructures in terms of the Burger vectors and thus better understanding of dislocation movements during UWB related to slip planes and dislocation directions could be done. This could be based on the results of the present investigation with much of the work being done on single crystal microstructural transformations. Results obtained from these microstructure characterization studies would then enable researchers to add appropriate constants and material

properties in the model developed in this study to estimate the extent of the microstructural transformation. The present model is simplistic in its approach and would need to be changed with new breakthroughs in UWB research.

In the area of intermetallic formation, it is known that Au and Al could form intermetallics at room temperatures. Therefore the as-bonded specimens in Chapter VI could be prepared by another method such as ultramicrotomy. In this method specimens could be mounted in a room temperature curing epoxy, thus eliminating any exposure of heat during sample preparation.

As research tool technology and techniques keeps pace with the demand for results and answers to new questions, perhaps an insitu investigation of the UWB process itself may one day be a possibility!!

REFERENCES

Abdel-Raouf, H., Plumtree, A., and Topper, T.H., "Temperature and Strain Rate Dependence of Cyclic Deformation Response and Damage Accumulation in OFHC Copper and 304 Stainless Steel", Met. Trans., Vol.5, January 1974, pp.267-277.

Blaha, F. and Langenecker, B., "Dehnung von Zink - Einkristallen unter Ultraschalleinwirkung", Naturwissenschaften 20, 1955, 556.

Boyer, H.E., Gall, T.L., ASM Metals Hand Book, 1985.

Brandes, E.A., Smithells Metals Reference Book, Sixth Edition, 1983, Pub. Butterworths, Boston.

Campisano, S.U., Foti, G., Rimini, E., Lau, S.S., and Mayer, J.W., "Kinetics of phase Formation in Gold-Aluminum Thin Films", Phil. Mag., Vol.31, 1975, pp.903-917.

Castleman, L.S., and Seigle, L.L., "Layer Growth During Interdiffusion in the Aluminum-Nickel Alloy System", Trans AIME, Vol.212, 1958, pp.589-596.

Chernenko, I.V., and Cherkashin, V.S., "The Use of Ultrasonics in Research on Materials", Vol.12, MOPI, Moscow 1960, as referenced in Severdenko, V.P., Klubovich, V.V., Stepanenko, A.V., 1972. Consultants Bureau, NY-London, 1972, pp.43-50.

Cliff, G., Lorimer, G.W., J. Microscopy, 103, 1975, p.203.

Colgan, E.G., Nastasi, M., and Mayer, J.W., "Initial Phase Formation and Dissociation in the Thin-Film Nickel-Aluminum System", J. Appl. Phy., Vol.58, 1985, pp.4125-4129.

Devine, J., "Joining Metals with Ultrasonic Welding", Machine Design, Sep. 1984.

Devine, J., "Joining Electric Contacts? Ultrasonic Works Fast", Welding Design & Fab., March 1980, pp.112-115.

Doong, S., Socie, D.F., and Robertson, I.M., "Dislocation Substructures and Non-Proportional Hardening", Trans. ASME, Vol.112, October 1990, pp.456-464.

Easterling, K.E., and Tholen, A.R., "Surface Energy and Adhesion at Metal Contacts", Acta Met., Vol.20, August 1972, pp.1001-1008

Fairbanks, H.V., "Some Solid State Microstructural Changes Produced in Metals by the Introduction of Macrosonics", Proc. of 1st Intl. Symp. on High-Power Ultrasonics, IPC Science and Technology Press, Surrey, U.K, September 1970, pp.116-119.

Feltner, C.E., and Laird, C., "Cyclic Stress-Strain Response of F.C.C. Metals and Alloys - I Phenomenological Experiments", Acta Met., Vol.15, 1967, pp.1621-1632.

Feltner, C.E., and Laird, C., "Cyclic Stress-Strain Response of F.C.C. Metals and Alloys - II Dislocation Structures and Mechanisms", Acta Met., Vol.15, 1967, pp.1633-1653.

Figueroa, J.C., Bhat, S.P., De La Veaux, R., Murzenski, S., and Laird, C., "The Cyclic Stress-Strain Response of Copper at Low Strains - I. Constant Amplitude Testing", Acta Met., Vol.29, 1981, pp.1667-1678.

Figueroa, J.C., and Laird, C., "The Cyclic Stress-Strain Response of Copper at Low Strains - II. Variable Amplitude Testing", Acta Met., Vol.29, 1981, pp.1679-1684.

Harman, G.G., and Albers, J., "The Ultrasonic Welding Mechanism as Applied to Al- and Au- Wire Bonding in Microelectronics", IEEE Trans. on Parts, Hybrids and Pkg., PHP-13, 1977, 406.

Harman, G.G., and Leedy, K.O., "An Experimental Model of the Microelectronic Ultrasonic Wire Bonding Mechanism", 10th Ann. Proc. of Reliability Phy. Symp., 1972, pp.49-56.

Hertzberg, R.W., "Deformation and Fracture Mechanics of Engineering Materials", Third Edition 1989, Pub. John Willey and Sons, NY.

Hockenhull, B.S., and Hacking, R.G., "Metal Fatigue at 20kHz", Proc. of 1st Intl. Symp. on High-Power Ultrasonics, IPC

Science and Technology Press, Surrey, U.K, September 1970, pp.44-49.

Hornbogen, E., Trans. ASM, Vol.56, 1963, p.16.

Horsting, C.W., "Purple Plague and Gold Purity", 10th Ann. Proceed., Reliability Phys., 1972, pp.155-158.

Hulst, A.P., and Lasance, C., "Ultrasonic Bonding of Insulated Wire", Welding Jour., February 1978, pp.19-25.

Jin, N.Y., Zhong, C., and Chen, X., "Cyclic Deformation of AISI-310 Stainless Steel - II. Saturation Dislocation Structures", Acta Met., Vol.38, No.11, 1990, pp.2135-2140.

Jin, N.Y., "Formation of Dislocation Structures during Cyclic Deformation of F.C.C. Crystals Oriented for Single-Slip", Acta Met., Vol.37, No.7, 1989, pp.2055-2066.

Jin, N.Y., and Winter, A.T., "Cyclic Deformation of Copper Single Crystals Oriented for Double Slip", Acta Met., Vol.32, No.7, 1984, pp.989-995.

Joshi, K.C., "The Formation of Ultrasonic Bonds between Metals", Welding Jour., 50, December 1971, p.840.

Kidson, G.V., J. Nucl. Mat., Vol.3, 1961, pp.21.

Konig, G., and Blum, W., "Comparison between the Cell Structures Produced in Aluminum by Cycling and by Monotonic Creep", Acta Met., Vol.28, 1980, pp.519-537.

Kralik, G., and Weiss, B., "Uber die Ultraschallverfestigung von kubisch flachenzentrierten Metallen und Legierungen", Zeitschr. Metallk., Vol.58, 1967, pp.471-475.

Kreye, H., "Melting Phenomenon in Solid State Welding Processes", Welding Rsch. Supp., May 1977, pp.154-158.

Krzanowski, J.E., "A Transmission Electron Microscopy Study of Ultrasonic Wire Bonding", Proc. 39th Elect. Comp. Conf.,

Houston, TX, 1989, pp.451-456.

Krzanowski, J.E., and Murdeshwar, N.M., "Deformation and Bonding Processes in Aluminum Ultrasonic Wire Wedge Bonding", Jour. of Electr. Mat., Vol.19, No.9, 1990, pp.919-928.

Langenecker, B., "The Effect of Sonic and Ultrasonic Radiation on the Safety Factors of Rockets and Missiles", AIAA, Vol.1, Jan.1963, pp.80-83.

Langenecker, B., "Effects of Ultrasound on Deformation Characteristics on Metals", IEEE Trans. on Sonics and Ultrasonics, Vol. SU-13, No.1, Mar.1966, pp.1-8.

Langenecker, B., Proc. ASTM, 62, 1962, pp.102-609.

Li, J.C.M., Trans. TMS-AIME, Vol.227, 1963, p.239.

Lustman, B., and Mehl, R.F., "Rate of Growth of Intermetallic Alloy layers in Structurally Analogous Systems", AIME Trans., Vol.147, 1942, pp.365-395.

Manji, G., Nobili, C., Ottaviani, G., Costato, M., and Gali, E., "Gold-Aluminum Thin Film Interaction and Compound Formation", J. Appl. Phys., Vol.52, 1981, pp.4047-4054.

Martin, B.D., Wilson, A.D., "An In-line Laser Interferometer Applied to Ultrasonic Bonder Characterization", IEEE Ultrasonics Symposium, San Francisco, California, Oct. 1970.

Mason, W.P., "Low and High Amplitude Internal Friction in Solids due to Dislocation Motions", Proc. of 1st Intl. Symp. on High-Power Ultrasonics, IPC Science and Technology Press, Surrey, U.K, September 1970, pp.15-22.

Maurer, K.L., "Electron Microscope Observation on Fatigue and Ultrasonic Fatigue in Metallic Materials", Proc. of 1st Intl. Symp. on High-Power Ultrasonics, IPC Science and Technology Press, Surrey, U.K, September 1970, pp.53-58.

Mehl, R.F., "Diffusion in Solid Metals", AIME Trans., Vol.122,

1936, pp.11-56.

Meyers, M.A., Chawla, K.K., "Mechanical Metallurgy Principles and their Applications", 1984, Pub. Prentice-Hall, Inc. NJ.

Mughrabi, H., Herz, K., and Stark, X., "Cyclic Deformation and Fatigue Behavior of α -Iron Mono- and Polycrystals", Intl. Jour. Fract., Vol.17, No.2, April 1981, pp.193-220.

Nevill, G.E., and Brotzen, F., "The Effects of Vibration on the Static Yield Strength of a Low-C Steel", Proc.Am.Soc. Testing Materials, 57, 1957, 751.

Philofsky, E., "Intermetallic Formation in Gold-Aluminum Systems", Solid-State Elect., Vol.13, 1970, pp.1391-1399.

Philofsky, E., 9th Ann. Proceed., Reliability Phys., 1971, pp.114-119.

Philofsky, E., 8th Ann. Proceed., Reliability Phys., 1970, pp.177-185.

Plough, C., Davis, D., and Lawler, H., "High Reliability Al Wire Bonding", Proc. Electr. Comp. Conf., Wash.D.C., April 1969, pp.157-165.

Puskar, A., J.Iron and Steel Inst., Vol.210, 1972, p.515.

Roderick, R.L. and Truell, R., "The Measurement of Ultrasonic Attenuation in Solids by the Pulse Technique and some Results in Steel", J.Appl.Phys., 23, 1952, 267.

Rosenberg, L.D., Physical Principles of Ultrasonic Technology, Vol.1, 1973, p.101.

Roth, L.D., Willertz, L.E., and Leax, T.R., "On the Fatigue of Copper up to Ultrasonic Frequencies",

Roven, H.J., and Nes, E., "Cyclic Deformation of Ferritic Steel - I. Stress-Strain Response and Structure Evolution", Acta Met., Vol.39, No.8, 1991, pp.1719-1733.

Saxena, A., and Antolovich, S.D., "Low Cycle Fatigue, Fatigue Crack Propagation and Substructures in a Series of Polycrystalline Cu-Al Alloys", Met. Trans., Vol.6A, September 1975, pp.1809-1828.

Schoeck, G., Phy.Status Solidi, Vol.32, 1969, p.651.

Severdenko, V.P., Klubovich, V.V., Stepanenko, A.V., "Ultrasonics Rolling and Wire Drawing of Metals", Consultants Bureau, NY-London, 1972, pp.43-50.

Shea, M.M., and Rao, B.V.N., "Surface Hardening and Microstructural changes in 304 Stainless Steel Resulting from Elevated Temperature Ultrasonic Vibration", Met. Trans., Vol.13A, July 1982, pp.1167-1176.

Smallman, R.E., "Modern Physical Metallurgy", Fourth Edition, 1985, Pub. Butterworths, Boston.

Uthe, P.M., "Variables Affecting Weld Quality in Ultrasonic Al Wire Bonding", Solid State Tech., Aug. 1969, pp.72-77.

Weiss, B., "The Defect Structure of Ultrasonically Fatigued Face Centered Cubic Metals", Proc. of 1st Intl. Symp. on High-Power Ultrasonics, IPC Science and Technology Press, Surrey, U.K, September 1970, pp.36-43.

Westmacott, K.H., and Langenecker, B., "Dislocation Structure in Ultrasonically Irradiated Aluminum", Phy.Rev.Lett., Vol.14, No.7, February 1965, pp.221-222.

Winchell II, V.H., and Berg, H.M., "Enhancing Ultrasonic Bond Development", IEEE Trans. on Comp., Hybrids, and Manuf. Tech. CHMT-1, 1978, pp.211-219.

Wood, W.A., and MacDonald, D.E., "Metal Fatigue at Ultrasonic Frequency", Proc. of 1st Intl. Symp. on High-Power Ultrasonics, IPC Science and Technology Press, Surrey, U.K, September 1970, pp.50-52.

Zener, C., "Elasticity and Anelasticity of Metals", Univ. of Chicago Press, Chicago, IL, 1948, p.154.

Zener, C., Phys. Rev., Vol.53, 1938, p.90.

Zhong, C., Jin, N.Y., Zhon, X., Meng, E., and Chen, X., "Cyclic Deformation of AISI-310 Stainless Steel - I. Cyclic Stress-Strain Responses", Acta Met., Vol.38, No.11, 1990, pp.2135-2140.